SERI/STR--211-3583

DE89 009496

Research on High-Efficiency, Single-Junction, Monolithic, Thin-Film Amorphous Silicon Solar Cells

Phase II Semiannual Report
1 February 1988 - 31 July 1988

**R. R. Ayra, M. S. Bennett, C. R. Dickson,
B. Fieselmann, C. Fortmann, B. Goldstein,
J. Morris, J. G. O'Dowd, R. S. Oswald,
S. Wiedeman, L. Yang**
Solarex Thin Film Division
Newtown, Pennsylvania

October 1989

SERI Technical Monitor: B. Stafford

Prepared under Subcontract No. ZB-7-06003-2

Solar Energy Research Institute
A Division of Midwest Research Institute

1617 Cole Boulevard
Golden, Colorado 80401-3393

Prepared for the
U.S. Department of Energy
Contract No. DE-AC02-83CH10093

DISCLAIMER

This report was prepared as an account of work sponsored by an agency of the United States Government. Neither the United States Government nor any agency thereof, nor any of their employees, makes any warranty, express or implied, or assumes any legal liability or responsibility for the accuracy, completeness, or usefulness of any information, apparatus, product, or process disclosed, or represents that its use would not infringe privately owned rights. Reference herein to any specific commercial product, process, or service by trade name, trademark, manufacturer, or otherwise does not necessarily constitute or imply its endorsement, recommendation, or favoring by the United States Government or any agency thereof. The views and opinions of authors expressed herein do not necessarily state or reflect those of the United States Government or any agency thereof.

DISTRIBUTION OF THIS DOCUMENT IS UNLIMITED

MASTER

DISCLAIMER

This report was prepared as an account of work sponsored by an agency of the United States Government. Neither the United States Government nor any agency thereof, nor any of their employees, makes any warranty, express or implied, or assumes any legal liability or responsibility for the accuracy, completeness, or usefulness of any information, apparatus, product, or process disclosed, or represents that its use would not infringe privately owned rights. Reference herein to any specific commercial product, process, or service by trade name, trademark, manufacturer, or otherwise does not necessarily constitute or imply its endorsement, recommendation, or favoring by the United States Government or any agency thereof. The views and opinions of authors expressed herein do not necessarily state or reflect those of the United States Government or any agency thereof.

DISCLAIMER

Portions of this document may be illegible in electronic image products. Images are produced from the best available original document.

NOTICE

This report was prepared as an account of work sponsored by an agency of the United States government. Neither the United States government nor any agency thereof, nor any of their employees, makes any warranty, express or implied, or assumes any legal liability or responsibility for the accuracy, completeness, or usefulness of any information, apparatus, product, or process disclosed, or represents that its use would not infringe privately owned rights. Reference herein to any specific commercial product, process, or service by trade name, trademark, manufacturer, or otherwise does not necessarily constitute or imply its endorsement, recommendation, or favoring by the United States government or any agency thereof. The views and opinions of authors expressed herein do not necessarily state or reflect those of the United States government or any agency thereof.

Printed in the United States of America
Available from:
National Technical Information Service
U.S. Department of Commerce
5285 Port Royal Road
Springfield, VA 22161

Price: Microfiche A01
Printed Copy A06

Codes are used for pricing all publications. The code is determined by the number of pages in the publication. Information pertaining to the pricing codes can be found in the current issue of the following publications which are generally available in most libraries: *Energy Research Abstracts (ERA)*; *Government Reports Announcements* and Index (*GRA* and I); *Scientific and Technical Abstract Reports (STAR)*; and publication NTIS-PR-360 available from NTIS at the above address.

SUMMARY

Subtask B1: The major focus of this subtask has been on improving the quality of the amorphous wide and narrow bandgap candidate materials, namely a-$Si_{1-x}C_x$ and a-$Si_{1-x}Ge_x$. The transport and optical properties of the undoped films were characterized by Photothermal Deflection Spectroscopy, Raman Spectroscopy, dark and photo-conductivity, and visible and near infrared spectroscopy. Films were prepared from a wide range of feedstocks. Although both germanium and carbon containing alloys show a decrease in mobility-lifetime product as the fraction of silicon decreases, there are marked differences in the optical properties of the alloys. The carbon containing alloys exhibit an increase in the Urbach energy as carbon is added, indicating an increase in the tail density of states distribution. In contrast, no such increase in the either the tail or midgap density of states is evident in the silicon germanium alloy. Raman spectroscopy indicates that the silicon germanium alloys are inhomogeneous, showing a higher concentration of germanium-germanium bonds than expected from a random mixing model.

Microcrystalline p-layer films containing carbon have been prepared to evaluate their importance for achieving high open circuit voltage. It has been possible to prepare microcrystalline p-layers containing carbon using disilylmethane instead of methane. Although excellent conductivity for these films has been obtained, no evidence of a crystalline SiC phase is seen in the Raman spectra. Although open circuit voltages as high as 0.88 volts have been achieved with these films, similar results have been obtained using amorphous p-type alloy films.

Silicon-germanium devices have been studied to optimize their performance in multijunction stacked cell structures. Far better performance for the alloy devices is obtained using an amorphous n-layer despite the concern of a barrier to electron flow that might be expected to arise from such a heterojunction. Conductivity measurements indicate and devices confirm that the higher resistivity obtained from the alloy has a detrimental effect on device performance. In addition grading the p/i interface also markedly improves device performance as we have previously shown for a-Si heterojunctions. Initial results indicate that the transport properties of the alloy can be improved by trace level doping with boron.

The best devices fabricated from the silicon germanium alloys had a conversion efficiency of 10.1%. The bandgap of this alloy was 1.55eV. The device exhibited a current density of 20mA/cm^2. This measurement may be low because of the use of a Xenon simulator filtered for AM1.5 use; such simulators have relatively poor output at long wavelengths.

Conversion efficiencies over 10% have been obtained using several alloy based stacked cells. Four configurations have been used: an a-SiC top cell with either a-Si:H or a-SiGe:H bottom cells, as well as both an a-Si:H/a-SiGe:H and a-Si:H/a-Si:H tandem device. 10.5% has been obtained by coupling an a-SiC top cell with an a-SiGe bottom device while an a-SiC:H/a-Si:H structure has yielded 10.2%

Stacked junction devices have shown far less susceptibility to light-induced degradation. For example an a-Si:H/a-Si:H tandem with an initial performance of close to 9% lost less than 14% of its initial performance after 1150 hours of exposure. Analysis indicate that the rate of degradation of stacked junction devices is the mean of the rates of degradation of the individual devices.

TABLE OF CONTENTS

Section Page

FIGURE CAPTIONS

LIST OF TABLES

SECTION 1.0
INTRODUCTION

The principle objective of this three year research program is to develop multi-junction submodules of amorphous silicon based alloys having a conversion efficiency of at least 13% over an area greater than 900cm^2.

The research program consists of three subtasks. The purpose of Subtask B1: Semiconductor Materials Research is to prepare, characterize and optimize the chemical, structural, optical and electronic properties of the amorphous silicon (a-Si) based alloys that will be used in submodule research. Subtask B2: Non-Semiconductor Materials Research involves the production, characterization and optimization of non-semiconductor materials that are required to make high performance multi-junction submodules. In Subtask B3: Submodule Research, we will develop an a-Si based submodule with a 13% conversion efficiency over a total area of at least 900cm^2 in a multi-junction configuration.

SECTION 2.0
SUBTASK B1: MATERIALS RESEARCH

2.1 OPTICAL AND TRANSPORT PROPERTIES OF a-SiC AND a-SiGe ALLOYS

High efficiency multijunction amorphous silicon based devices require improvements in the transport properties of both the wide and narrow bandgap alloys. Given the constraint that one junction in the multijunction device must contain 1.7eV bandgap a-Si, the optimum performance is achieved with a rear junction i-layer bandgap of 1.1eV. Using the same constraint a triple junction stacked cell would require a 2.0eV top bandgap i-layer and a bottom cell bandgap of 1.45eV. Using a four terminal device (or six) relaxes the bandgap constraints and provides a much greater flexibility in the thickness of the junctions, since current matching is no longer required.

During the period of this report, we have concentrated on making and studying undoped films, routinely measuring dark and photoconductivity, IR absorption by means of FTIR spectroscopy and Raman spectroscopy, and determined the midgap densities of states, Urbach energy and optical bandgap using PDS (Photothermal Deflection Spectroscopy) and visible and near infrared absorption spectroscopy. On some samples elemental analysis was done by means of Rutherford backscattering spectroscopy (RBS) and Energy Dispersive X-Ray Analysis. We chose the mobility-lifetime product derived from photoconductivity data as a measure of film quality recognizing that this can be influenced by factors such as Fermi level position, which may not reflect the actual device performance. We have not yet made a complete set of solar cells using i-layers deposited using the same deposition conditions as were used for the films. Measurement of cell parameters will allow us to determine if the mobility-lifetime product, or any other measurement, is an appropriate figure of merit.

Both wide gap and narrow gap films were made, using a variety of feedstocks, diluents and deposition conditions. These are partially listed in Table 2.1-1.

Summaries of some of the results are shown in Figure 2.1-1 for mobility lifetime product and Figure 2.1-2 for Urbach edge. Several trends are readily apparent. The photoconductive properties of the alloys fall as the bandgap (estimated to be the energy at which the absorption coefficient equals $2x10^3cm^{-1}$ as measured by PDS) moves away in either direction from that of a-Si:H. Specifically, the log of the mobility-lifetime product falls linearly with bandgap more or less independently of

[redacted]

FIGURE 2.1-1. MOBILITY-LIFETIME PRODUCT PLOTTED VERSUS OPTICAL BANDGAP OF a-Si$_{1-x}$C$_x$:H and Si$_{1-x}$Ge$_x$:H FILMS

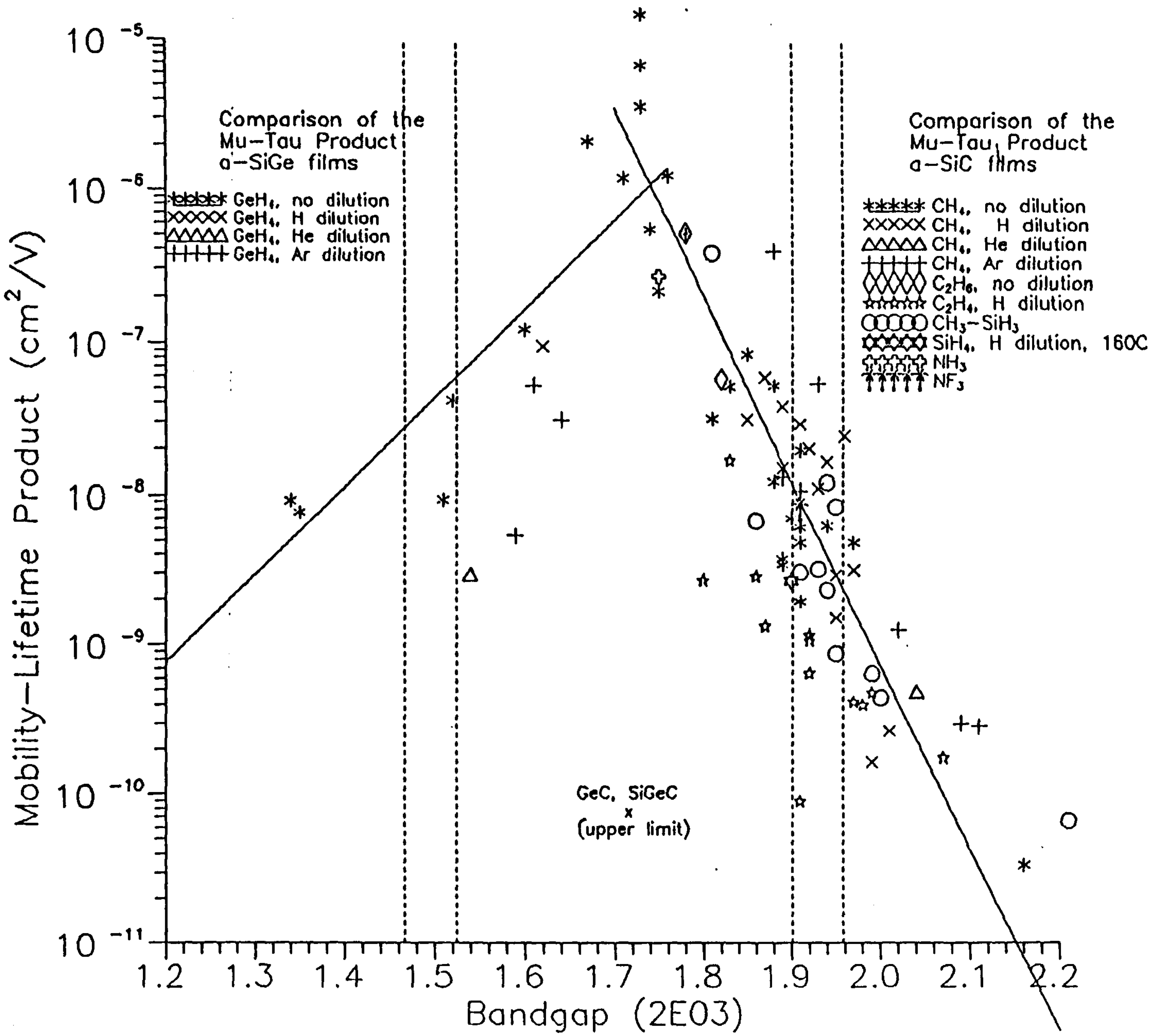

FIGURE 2.1-2. URBACH ENERGY AS A FUNCTION OF BANDGAP FOR a-$Si_{1-x}Ge_x$:H AND a-$Si_{1-x}C_x$:H.

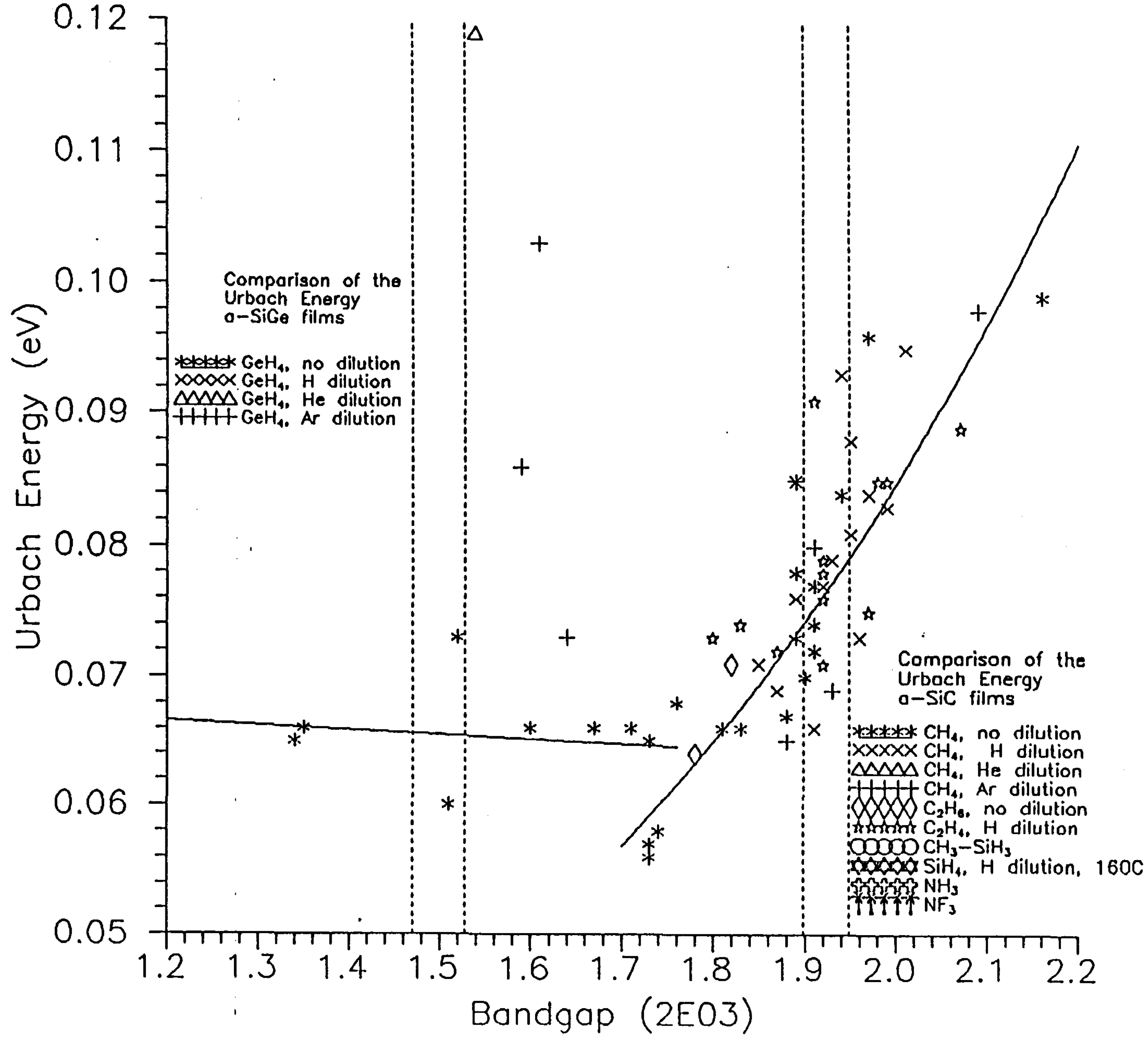

TABLE 2.1-1

Feedstocks used for the prpeparation of the a-$Si_{1-x}C_x$:H alloys

Feedstock	Diluent
CH_4	none
"	Ar
"	H_2
"	He
C_2H_6	none
C_2H_4	H_2
SiH_3-CH_3	none
"	Ar
"	H_2

the preparation method. The fall off in mobility-lifetime product is much more rapid for the silicon-carbon and silicon-nitrogen alloys than the silicon-germanium alloys. There is also a pronounced difference in the slope of the Urbach edge for the wide and narrow gap alloys as shown in Figure 2.1-2. The Urbach edge is independent of bandgap in the case of SiGe alloys, while a rapid increase in the Urbach energy is seen for the wide bandgap alloys. Therefore the mechanism for the decrease in the transport properties of the two classes of alloys appears to be quite different.

The lack of an increase in the midgap density of states for the silicon-germanium alloys, also associated with the light induced defect, suggests a mechanism other than the dangling bond defect limits transport properties. The problem may lie with preferred Ge-Ge bonding or clusters of Ge leading to large potential fluctuations in the material and recombination centers. Raman spectroscopy has been used to study inhomogeneities in the alloys and these results are discussed elsewhere in this report. In addition, the effect of local Ge-Ge bonding has been studied in devices, and these results are summarized in Appendix I.

We have investigated the effect of deposition pressure and temperature, flow rates, etc. for the feedstocks listed in Table 2.1-1. Although no scheme has been devised into which all results can be fit, some of our findings are summarized below.

1) A mixture of SiH_4 and CH_3-SiH_3 produced films which were, at a given bandgap, indistinguishable from films produced from CH_4 feedstock, using any of the measurements available to us. However carbon was incorporated into the film much more efficiently than from a silane-methane mixture.

2) Films made from ethylene (C_2H_4) were uniformly poor. We suspect that all feedstocks containing double and triple C bonds will have similar poor properties. It was necessary to dilute this feedstock in hydrogen to avoid graphitic deposits.

3) Films grown from methane highly diluted in argon have much greater carbon incorporation and in some cases improved photoconductive properties.

4) SiC films made from methane diluted in either H_2 or Ar were of higher quality than those made from methane with no dilution. This conclusion is based on the IR peaks around $2000cm^{-1}$ (indicative of mono- or di-hydride bonding in a dense network) and $2070cm^{-1}$ (indicative of similar bonding in an environment of larger microvoids).

5) Films made from methane with no H_2 dilution show fewer C-H_2, CH_3, Si-CH_3 bonds as the deposition power is increased. Similar films made with H_2 dilution show that the

2070cm^{-1} peak, the Si-CH$_3$ peak and the Si-H wag peak all broaden as the deposition power increases.
6) A few SiN films were grown with bandgaps in the 1.9eV range using NH$_3$ and NF$_3$ as feedstocks. These had very similar properties to SiC of the same bandgap.

7) Although work is continuing on the Si-Ge alloys, early attempts to use inert gas dilution have not been successful in making films with improved properties. Also films prepared from a mixture of disilane and silicon tetrafluoride and germane with or without dilution show improved mobility-lifetime product at a given bandgap than the corresponding alloy prepared from other feedstocks. However the activation energy of the dark conductivity is less than half the bandgap and devices prepared from these feedstocks show poor response.

2.2 RAMAN SPECTROSCOPY OF SiGe ALLOYS

Improving the quality of a-SiGe alloys is now one of the central elements in amorphous semiconductor photovoltaic research. So far the quality of the alloys has proven poorer than amorphous silicon, at least on a relative basis. A number of possible causes have been suggested to account for the observed poor opto-electronic properties of the alloys in terms of their bonding characteristics. For instance, Ge atoms were suspected to bond preferentially with each other forming clusters which act as effective carrier traps or recombination centers. However, there has been no direct evidence from structural analysis to prove this hypothesis which was based on primarily transport and TEM measurements

During this period, we have attempted to use Raman spectroscopy to search for direct evidence of structural inhomogeneities and establish a correlation between the microstructure of the alloy films to its transport properties. Raman spectroscopy is well known for its good sensitivity to the local bonding environment. In many cases, the intensity of the characteristic Raman peak can be used as a direct measure of the density of the particular type of bonds in the film. Therefore, by analyzing the relative peak intensities associated with Si-Si, Si-Ge and Ge-Ge bonding, one would be able to tell whether Ge-Ge bonding is more favored than Si-Ge bonding. Moreover, if preferential bonding does not exist, the degree of clustering can be modeled to give parameters such as the average size of clusters and the mean distance between nearest clusters. These parameters may then shed light on the observed opto-electronic properties of the alloy material.

Preliminary results of Raman measurements on a series of a-Si$_{1-x}$Ge$_x$:H alloy samples made by dc glow discharge of germane diluted in silane yield important evidence of

FIGURE 2.2-1. RAMAN SPECTRA OF a-$Si_{1-x}Ge_x$:H SAMPLES.

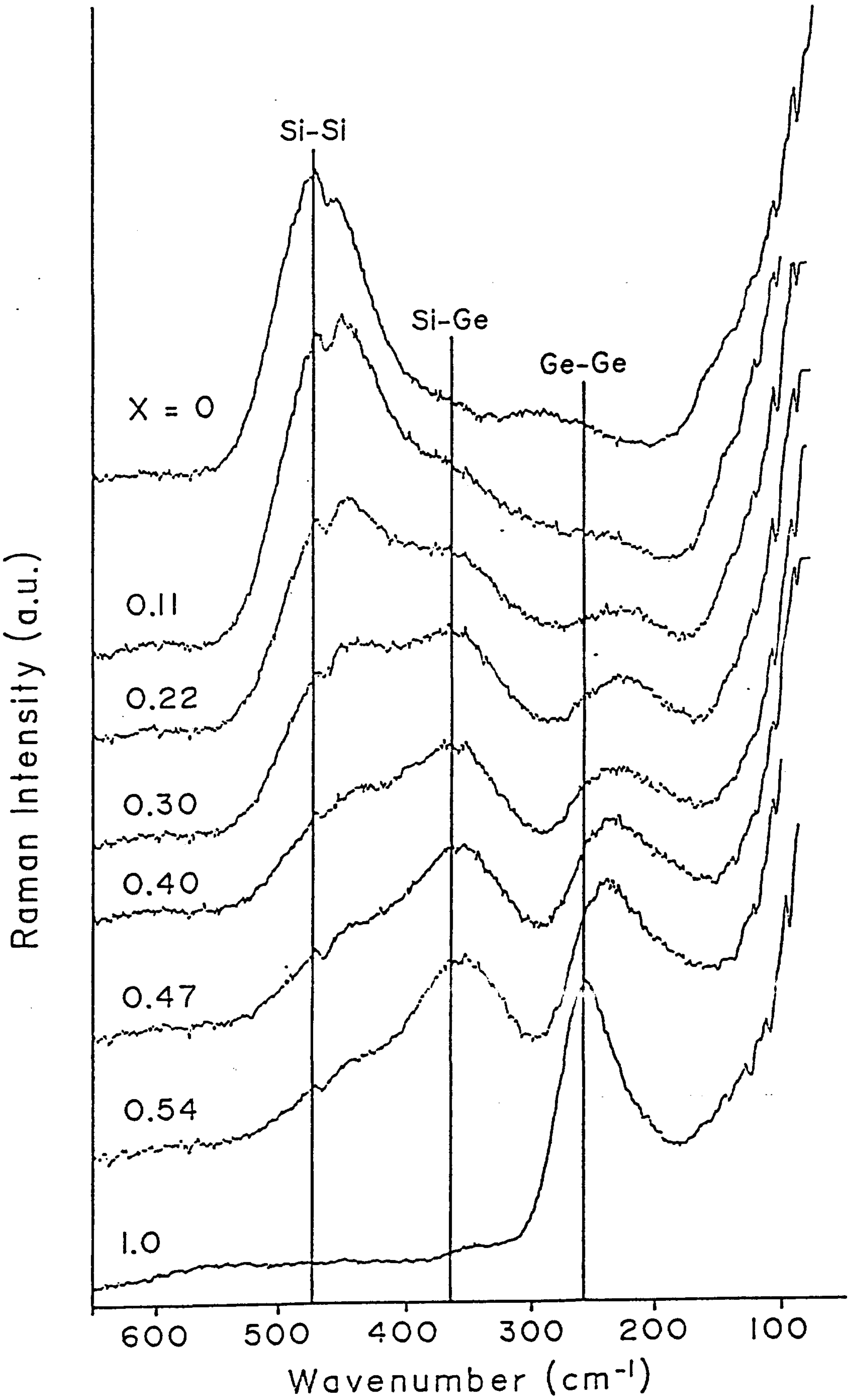

FIGURE 2.2-2. PLOT OF THE RATIO OF THE INTEGRATED INTENSITY FOR Ge-Ge BONDS (I_{Ge-Ge}) TO SiGe BONDS (I_{Si-Ge}).

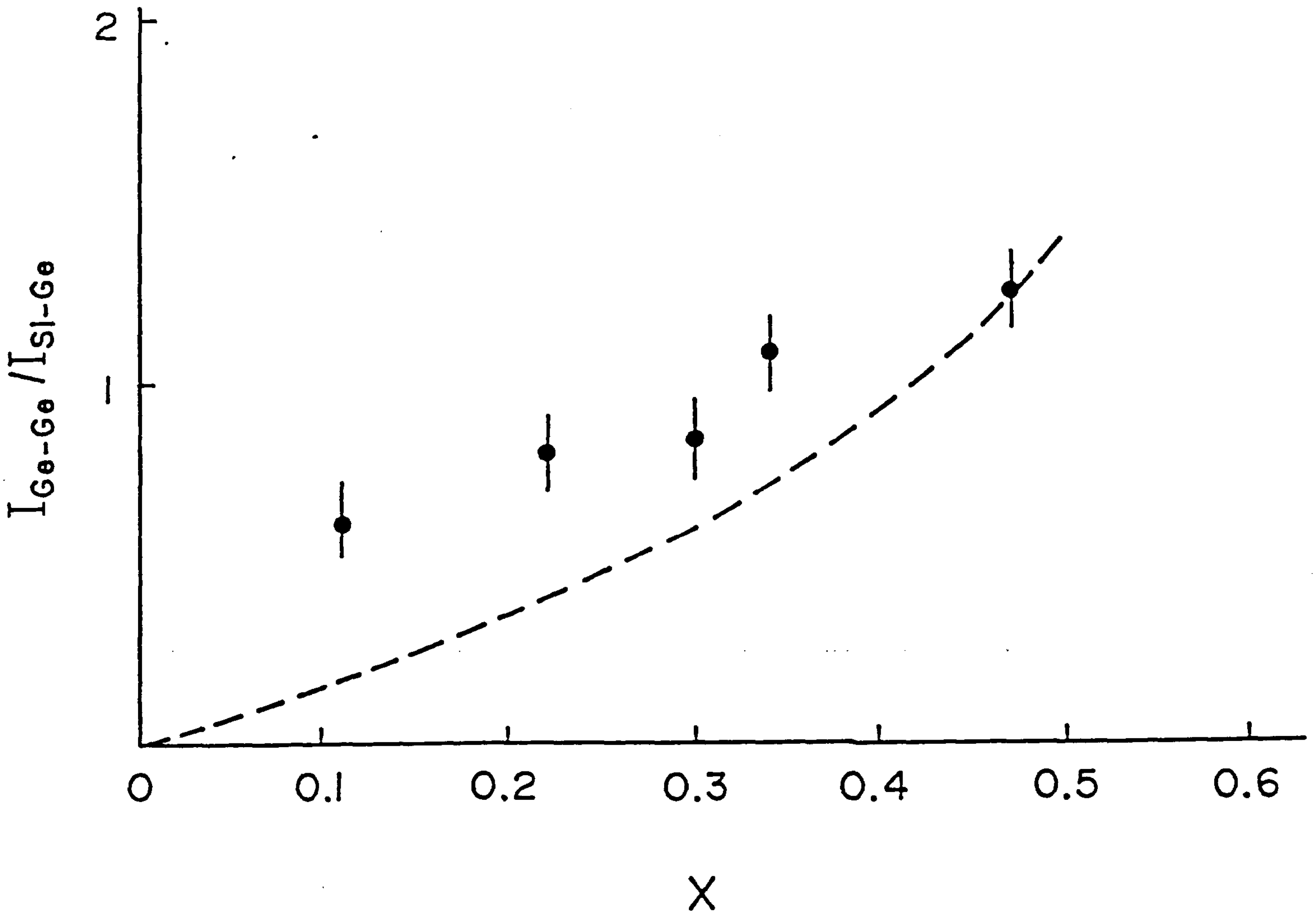

local inhomogeneities in the bonding environment. Figure 2.2-1 shows the Raman spectra of the alloy samples. The germanium concentration, x, measured by RBS is indicated for each spectrum in the figure. For pure a-Si:H (x=0), a strong Raman peak centered at a wavenumber of ~480cm^{-1} is observed which corresponds to the TO vibrational mode of Si-Si bonding. The sharp rise in intensity at wavenumbers below 140cm^{-1} is due to the tail of the excitation laser line at 514.5nm. Even at very low germanium concentrations, two additional Raman peaks at ~365cm^{-1} and ~265cm^{-1} clearly emerge which correspond to the vibration modes of Si-Ge and Ge-Ge. We decomposed each spectra into Si-Si, Si-Ge and Ge-Ge components and plotted the ratio of the integrated intensity, I_{Ge-Ge}/I_{Si-Ge}, as a function of germanium concentration in Figure 2.2-2. To this end, we want to compare this result to the case where bonds are randomly mixed with no preferential chemical ordering. Based on statistics, we know that for this ideal situation the bond densities of Si-Si, Si-Ge and Ge-Ge would be respectively proportional to $(1-x)^2$, $2(1-x)x$ and x^2, resulting in a ratio of I_{Ge-Ge}/I_{Si-Ge} to be proportional to $x/2(1-x)$. Although we lacked a calibration for the random mixing model, we forced the theoretical curve to go through the experimental point with the highest germanium concentration (x=0.47) as shown in Figure 2.2-2. For all the samples measured ($0.1<x<0.5$), the experimental values for the I_{Ge-Ge}/I_{Si-Ge} ratio were found to be inevitably higher than those predicted by the random mixing model.

Our preliminary result indicates that Ge atoms tend to form clusters in the alloys. Since this cluster formation appears to take place at a Ge concentration as low as only ~10%, we might further speculate that such a cluster formation is associated with the plasma decomposition process and clusters of a few Ge atoms may already form in the gas phase and then be incorporated into the film.

More detailed analysis of Raman measurements are now underway; this includes the calibration of the theoretical curve for the random mixing model by using an alloy sample with a minimal amount of Si dispersed in the Ge matrix. After all, we hope that Raman spectroscopy will eventually be able to provide a guideline in the search for better alloy materials using novel feedstocks and different deposition conditions.

2.3 FEEDSTOCK RESEARCH

2.3.1 Novel Dopants for p-layer Films

To improve the performance of the p-layer in p-i-n photovoltaic cells, novel sources of carbon and boron were investigated. Recent published efforts involve the synthesis and materials studies with trimethylboron ($B(CH_3)_3$). The compound $B(CH_3)_3$ is a monomeric boron compound which is expected to give an amorphous silicon film with few unfavorable boron-boron bonds than the more traditional dimeric boron source diborane (B_2H_6). Trimethylboron is also more chemically stable than diborane and thus is easier to handle during deposition studies.

An initial small scale preparation of $B(CH_3)_3$ was undertaken using the following synthetic route:

$$Al(CH_3)_3 + B(OCH_3)_3 \rightarrow B(CH_3)_3 + Al(OCH_3)_3$$

The synthesis and product purification were carried out on a standard vacuum line and gave about two grams of the desired compound in 60% yield. Gas chromatography/mass spectroscopy analyses indicated that the final purity was 99.6%. For depositions, the $B(CH_3)_3$ was diluted to 1% by volume with silane.

The analysis of the films prepared with $B(CH_3)_3$ is not complete, but a few points are clear. The methyl groups in $B(CH_3)_3$ are reactive in the deposition plasma and carbon is present in the films made with trimethyl boron. Thus it is not possible to compare directly films doped with diborane and trimethylboron without taking into consideration the carbon deposited by the later compound. To compare amorphous silicon films containing diborane with similar films containing trimethylboron films, it has proven necessary to add methane to diborane films to obtain comparable materials with similar bandgaps.

2.3.2 Stability of Diborane for p-layer Films

To improve the reliability of amorphous silicon device fabrication, an analytical program was undertaken to monitor the stability of the diborane concentration in the feed gas mixture, B_2H_6/SiH_4, as a function of time. The most unstable of the feed gases that are utilized in the preparation of amorphous silicon photovoltaic cells is the B_2H_6 mixture, which has often proved to be a source of difficulty in preparing high performance cells. The gas mixture is usually blended by a vendor to a concentration of several percent B_2H_6 in silane. The flow rate of this gas is adjusted to give optimum cell performance.

After attempting without success to use gas chromatography to quantitate diborane/silane mixtures, a wet chemical analytical method was developed that permitted quantifying of diborane at the 0.1-10% level in silane. The method relies on the fact that silane does not react with deoxygenated water while diborane decomposes to form boric acid and hydrogen. Using a standard analytical technique,

FIGURE 2.3.2-1. CONCENTRATION OF DIBORANE IN DIBORANE-SILANE MIXTURES AS A FUNCTION OF TIME.

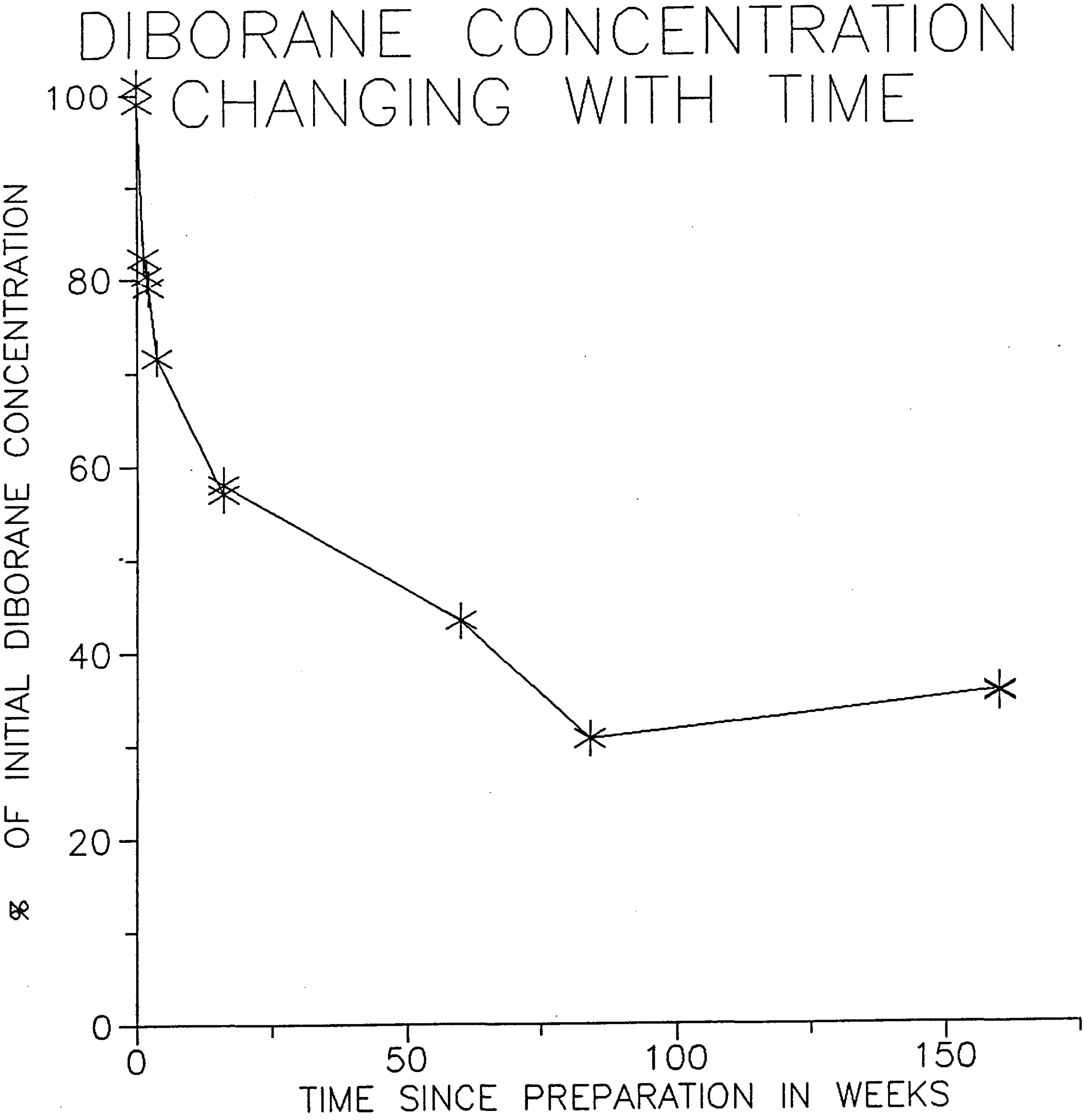

the boric acid is complexed with the sugar mannitol to form a strong acid which is titrated with sodium hydroxide. The entire analytical sequence is given below:

$B_2H_6 + SiH_4 + 6H_2O \text{ ----> } 2B(OH)_3 + 6H_2 + SiH_4$

$B(OH)_3 + \text{mannitol ----> } HOB(\text{mannitol}) + 2H_2O$

$NaOH + HOB(\text{mannitol}) \text{ ----> } NaOB(\text{mannitol}) + H_2O$

A decrease in diborane concentration with time was established by analyzing a single B_2H_6/SiH_4 gas cylinder every week throughout the first few months after blending. The long term stability was obtained by analyzing several selected B_2H_6/SiH_4 cylinders from a number of different vendors which initially had diborane concentrations of several percent and which had been in use for various periods of time.

The results to date are presented in Figure 2.3.2-1 and confirm that the actual diborane concentration is typically much less than the initial concentration. The data shows that there is a rapid decline in B_2H_6 concentration during the first four months after blending. The concentration of diborane continues to drop to about half of its initial level. Thereafter the tank continues to show a slower rate of diborane degradation until after a year and a half the B_2H_6 concentration stabilizes at 30-35% of its initial value. The results are particularly important when one is trying to reproduce previous work or when an old cylinder of B_2H_6/SiH_4 is being replaced by a newly prepared cylinder.

2.4 p+ MICROCRYSTALLINE SiC:H FILMS FOR HIGH VOLTAGE SOLAR CELLS

A series of experiments was performed to compare methane and disilylmethane in the preparation of microcrystalline p+ material. It was found that using the same hydrogen-diluted, rf, high power glow discharge microcrystalline p+ SiC can be made using methane except that more carbon can be incorporated into microcrystalline films using disilylmethane before the microcrystallinity is suppressed. Where relatively high-conductivity, partially microcrystalline films can be made with DSM containing up to 6% carbon, such films can be made with only 3-4%C when CH_4 is used as the feedstock. It is speculated that this may be due to the fact that the feedstock molecule already contains bonded C and Si for the case of DSM, and can thus be more effectively incorporated into the lattice with less bond-breaking. It should be noted that even in the microcrystalline films containing carbon, the evidence is that these films contain microcrystalline silicon in a matrix of carbon containing amorphous alloy; there is no evidence for a microcrystalline SiC phase. However since the cross section for absorption of the Si-C bond is low, Raman spectroscopy has relatively poor sensitivity to the crystalline SiC phase.

As reported earlier, the only substrate on which we have been able to grow microcrystalline p+SiC:H is amorphous Si:H. Measurements have indicated that 100-200Å of the latter is required. Accordingly, we are currently interposing an amorphous layer on SiC:H (10% C) ~100-150Å thick between CTO and the p+ microcrystalline layer in our test cells.

Transmission Electron Micrographs (TEM) of sectioned p+-i-n+ structure at a magnification of 600,000 have shown directly the presence of microcrystalline p+ and n+ layers (see Figure 2.4-1(a) and (b)). The size of grains are of the order of 50-100Å, in good agreement with inferences from the Raman data shown in earlier reports. The degree of microcrystallinity is considerably better for the n+ layer than for the p+ layer, - even though there was 100Å of α-Si:H as a substrate for the p+ layer to grow on. This is most likely due to the well-known crystallization-enhancing action of phosphorous. Accordingly, we have attempted to grow a better microcrystalline p+-layer in p-i-n cells that would produce significant and worthwhile improvements, e.g., a V_{OC} close to 1V. We have counter-doped the p+-layer with phosphorous (while, of course keeping it's level less than that of B). We have increased the doping levels of both P and B in the p+-layer to help initial nucleation. We have even interposed a 30-50Å thick (tunnelable) phosphorous-doped microcrystalline layer to act as a seed bed for the p+-microcrystalline layer. However we have still seen no effect of a microcrystalline p+-layer on cell properties. (We have sent two such cells to Amoco's corporate research facility in Naperville to see if we could detect any microcrystalline layers with a scanning TEM).

A model for the deposition of microcrystalline Si:H has been proposed by Veprek which involves, among other things, the beneficial presence of H atoms on the substrate and then subsequently on the grown layer, which aids and abets the nucleation of crystallites by bringing the growth of layers closer to chemical equilibrium with the depositing vapor. We suggest that this might explain why microcrystalline material deposits on α-Si:H, but not on CTO, e.g., see Fig. 2-40 of the 1987 Annual Report.

In addition to our attempts to incorporate μc-p+ layers into solar cells described above, basic cell structures were grown that included bandgap grading between the μc-p+ layer and the i-layer in order to minimize interfacial recombination from possibly limiting V_{OC}. In the graded case V_{OC} increased significantly over that of

FIGURE 2.4-1a,b. TEM PHOTOGRAPHS OF MICROCRYSTALLINE P+ AND N+ LAYERS, RESPECTIVELY. NOTE THE GRAIN SIZE OF THE N+ LAYER (TOP PHOTOGRAPH, A) COMPARED TO THE P+ LAYER (BOTTOM PHOTOGRAPH, B).

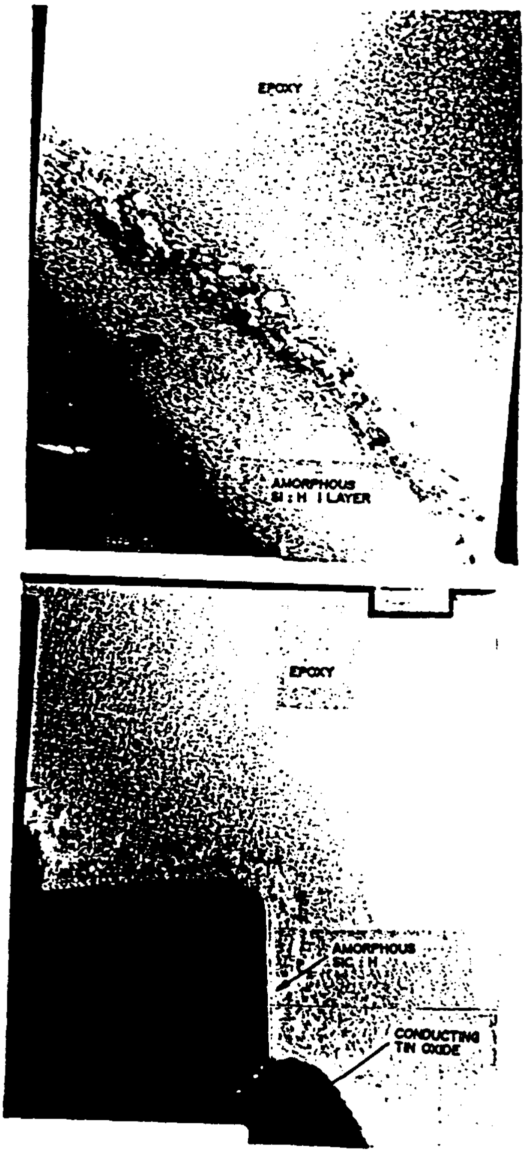

the ungraded reference; maximum values of 0.88V were reached, but such values are really no better than those achieved with grading using amorphous SiC layers. Furthermore, evidence is accumulating that the combination of necessary buffer layer and thicker-than-usual μc-p+ layer may, even with wide bandgaps, be significantly reducing J_{SC}.

To summarize briefly, after some considerable effort we have yet to observe any sign that we have successfully incorporated a well-formed microcrystalline p+ layer of SiC:H into a p-i-n solar cell. No cell property such as V_{OC} or fill factor has significantly improved. In contra-distinction, good microcrystalline n+ layers, as in Figure 2.4-1, have been directly observed as have increases in their electrical properties such as lateral conductivity. We have recently fabricated n-i-p/ITO solar cell structures on both stainless steel and glass/CTO which contain microcrystalline p+ layers of SiC:H; however the properties of such stainless steel and glass/CTO which contain microcrystalline p+ layers of SiC:H; however the properties of such structures have not yet been measured.

Future plans in this area include a broader investigation of the deposition parameter space, and novel methods of making microcrystalline layers such as by laser-solid interactions.

Progress was made in our understanding of the annealing effect reported earlier in which both the resistivity and Fermi-level of p+-layers deposited at low temperature decreased markedly upon annealing at 225°C. (1) It was determined that the deposition temperature has to be below 125°C for the effect to be observed and (2) the IR vibrational spectrum for these low temperature films contain no sign of the CH_3 radical, while after annealing both the rocking and bending modes of CH_3 attached to silicon are clearly seen, as shown in Figure 2.4-2. (Films deposited above 125°C show the modes associated with CH_3 without subsequent annealing.) Bearing in mind that the total hydrogen content actually increases as the deposition temperature decreases, we suggest that hydrogen appears to be the common factor between the formation of the $Si-CH_3$ complex and, through its interaction with dangling bond states and boron, the observed increases in B doping efficiency. We suggest that at low temperature the hydrogen has not yet either complexed with carbon or interacted with dangling bond states due to some barrier, and that some thermal energy is required to overcome this barrier - somewhat akin to be the heat treatment required to "activate" ion-implanted dopant atoms in single crystal silicon. Even if the hydrogen needs to move one or two atom distances for proper orientation for complexing, such thermally induced motion at ~200°C is quite reasonable and plausible considering its mobility at these temperatures.

FIGURE 2.4-2. FTIR SPECTRA OF μc-p+ FILM DEPOSITED AT 110°C (A) UNANNEALED; (B) ANNEALED AT 225°C. NOTE APPEARANCE OF CH_3 LINES AT 780cm^{-1} AND 1200-1400cm^{-1} AFTER ANNEALING.

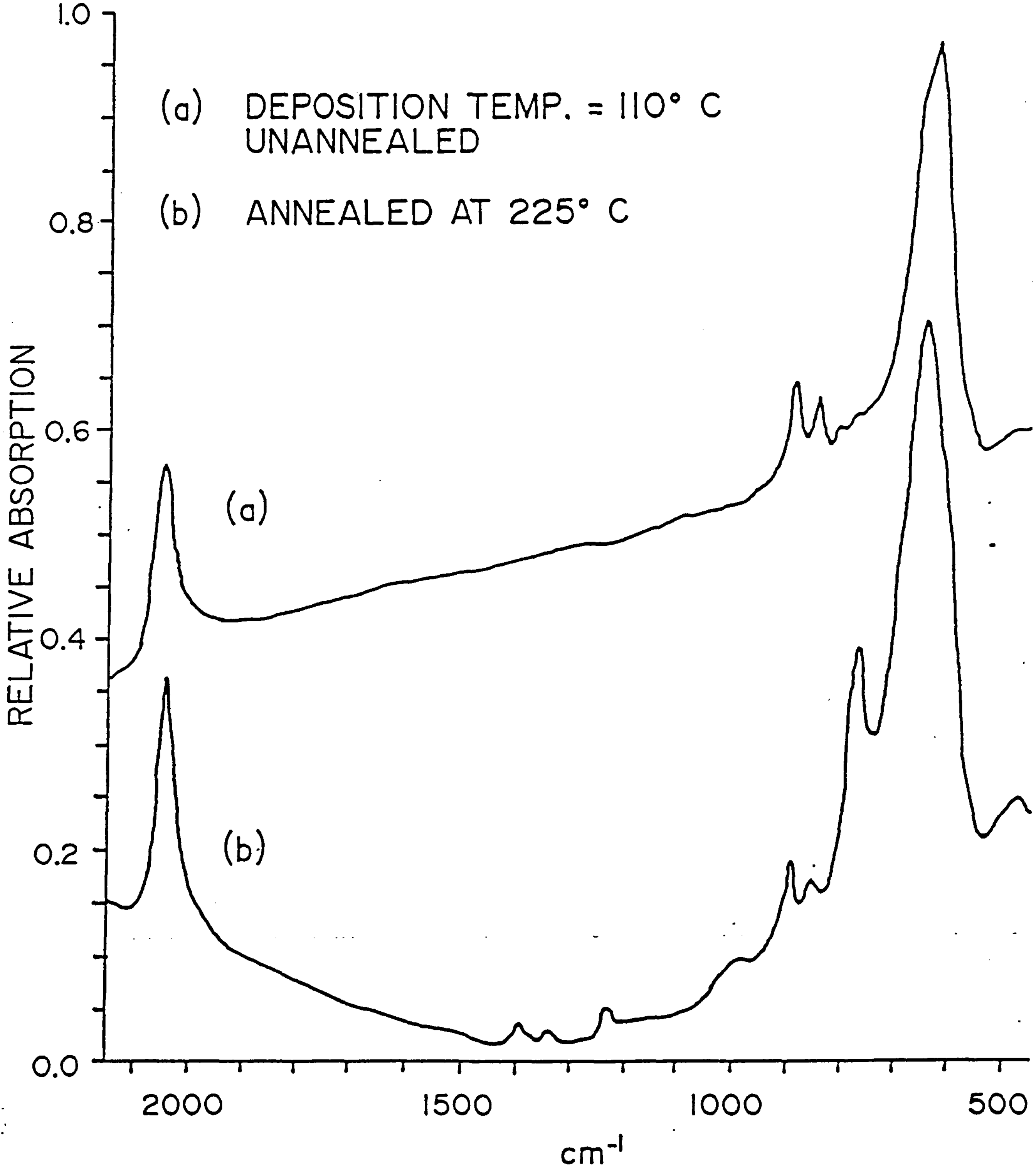

During the course of monitoring the annealing of Al contacts to p-i-n cells, it was found that contacts to microcrystalline n+ layers were, under some circumstances, more stable with temperature than those to amorphous n+ layers. This work has lead to improved n-layers, deposited with a specific chemical composition which yield a significant improvement. A search of the literature is now being conducted to determine if a patent of this technology is warranted.

2.5 HIGH EFFICIENCY DEVICE RESEARCH

2.5.1 Introduction

The high efficiency device program has focused on the development of amorphous silicon-carbon and amorphous silicon-germanium single and stacked junction solar cells. We have explored a-SiC:H single junction cells in the bandgap range of 1.7eV to 2.0ev and a-SiGe:H single junction cells in the bandgap range of 1.7eV to 1.5eV. Multi-junction cells with the combination of a-SiC:H, a-Si:H, and a-SiGe:H have been prepared.

2.5.2 Role of Interfaces in Amorphous Silicon-Germanium Single Junction Cells

Efficient a-SiGe:H alloy solar cells not only require the development of device quality intrinsic films but also require the development of appropriate doped layers and optimization of several interfaces in the device structure. The doped layers establish the built-in field which influences the collection of carriers since their transport is field assisted. The interfaces can act as recombination centers or barriers to the transport of carriers.

During this period we have concentrated our efforts in depositing 1.5eV bandgap a-SiGe:H alloy films from a variety of feedstocks and diluents. The opto-electronic properties of these films will be discussed elsewhere.

Single junction a-SiGe:H p-i-n solar cells have been fabricated in which the optical bandgap of the i-layer is either 1.55eV or 1.5eV. These alloys are deposited by dc glow discharge from a gaseous mixture of silane and germane. In the structure of the device, shown in Figure 2.5.2-1, we have studied the role of two interfaces and the effect of the n-layer on the performance of the devices. The first interface is between the a-Si:H buffer layer and the bulk a-SiGe:H i-layer and the second interface is between the bulk a-SiGe:H i-layer and the n-layer. The opto-electronic properties of a-SiGe:H and a-Si:H n-layers and its effect on the device performance has been evaluated. Low-level doping of a-SiGe:H alloys with boron has been explored

FIGURE 2.5.2-1. SCHEMATIC ILLUSTRATION OF THE SILICON-GERMANIUM PIN DEVICE.

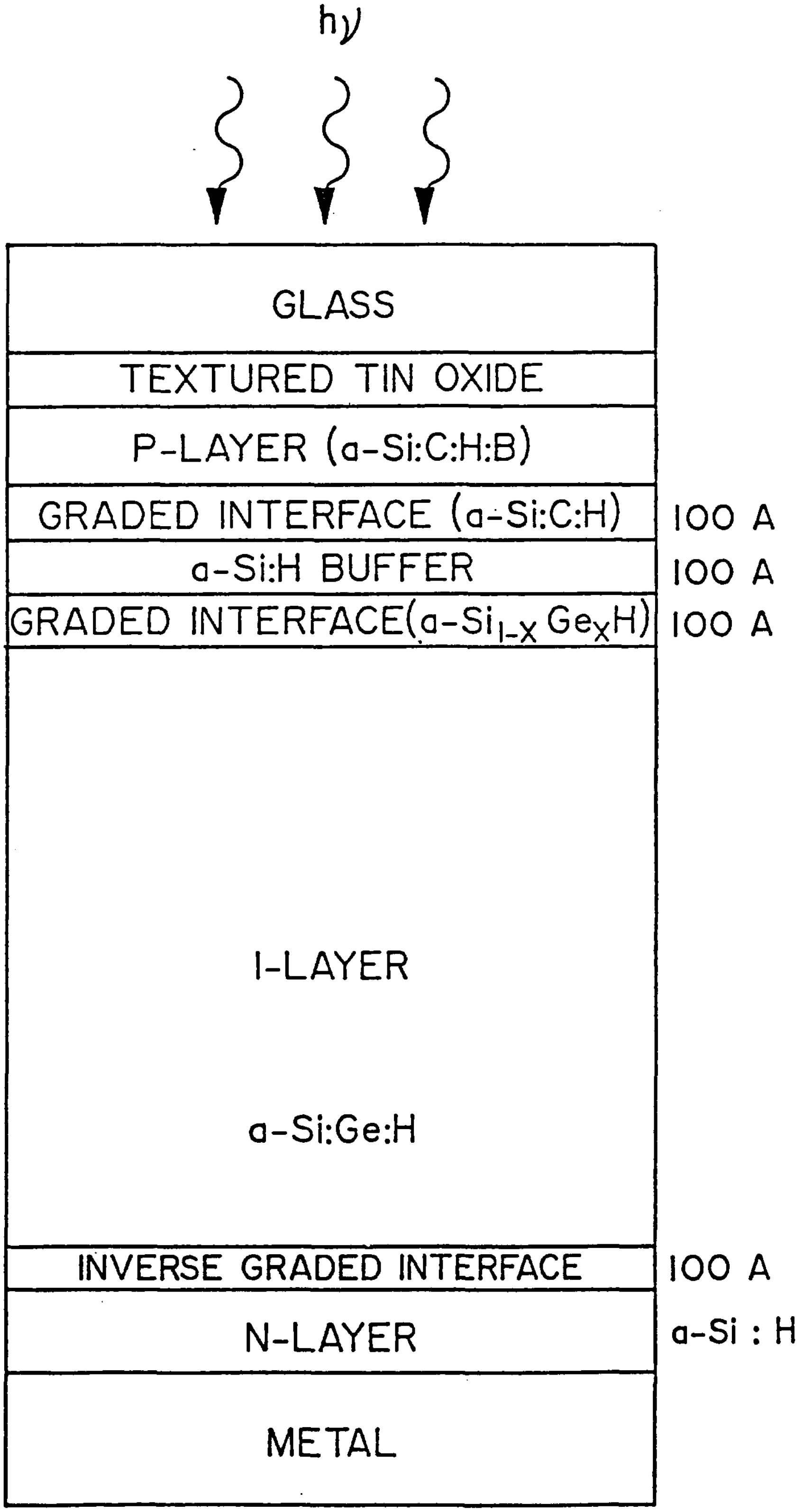

FIGURE 2.5.2-2. QE(0.6V)/QE(0V) FOR SOLAR CELLS WITH AND WITHOUT IGI (SEE TEXT).

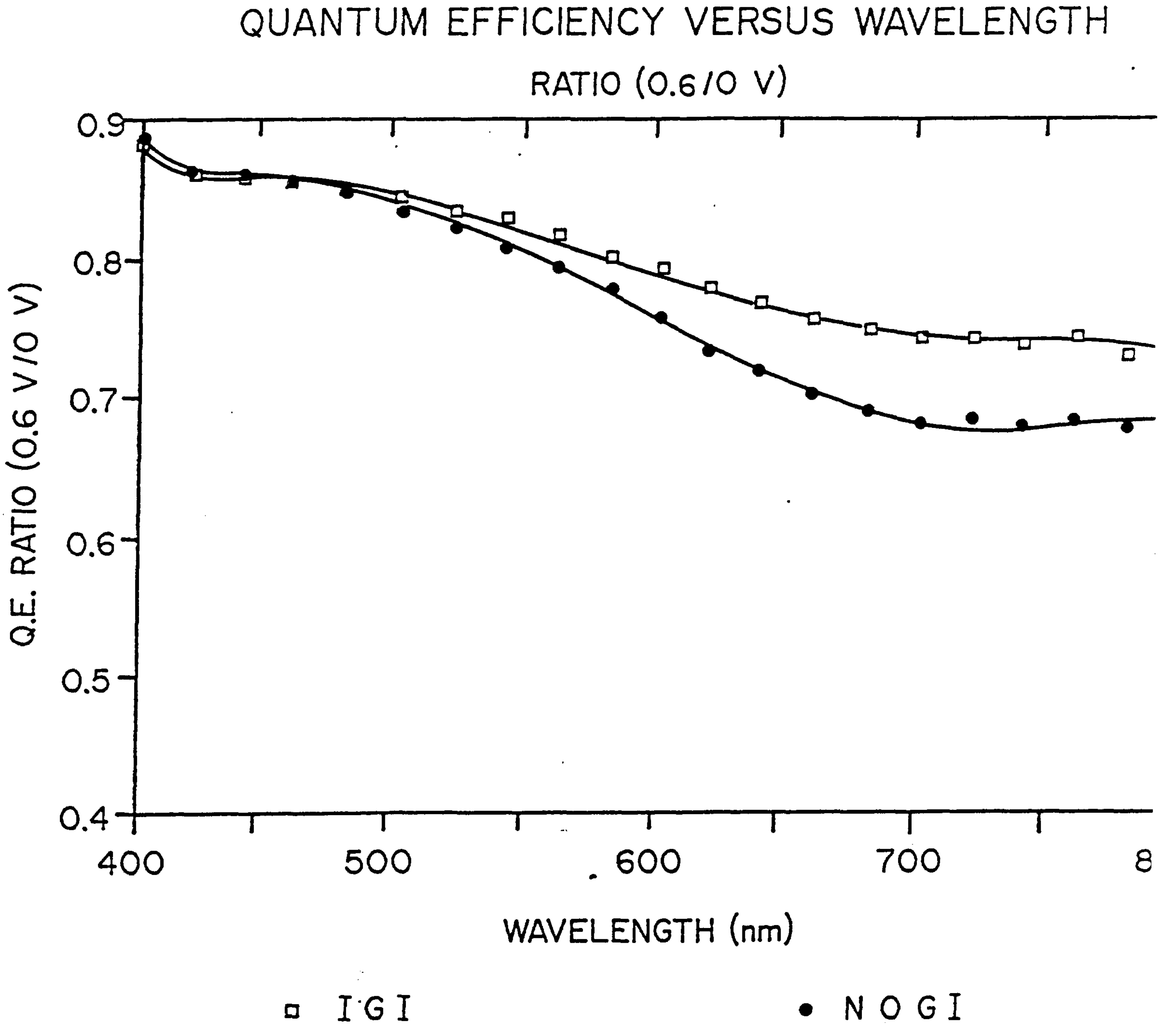

and its effect on film properties and devices has been studied.

In single junction a-SiGe:H solar cells we have employed the same p-layers and the same p/i graded interface as those used in our high efficiency a-Si:H single junction cells. The concept of p/i graded interface has been extended to the interface between the a-Si:H and a-SiGe:H i-layer. This graded interface (GI2), which is about 100Å thick, is deposited by changing the gas ratio of silane and germane such that the bandgap changes from 1.7eV to either 1.55eV or 1.5eV, reducing carrier recombination. An abrupt transition from a-Si:H (1.7eV) to a-SiGe:H (1.55eV or 1.5eV) can be increase the density of recombination centers at the interface. Moreover, if the electron affinity does not change as the Ge content is increased in a-SiGe:H alloys but the valence band moves up in energy, this interface can create a barrier to the transport of holes. We have studied the effect of depositing an inverse graded interface (IGI) at the a-SiGe:H/n interface. This layer is about 50-100Å thick and is deposited by changing the ratio of silane and germane in such a manner that the bandgap changes from either 1.55eV or 1.5eV to 1.7eV over this interface layer. The effect of employing an IGI can be seen in the improvements of the photovoltaic parameters as well as in the bias dependency of quantum efficiency measurements. The photovoltaic parameters of two identical a-SiGe:H cells (E_g = 1.55eV), with and without IGI are tabulated in Table 2.5.2-1. Figure 2.5.2-2 shows the ratio of quantum efficiency measurements at 0.6V and at 0V for these two solar cells. It is evidence that employing an IGI improves the collection of long wavelength carriers which also manifests as an improvement in the fill-factor of the devices.

2.5.3 SiGe n-layers

n-type doped layers were deposited by dc glow-discharge from a mixture of silane, germane, and phosphine or from a mixture of silane and phosphine. The films were characterized by optical bandgap measurements, photo-thermal deflection spectroscopy (PDS), dark conductivity and temperature dependence of dark conductivity. Single junction p-i-n solar cells were fabricated with a-SiGe:H i-layers (Eg = 1.55eV) which had either a-SiGe:H n-layers or a-Si:H n-layers. The electrical and optical properties of a-Si:H and a-SiGe:H n-layers are tabulated in Table 2.5.3-1 and the photovoltaic parameters of devices with these n-layers are tabulated in Table 2.5.3-2. The dark conductivity of a-SiGe:H n-layer is found to be about an order of magnitude lower than that of a-Si:H n-layer. Moreover, the conductivity activation energy (E_a) of the a-SiGe:H n-layer was 0.299eV as compared to 0.207eV for the a-Si:H n-layer which clearly demonstrates the inferior doping characteristics of a-SiGe:H

Table 2.5.2-1

Comparison of AM1.5 current-voltage characteristics of devices with and without IGI (see text)

Cell # (mV)	Voc (mA/cm^2)	Jsc	FF (%)	Eff	Remarks
LL724423	852	17.7	0.548	8.26	NO IGI
LL724443	842	17.7	0.584	8.70	WITH IGI

Table 2.5.3-1

Electrical and Optical properties of n-layers

Property	a-Si:H	a-SiGe:H
Optical Bandgap	1.71eV	1.54eV
Dark Conductivity	6.4 X 10^{-3}ohm-cm	3.1 X 10^{-4}ohm-cm
Activation Energy	0.207eV	0.299eV

Table 2.5.3-2

Photovoltaic parameters of a-SiGe:H cells with different n-layers

Cell #	Voc (mV)	Jsc (mA/cm^2)	FF	Efficiency (%)	n-layer
LL724422	834	19.23	0.629	10.08	a-Si:H
LL724431	822	18.03	0.519	7.69	a-SiGe:H

FIGURE 2.5.3-1. J-V CHARACTERISTICS OF PIN SOLAR CELLS WITH a-Si:H (A) AND a-SiGe:H (B) N-LAYERS.

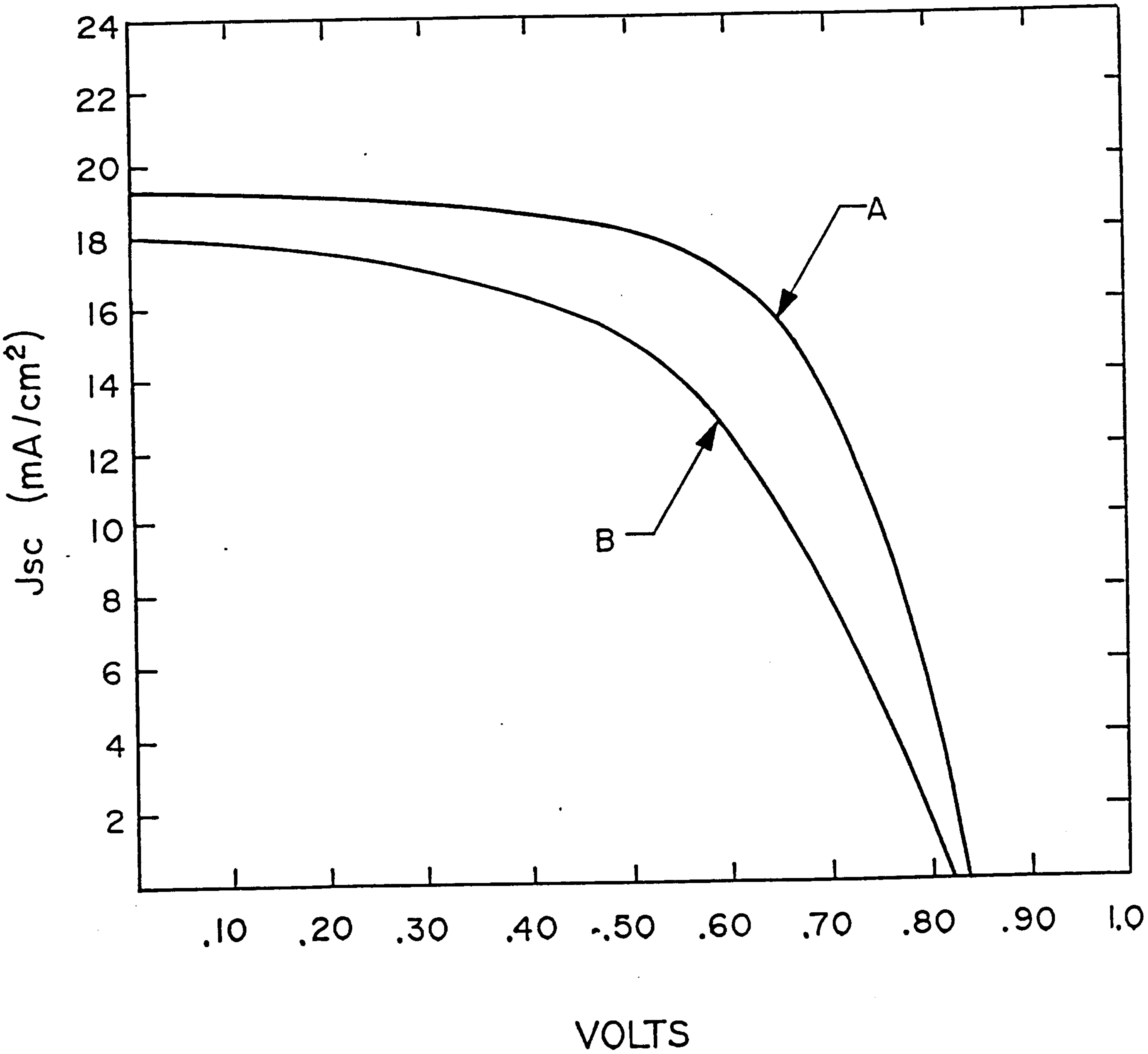

FIGURE 2.5.3-2. QUANTUM EFFICIENCY OF DEVICES WITH a-Si:H AND a-SiGe:H N-LAYERS.

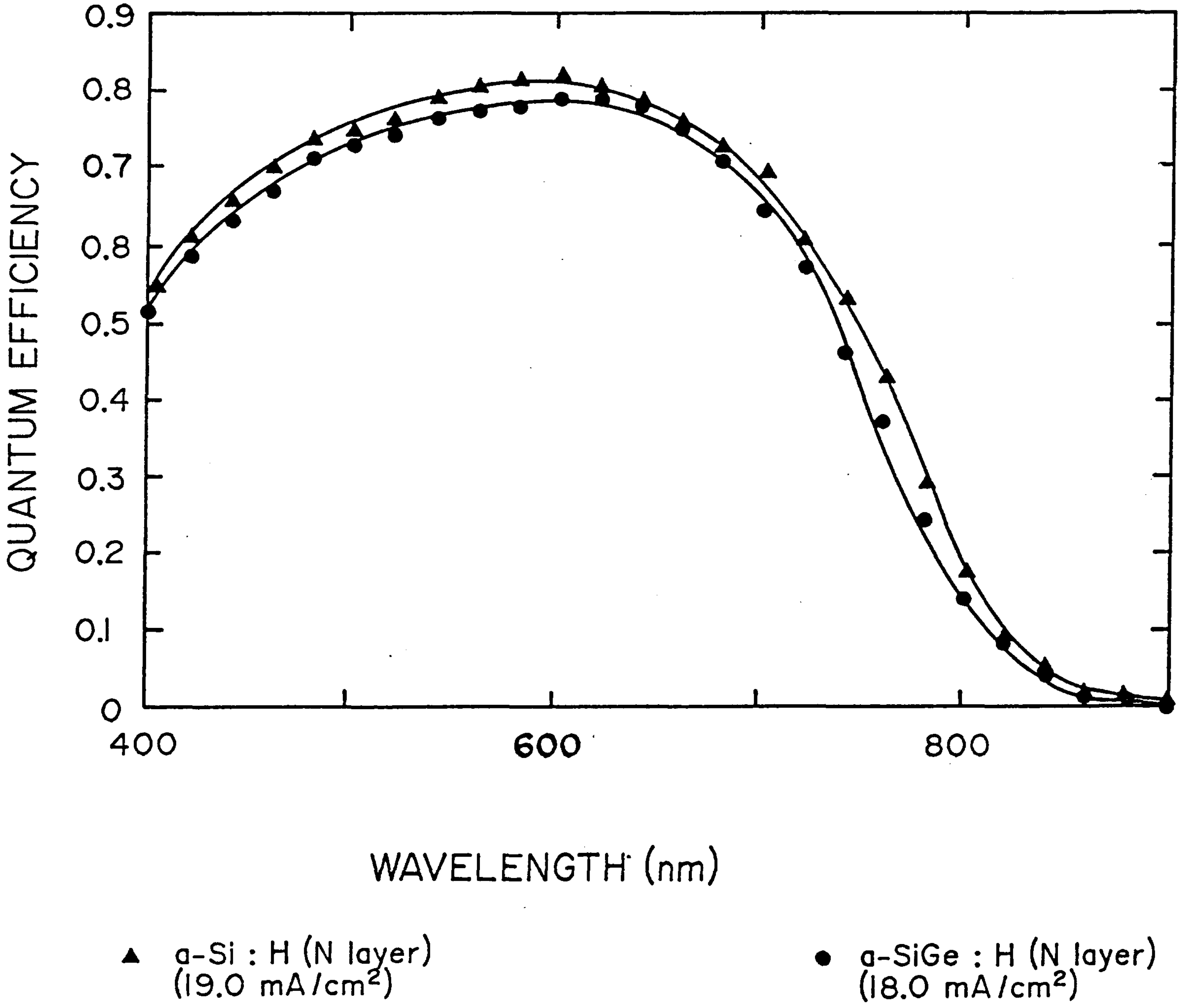

FIGURE 2.5.3-3. QE(0.6V)/QE(0V) FOR PIN CELLS WITH a-Si:H AND a-SiGe:H N-LAYERS.

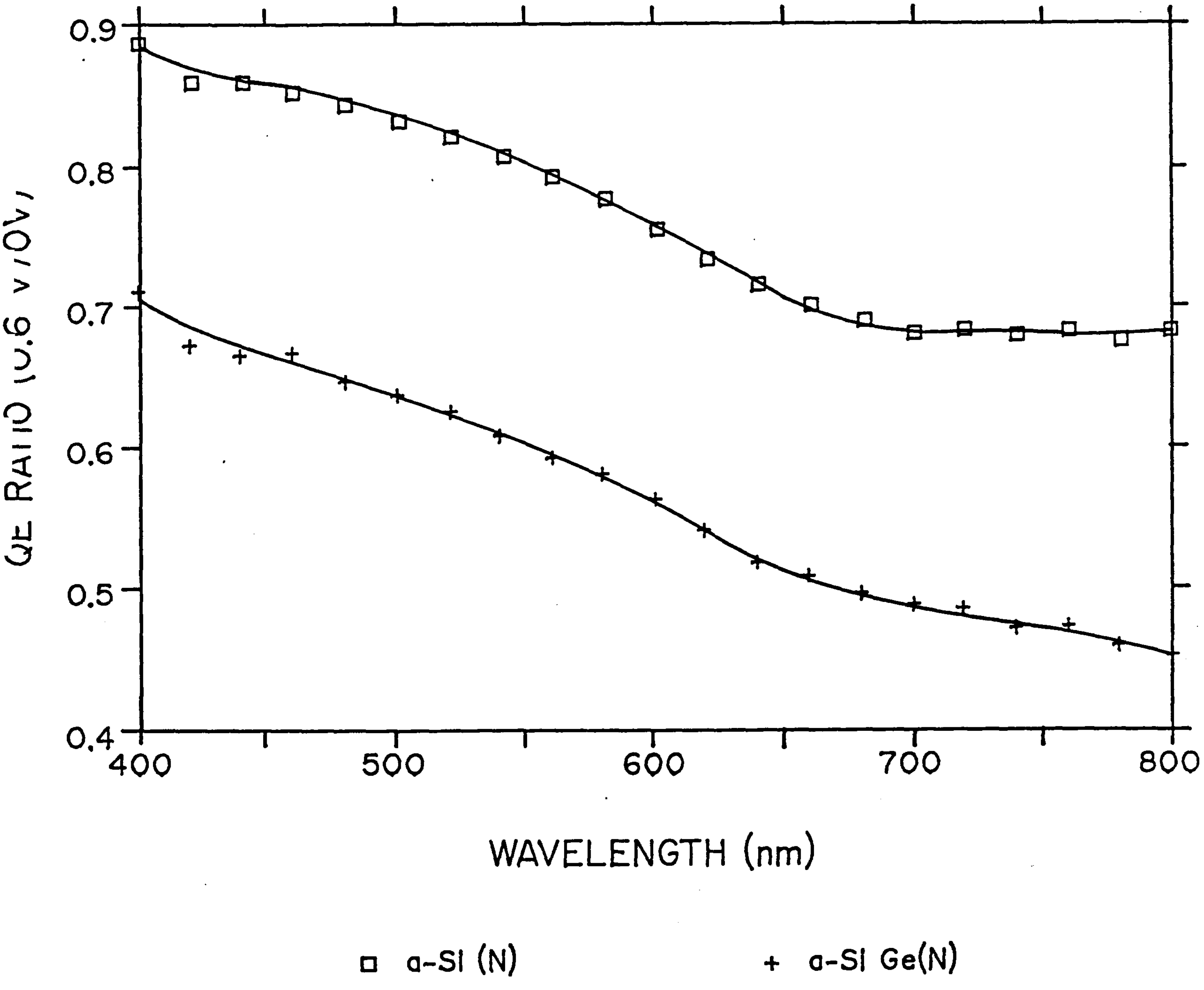

n-layers. It is possible that in a-SiGe:H films the formation of defects with an energy in the mid-gap region compensates the dopants and pulls the Fermi level towards the mid-gap. In p-i-n solar cells we found that using a-Si:H n-layers produced small differences in the open-circuit voltage but the short-circuit current and the fill-factor were far superior than that of devices with a-SiGe:H n-layers. Figure 2.5.3-1 shows the J-V characteristics under global AM1.5 illumination of the two cells with different n-layers. Figure 2.5.3-2 shows the external quantum efficiency as a function of wavelength of the same two devices. In these devices, the difference in the Jsc values can be explained in terms of the optical losses due to absorption in the respective n-layers (Eg = 1.54eV for a-SiGe:H and Eg = 1.7eV for a-Si:H n-layer). The small difference in Voc and the poor fill-factor are probably due to the inferior doping characteristics of a-SiGe:H n-layer. A poorer doped n-layer can lead to less band-bending at the i/n interface, a lower value of flat-band voltage and consequently a lower fill-factor. The hypothesis of less band-bending at the i/n interface is somewhat evident in the quantum efficiency measurements made with applied forward bias. In forward bias the built-in field is reduced. If this reduction in the field strength is uniform one would expect little wavelength dependence in the collection of carriers. In a-SiGe:H devices there is a strong bias dependence on the collection of long wavelength carriers which indicates a hole transport limitation due to low product of holes. In these devices the same trend is seen but cells with a-SiGe:H n-layer have a much larger bias dependence than that of cells that of cells with a-Si:H n-layer. This is shown in Figure 2.5.3-3 where the ratio of quantum efficiency versus wavelength measurements at 0.6V to that at 0V is plotted for the two types of cells.

2.5.4 Low-level Boron Doping of SiGe:H Films

In order to improve the hole transport properties of a-SiGe:H alloys we have explored low-level boron doping of i-layers and studied its effect on transport properties and devices. Boron doping in the range of 0-10 ppm was accomplished by deposition from a gaseous mixture of silane, germane, and 38 ppm of boron trifluoride mixed with silane. Figures 2.5.4-1(a), (b), (c) and (d) show the effect of boron doping on the dark conductivity, the conductivity activation energy, the photo-conductivity, and the ratio of photo to dark conductivity respectively of 1.55eV bandgap a-SiGe:H i-layers. As the doping is increased from 0 to 10 ppm the dark conductivity decreases from $2X10^{-10}$(ohm-cm)$^{-1}$ to 8X 10^{-12}(ohm-cm)$^{-1}$, the conductivity activation energy increases from 0.76eV to 0.89eV, the photo-conductivity decreases from 2X 10^{-6}(ohm-cm)$^{-1}$ to $4X10^{-7}$(ohm-cm)$^{-1}$ but the ratio of dark to photo conductivity increases from $8X10^{3}$ to $5X10^{4}$. The decrease in dark conductivity with an increase in the activation energy indicates that the Fermi level is moving towards the valence

FIGURE 2.5.4-1. a,b,c,d EFFECT ON LOW LEVEL BORON DOPING OF 1.55eV a-SiGe:H ALLOY FILMS ON a) DARK CONDUCTIVITY, B) CONDUCTIVITY ACTIVATION ENERGY, C) PHOTOCONDUCTIVITY AND D) RATIO OF PHOTO TO DARK CONDUCTIVITY.

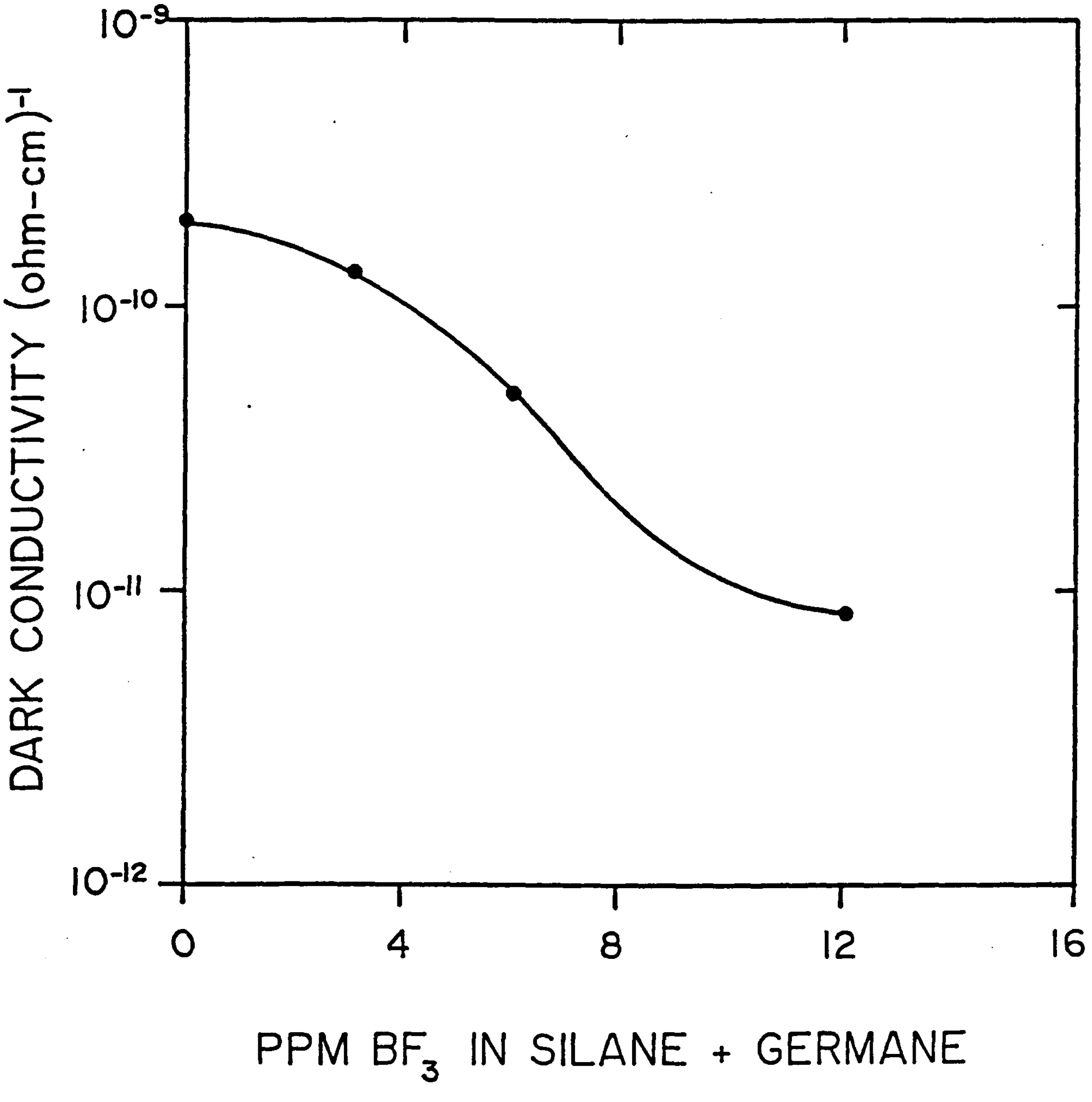

FIGURE 2.5.4-1. a,b,c,d EFFECT OF LOW LEVEL BORON DOPING OF 1.55eV a-SiGe:H ALLOY FILMS ON A) DARK CONDUCTIVITY, B) CONDUCTIVITY ACTIVATION ENERGY, C) PHOTOCONDUCTIVITY AND D) RATIO OF PHOTO TO DARK CONDUCTIVITY.

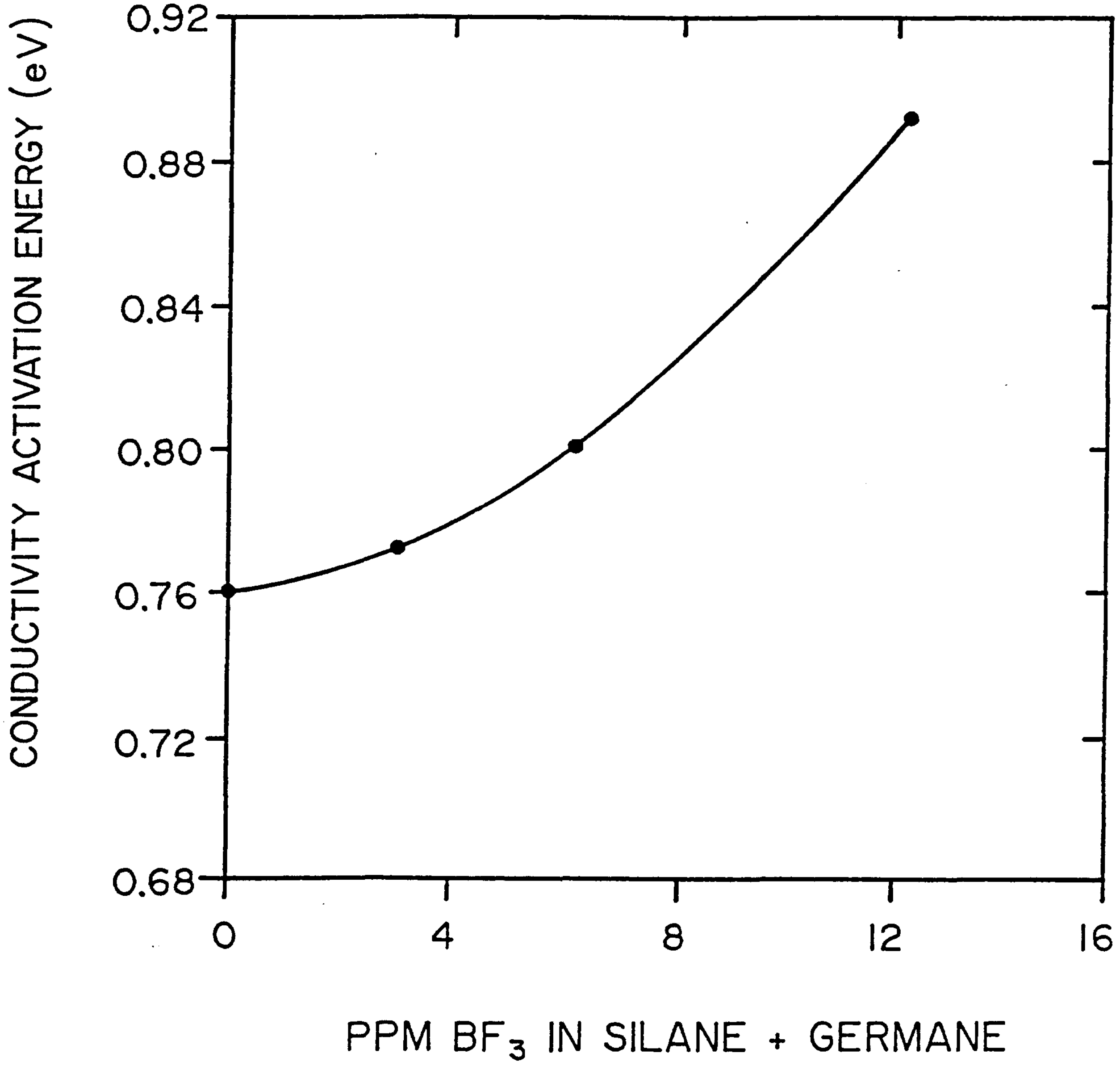

FIGURE 2.5.4-1. EFFECT OF LOW LEVEL BORON DOPING OF 1.55eV a-SiGe:H ALLOY FILMS
a,b,c,d ON A) DARK CONDUCTIVITY, B) CONDUCTIVITY ACTIVATION ENERGY, C) PHOTOCONDUCTIVITY AND D) RATIO OF PHOTO TO DARK CONDUCTIVITY.

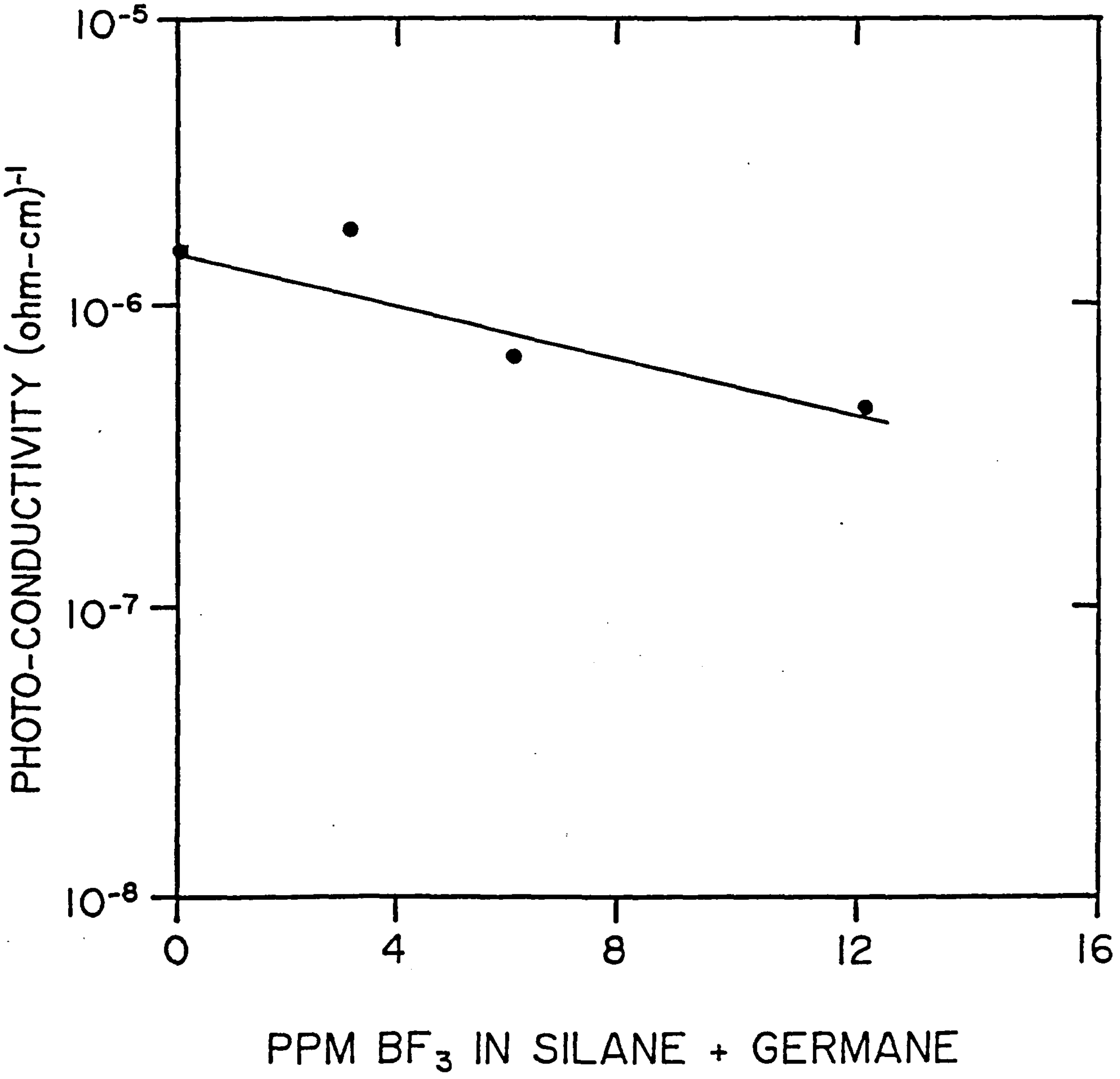

FIGURE 2.5.4-1. EFFECT OF LOW LEVEL BORON DOPING OF 1.55eV a-SiGe:H ALLOY FILMS
a,b,c,d ON A) DARK CONDUCTIVITY, B) CONDUCTIVITY ACTIVATION ENERGY, C) PHOTOCONDUCTIVITY AND D) RATIO OF PHOTO TO DARK CONDUCTIVITY.

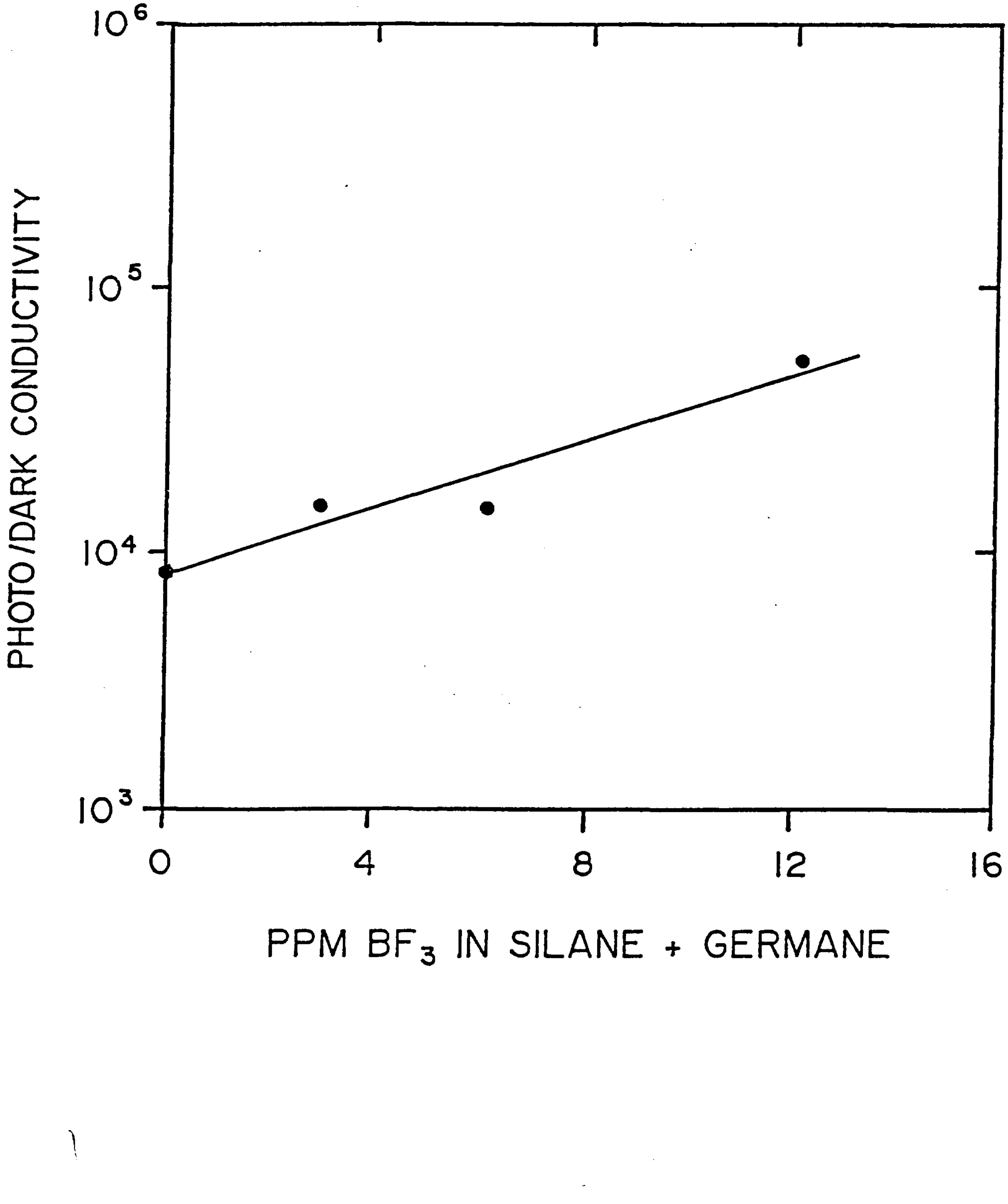

band. The undoped material is slightly n-type. Figures 2.5.4-2(a) and (b) show the J-V characteristics of two p-i-n a-SiGe:H devices with 0 and 6 ppm boron doping (gas phase) of the i-layer. Even though the total short-circuit current density is less for the boron doped cell the fill-factor is superior. Figure 2.5.4-3 shows the quantum efficiency measurements of these two devices. Due to boron doping the blue response is lower but the red response is increased. Figures 2.5.4-4 (a) and (b) show the J-V characteristics of the same two devices measured under orange illumination (beyond 600nm). It is clear that the cell with boron doping not only has higher Jsc but also higher fill-factor. These results were obtained with uniform doping of the i-layer. Optimization of doping characteristics are underway and ultimately one would like to use boron grading in the i-layer.

The best single junction a-SiGe:H cell in which the i-layer had an optical bandgap of 1.55eV had a conversion efficiency of 10.1% with short-circuit current density of 20mA/cm^2. Figure 2.5.4-5 shows the J-V characteristics of this device and Figure 2.5.4-6 shows the quantum efficiency versus wavelength measurement. This device has a response of 75% at 700nm and 20% at 800nm. The best device fabricated with 1.5eV bandgap material had a conversion efficiency of 8% (no AR coating) with short-circuit current density of 19.5mA/cm^2. Figure 2.5.4-7 shows the J-V characteristics of this device and Figure 2.5.4-8 shows the corresponding quantum efficiency versus wavelength measurement made at 0 bias. This device exhibited 33.7% response at 800nm. Under reverse bias this device generates 21.4mA/cm^2 current with 76.7% response at 700nm and 36.9% response at 800nm. Figure 16 shows the quantum efficiency measurements of this device under -3V bias.

2.5.5 Amorphous Silicon-Carbon Single Junction Cells

During this period we have studied a-SiC:H alloys deposited from a large variety of feedstocks, diluents, and under various deposition conditions. The material properties of these films are discussed in a later section.

Single junction p-i-n solar cells were fabricated in which the i-layer consists of a-SiC:H deposited from a gaseous mixture of silane and methane. The photovoltaic parameters of the best cells fabricated with different i-layer bandgaps are tabulated in Table 2.5.5-1. The J-V characteristics of three cells are shown in Figure 2.5.5-1.

FIGURE 2.5.4-2. a,b J-V CHARACTERISTICS OF a-SiGe DEVICES WHOSE I-REGIONS WERE A) UNDOPED AND B) DOPED WITH 6ppm BF_3.

Cell No. A8123-2-IS3RI
Voc = -.811 Volts
F.F. = .576
Power = 8.61 mw/cm^2
V (max) = -.582 Volts
Rs = 8.90E + 00 ohm-cm^2
Rscc = .99
Temp. = 27.3° C

DATE - 5/4/88
Jsc = 13.42 ma/cm^2
Eff = 8.61%
Illum. = 99.15 mw/cm^2
J (max) = 14.88 ma/cm^2
Rsh = 3.46E + 03 ohm-cm^2
Rshcc = 0.00
I T O = 0.00E + 00 ohm/cm^2

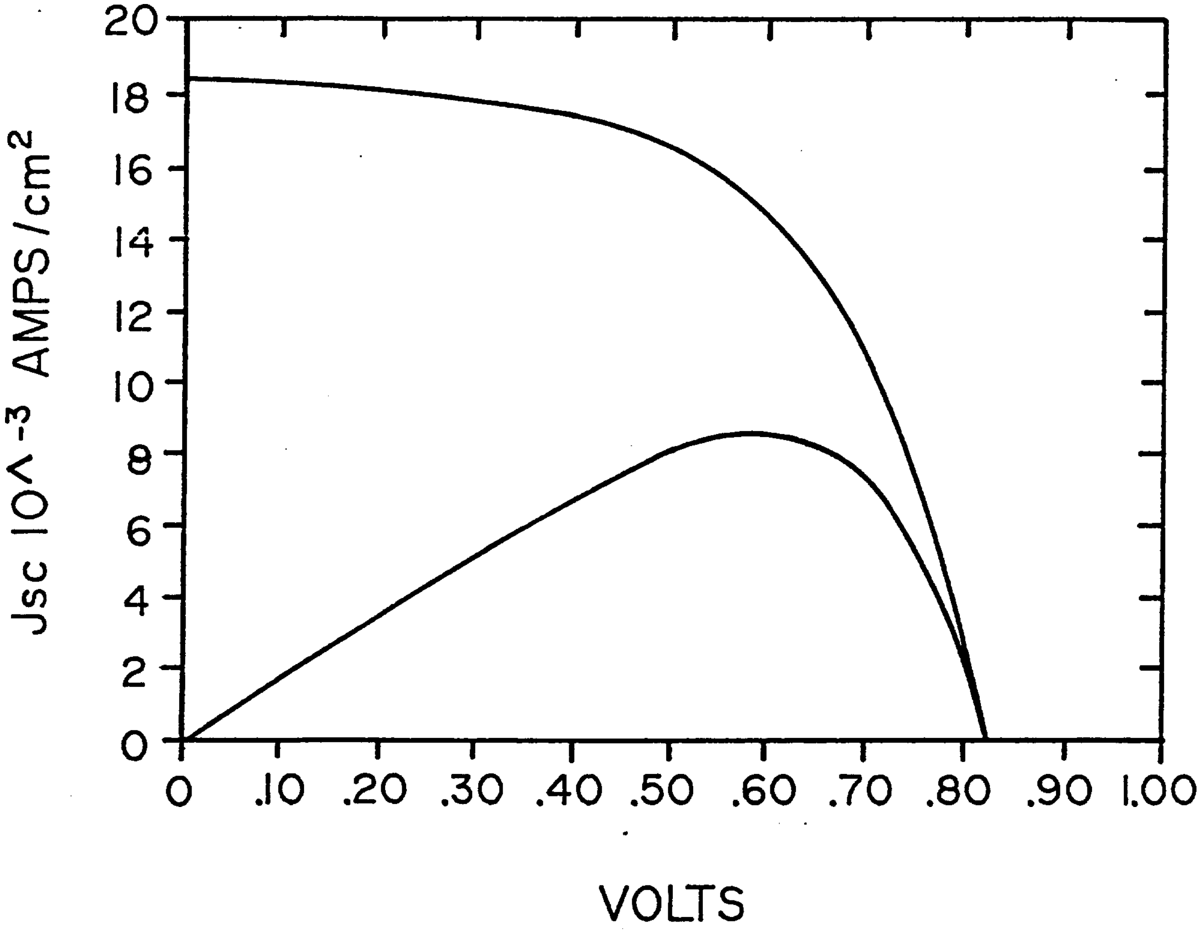

FIGURE 2.5.4-2. J-V CHARACTERISTICS OF a-SiGe DEVICES WHOSE I-REGIONS WERE
a,b A) UNDOPED AND B) DOPED WITH 6ppm BF_3.

Cell No. A8119-2-2 S3R1
Voc = -.772 Volts
F.F. = .612
Power = 8.31 mw/cm^2
V (max) = -.583 Volts
Rs = 6.88E + 00 ohm-cm^2
Rscc = 1.00
Temp. = 35.4° C

DATE - 5/4/88
Jsc = 17.61 ma/cm^2
Eff = 3.31%
Illum. = 104.65 mw/cm^2
J (max) = 14.26 ma/cm^2
Rsh = 5.65E + 02 ohm-cm^2
Rshcc = 0.00
ITO = 0.00E + 00 ohm/cm^2

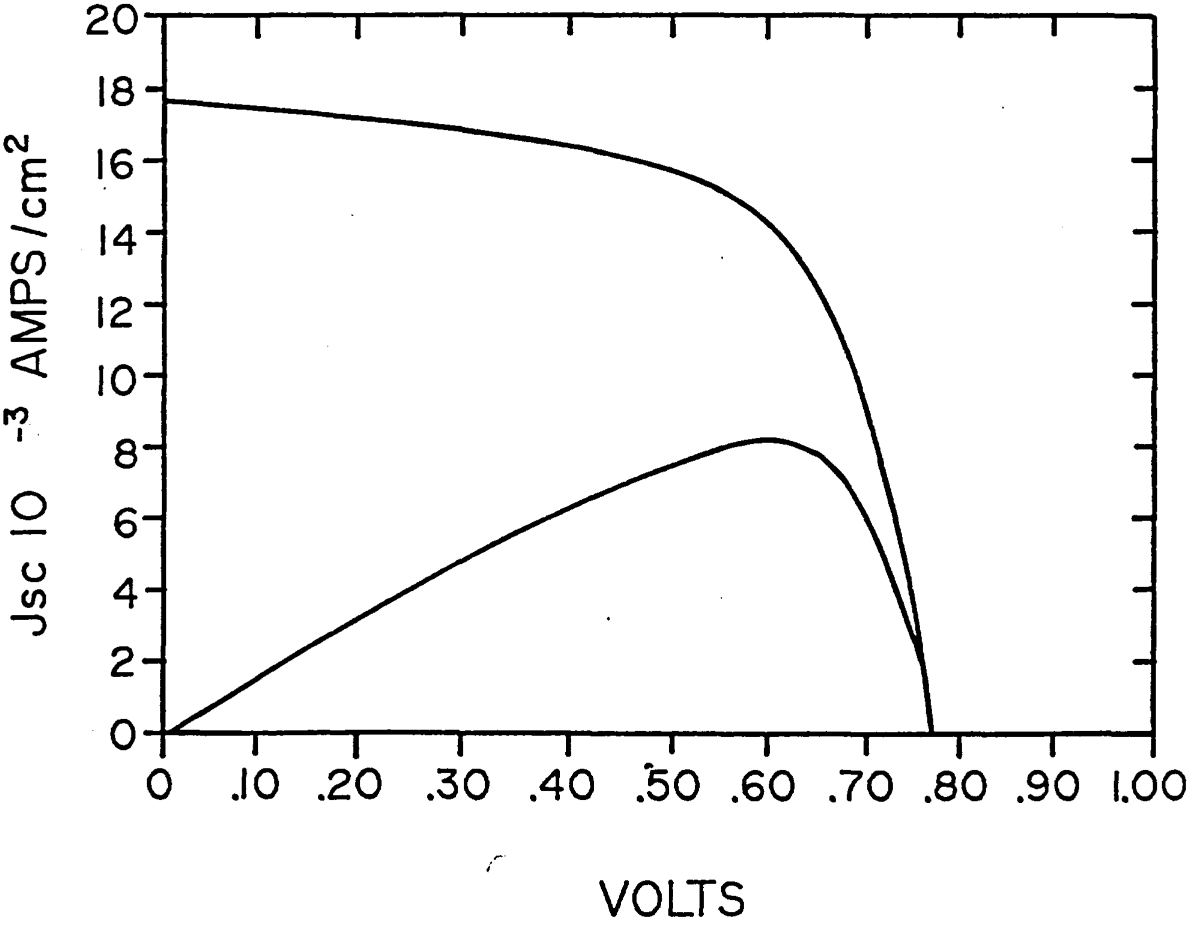

FIGURE 2.5.4-3. QUANTUM EFFICIENCY OF UNDOPED AND 6ppm BORON DOPED a-SiGe DEVICES. NOTE INCREASE IN RED RESPONSE OF BORON DOPED DEVICE.

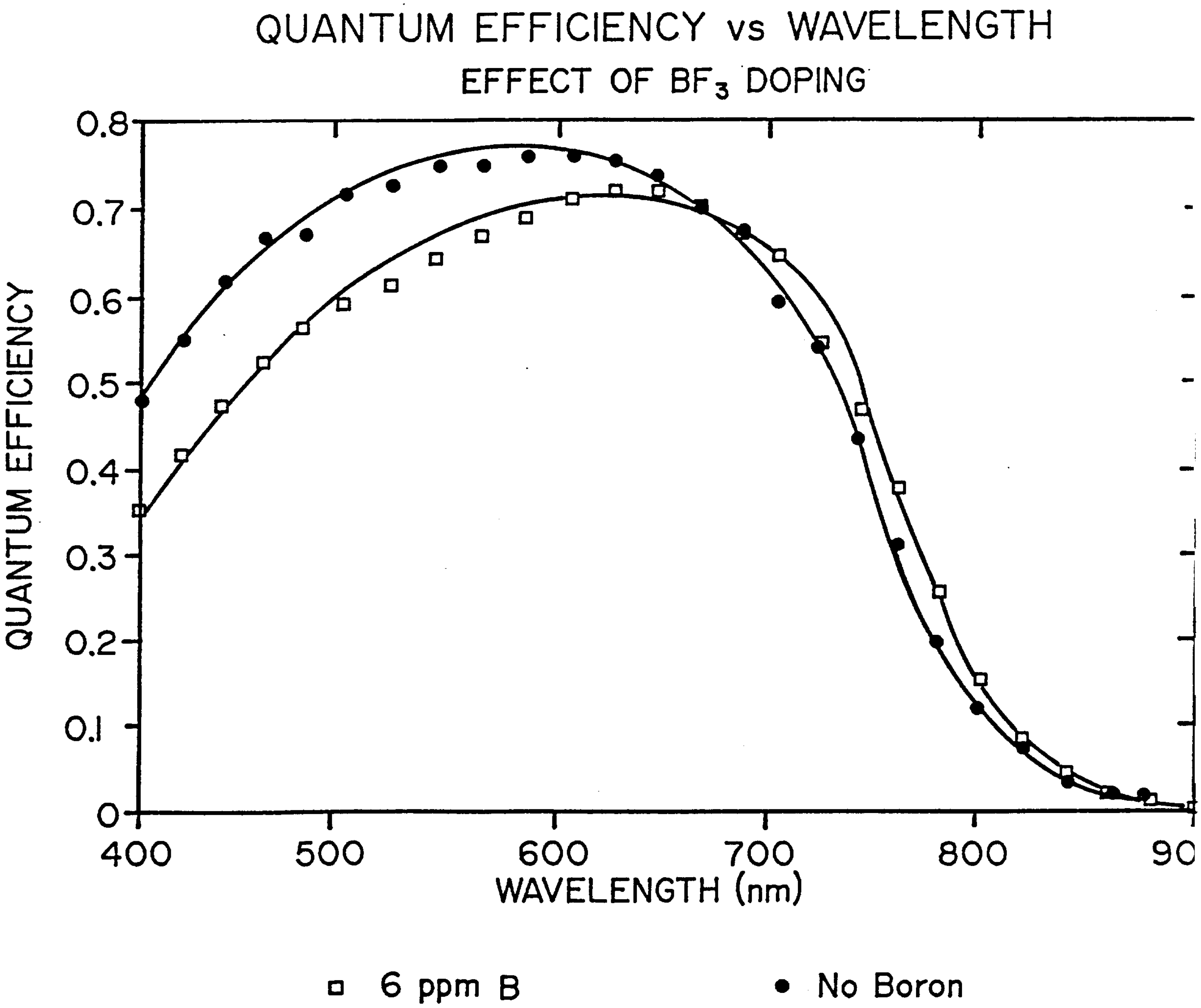

FIGURE 2.5.4-4. J-V CHARACTERISTICS OF UNDOPED AND BORON DOPED DEVICES UNDER ORANGE ILLUMINATION.

Cell No. = BF_3 = 0 Orange
Voc = -.761 Volts
F.F. = .579
Power = 3.82 mw/cm^2
V (max) = -.551 Volts
Rs = 1.46E + 01 ohm-cm^2

Date = 5/5/88
Jsc = 8.65 ma/cm^2
Eff = 3.82 %
Illum. = 102.61 mw/cm^2
J (max) = 5.92 ma/cm^2
Rsh = 1.15E + 03 ohm-cm^2

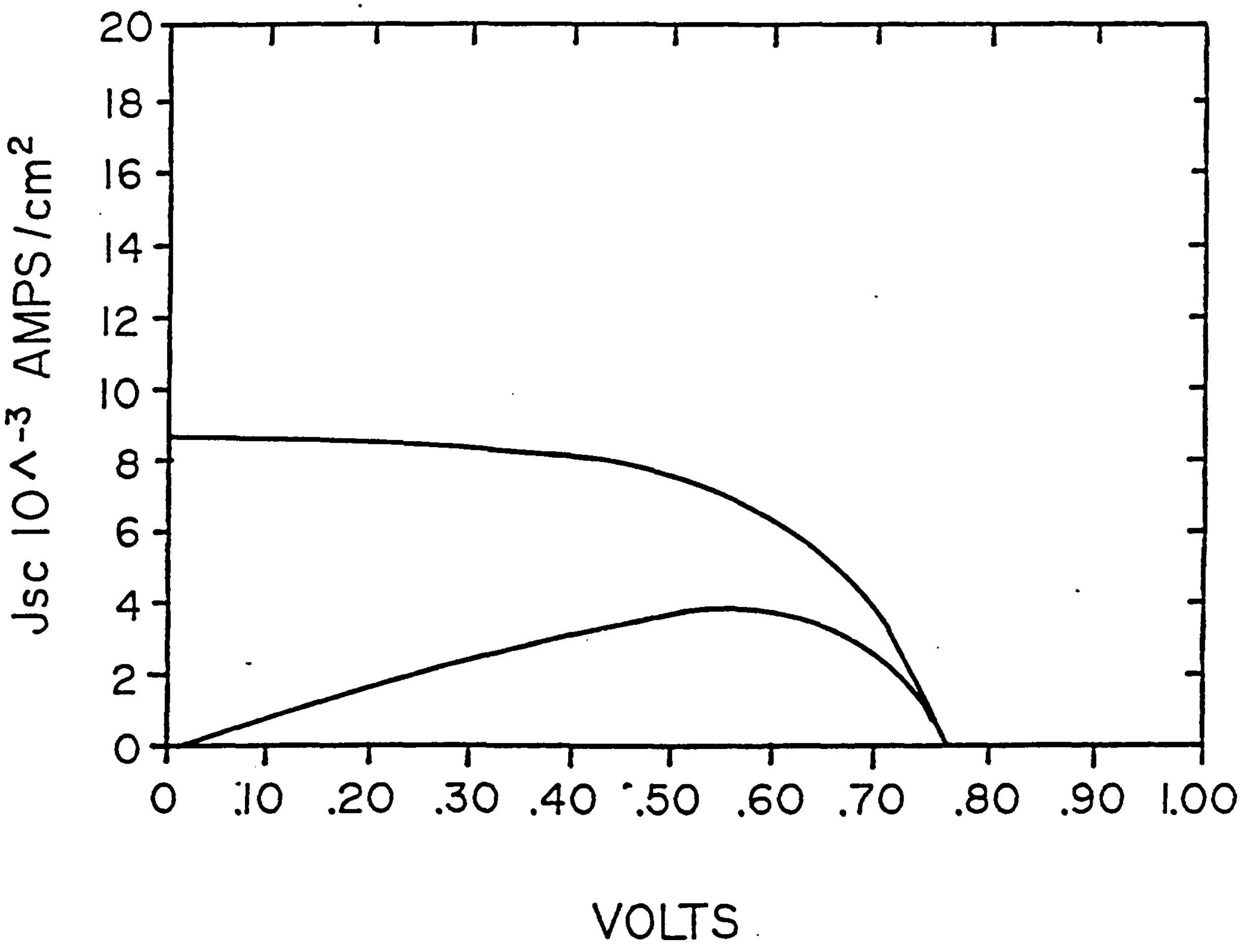

FIGURE 2.5.4-4. J-V CHARACTERISTICS OF UNDOPED AND BORON DOPED DEVICES UNDER ORANGE ILLUMINATION.

Cell No.	= BF_3 = 30 Orange	Date	= 5/5/88
Voc	= -.741 Volts	Jsc	= 9.06 ma/cm^2
F.F.	= .620	Eff	= 4.16 %
Power	= 4.16 mw/cm^2	Illum.	= 102.58 mw/cm^2
V (max)	= -.563 Volts	J (max)	= 7.40 ma/cm^2
Rs	= 1.10E + 01 ohm-cm^2	Rsh	= 5.93E + 02 ohm-cm^2

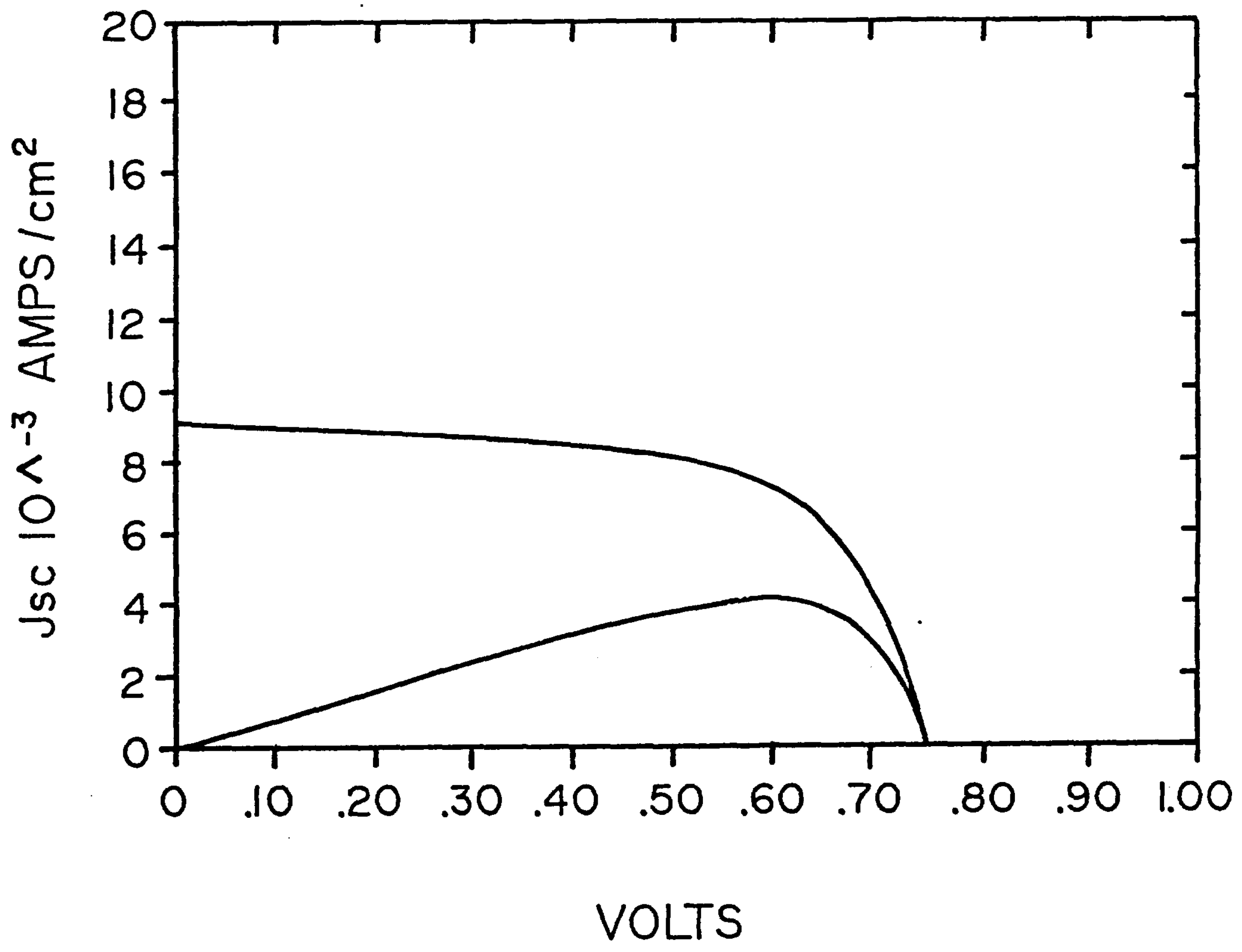

FIGURE 2.5.4-5. CURRENT-VOLTAGE CHARACTERISTICS OF 10.1% 1.55eV BANDGAP a-SiGe SOLAR CELL.

Cell No. A8068-2-3 S3R	Date 032188
Voc = -.823 Volts	Jsc = 20.08 ma/cm^2
F.F. = .611	Eff = 10.09 %
Power = 10.09 mw/cm^2	Illum. = 102.15 mw/cm^2
V max = -.608 Volts	J max = 16.60 ma/cm^2
Rs = 6.65 E + 00 ohm-cm^2	Rsh = 2.11E + 03 ohm-cm^2
Temp. = 28.5 deg. C	Cell Area = .260 cm^2

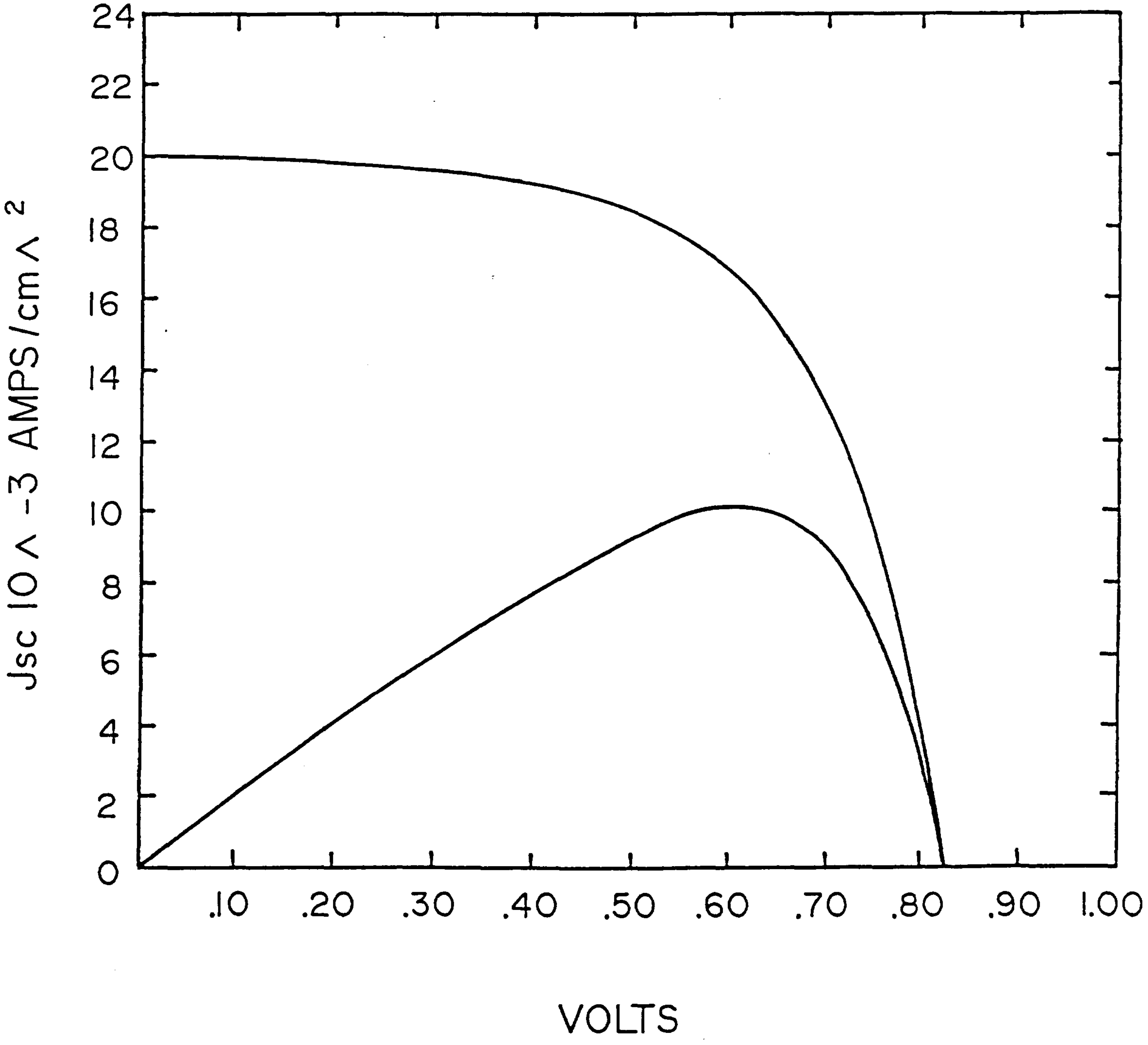

FIGURE 2.5.4-6. QUANTUM EFFICIENCY OF 10.1%, 1.55eV BANDGAP SiGe DEVICE.

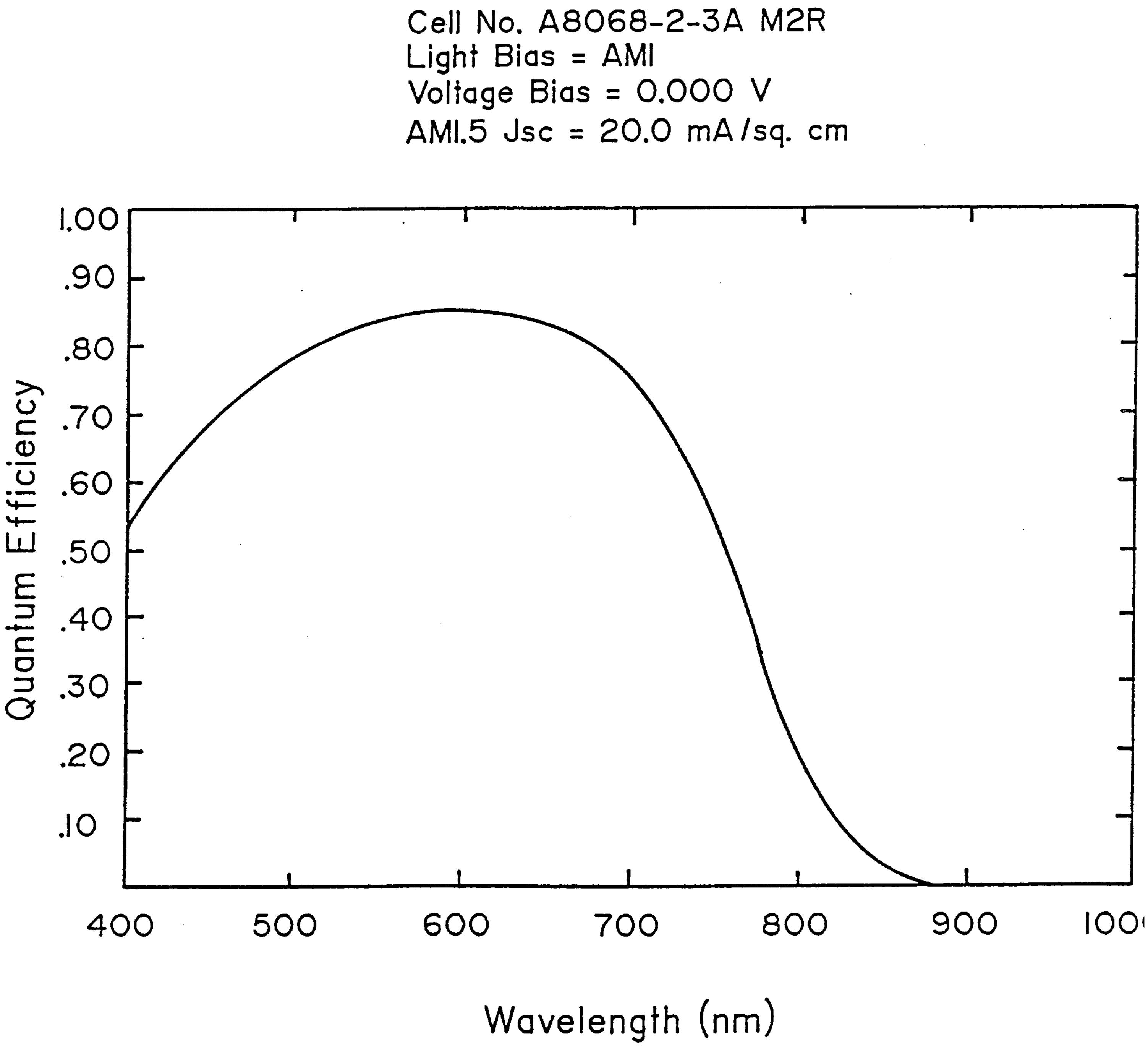

FIGURE 2.5.4-7. J-V CHARACTERISTICS OF 1.5eV BANDGAP SiGe DEVICE.

Cell No. = A8069-2-4 M2

Cell Area = .620 cm^2 Date = 3/21/88
Voc (I) = -.756 Volts No. of Segments = 1
Voc = -.752 Volts Jsc = 19.29 ma/cm^2
F.F. = .547 Eff = 7.93 %
Power = 7.93 mw/cm^2 Illum. = 102.11 mw/cm^2
V (max) = -.523 Volts J (max) = 15.17 ma/cm^2
Rs = 8.62E + 00 ohm-cm^2 Rsh = 4.46E + 02 ohm-cm^2
Rscc = 1.00 Rshcc = 0.00
Temp = 26.6° C ITO = 0.00E + 00 ohm/cm^2

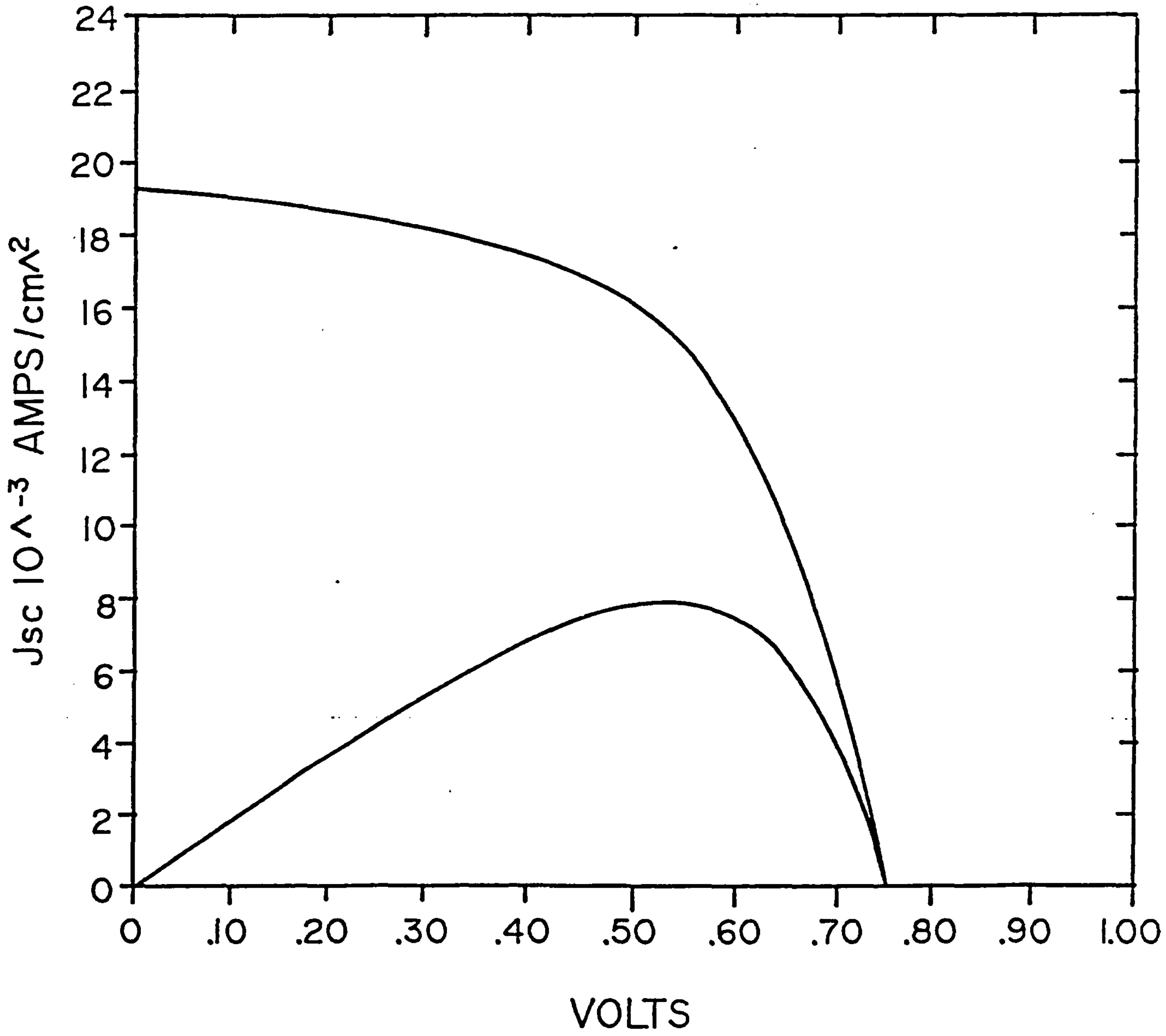

FIGURE 2.5.4-8. QUANTUM EFFICIENCY OF 1.5eV BANDGAP SiGe DEVICE.

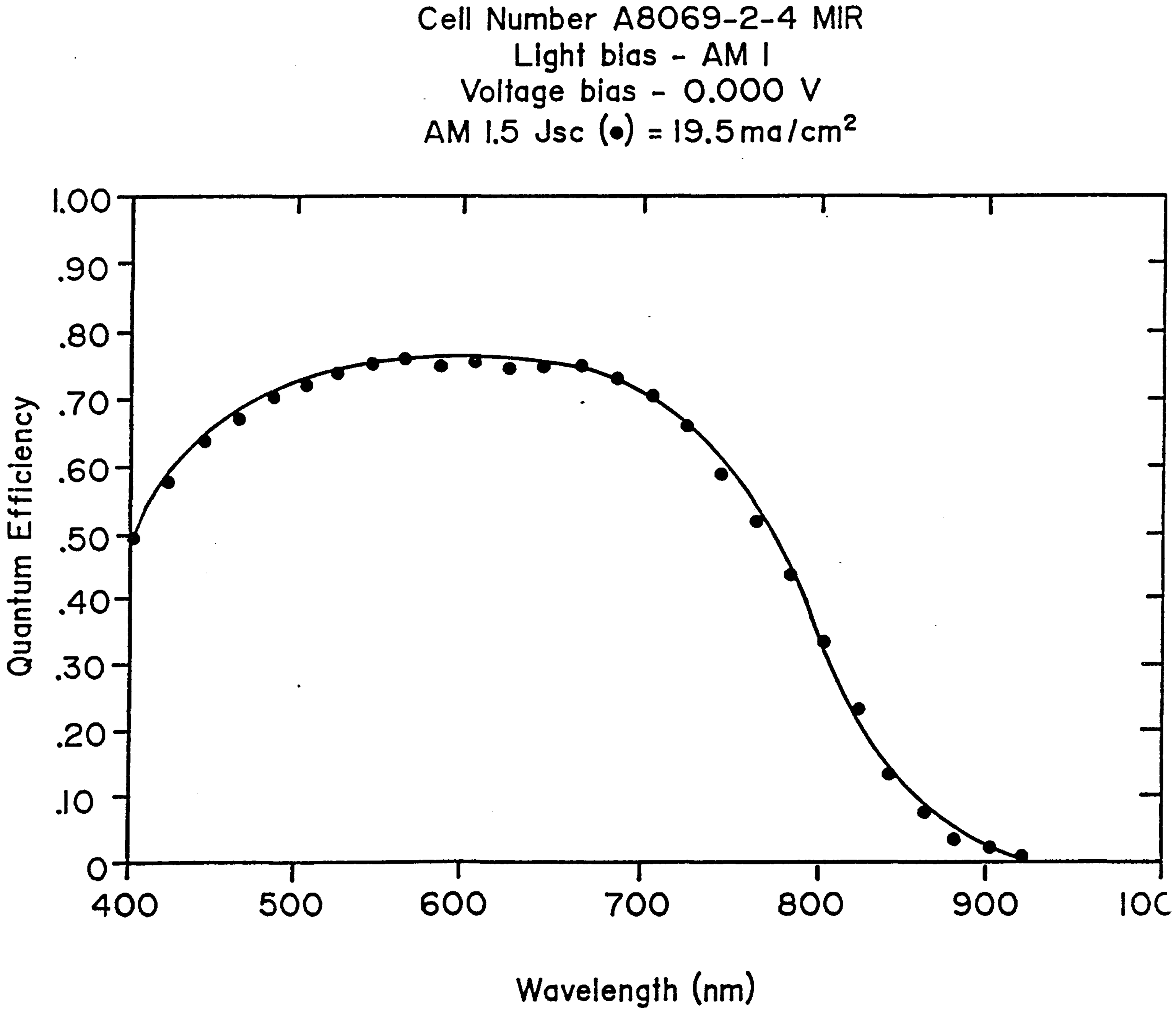

Table 2.5.5-1

Photovoltaic parameters of some a-SiC:H single junction cells

Cell #	Eg (eV)	Voc (mV)	Jsc (mA/cm2)	FF	Efficiency (%)
A817342M1	1.8	880	9.59	0.704	5.94 (A)
A819444S1	1.85	932	9.44	0.670	5.89 (B)
A820314S1	~1.90	952	9.52	0.605	5.48 (C)

FIGURE 2.5.5-1. J-V CHARACTERISTICS OF THREE a-SiC SOLAR CELLS (SEE TEXT FOR DETAILS).

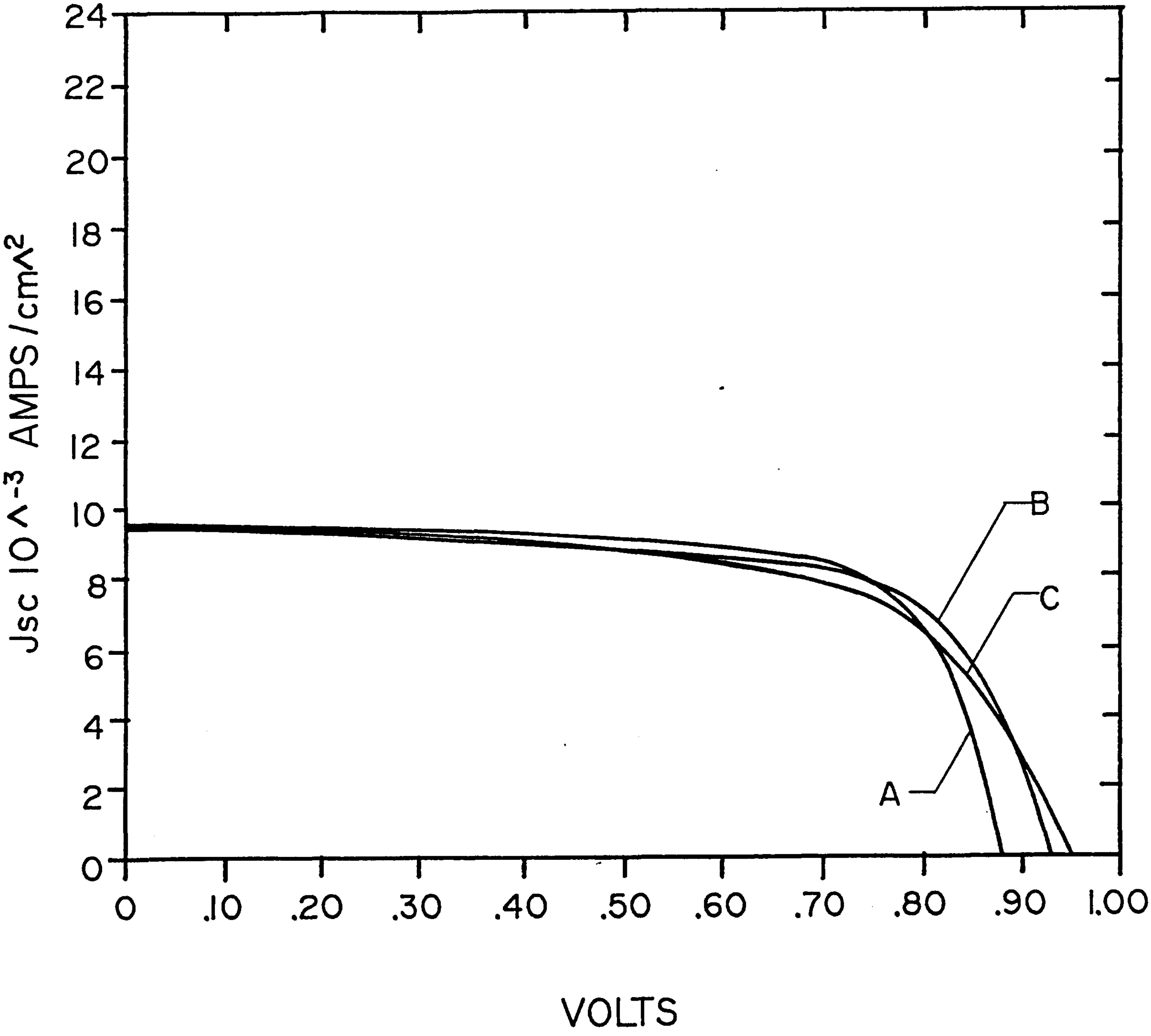

2.5.6 Multi-junction (stacked) Solar Cells

Multi-junction (stacked) solar cells in which the top cell has an i-layer of a-SiC:H and the bottom cell has an i-layer of either a-Si:H or a-SiGe:H have resulted in conversion efficiencies above 10%.

Figure 2.5.6-1 shows the J-V characteristics of an a-SiC:H/a-Si:H stacked junction cell which had a conversion efficiency of 10.2% with the following photovoltaic parameters: Voc = 1.752V, Jsc = 8.16mA/cm2, and fill-factor = 0.712. Figure 2.5.5-2 shows the quantum efficiency versus wavelength measurement of this device. Figure 2.5.6-3 shows the J-V characteristics of an all alloy stacked junction cell in which the top cell has an i-layer of a-SiC:H and the bottom cell has an i-layer of a-SiGe:H. This cell had a conversion efficiency of 10.5% with the following photovoltaic parameters : Voc = 1.722V, Jsc = 9.11mA/cm2, and fill-factor = 0.67. Figure 2.5.6-4 shows the quantum efficiency versus wavelength measurement of this device. The cell measurements were verified at SERI where a conversion efficiency of 10.3% was measured.

2.6 LIGHT-INDUCED EFFECTS

2.6.1 Indoor vs. Outdoor Measurements of Tandem Devices

In order to test the reliability of indoor light-soaking in predicting outdoor power losses, a number of modules from the same lot run were degraded. Eleven each were degraded indoors under sodium vapor lamps and outdoors at the Solarex outdoor test site in Newtown. The indoor degradation was carried out on a continuous basis under lamps at a temperature of about 45°C. These lamps were coated with a diffusing reflector to provide uniform illumination over a large area, and were calibrated using a suitably filtered single crystal cell which produces a known current when exposed to an AM1.5 spectrum. The outdoor degradation started in January, and has thus far proceeded through winter, spring and early summer. In order to compare our indoor and outdoor results we converted the outdoor exposure to an equivalent indoor exposure using the factor of 1000 hours/yr. The exact value of the conversion factor used is not important because of the logarithm nature of the time dependence. As can be seen from Figure 2.6.1-1, the outdoor performance is, within experimental error, that which would have been predicted from the indoor results.

FIGURE 2.5.6-1. J-V CHARACTERISTICS OF a-SiC:H/a-Si:H STACKED CELL WITH AN EFFICIENCY OF 10.2%.

a-SiC/a-Si

Cell No. L7127-IFS2ITO	Date 052687
Voc = 1.752 Volts	Jsc = 8.16 mA/cm^2
F.F. = .712	Eff = 10.17%
Power = 10.17 mW/cm^2	Illum. = 99.24 mW/cm^2
V max = -1.450 Volts	J max = 7.01 mA/cm^2
Rs = 2.27E + 01 ohm/cm^2	Rsh = 2.85E + 03 ohm-cm^2
Temp = 27.1 deg C	Cell Area = .257 cm^2

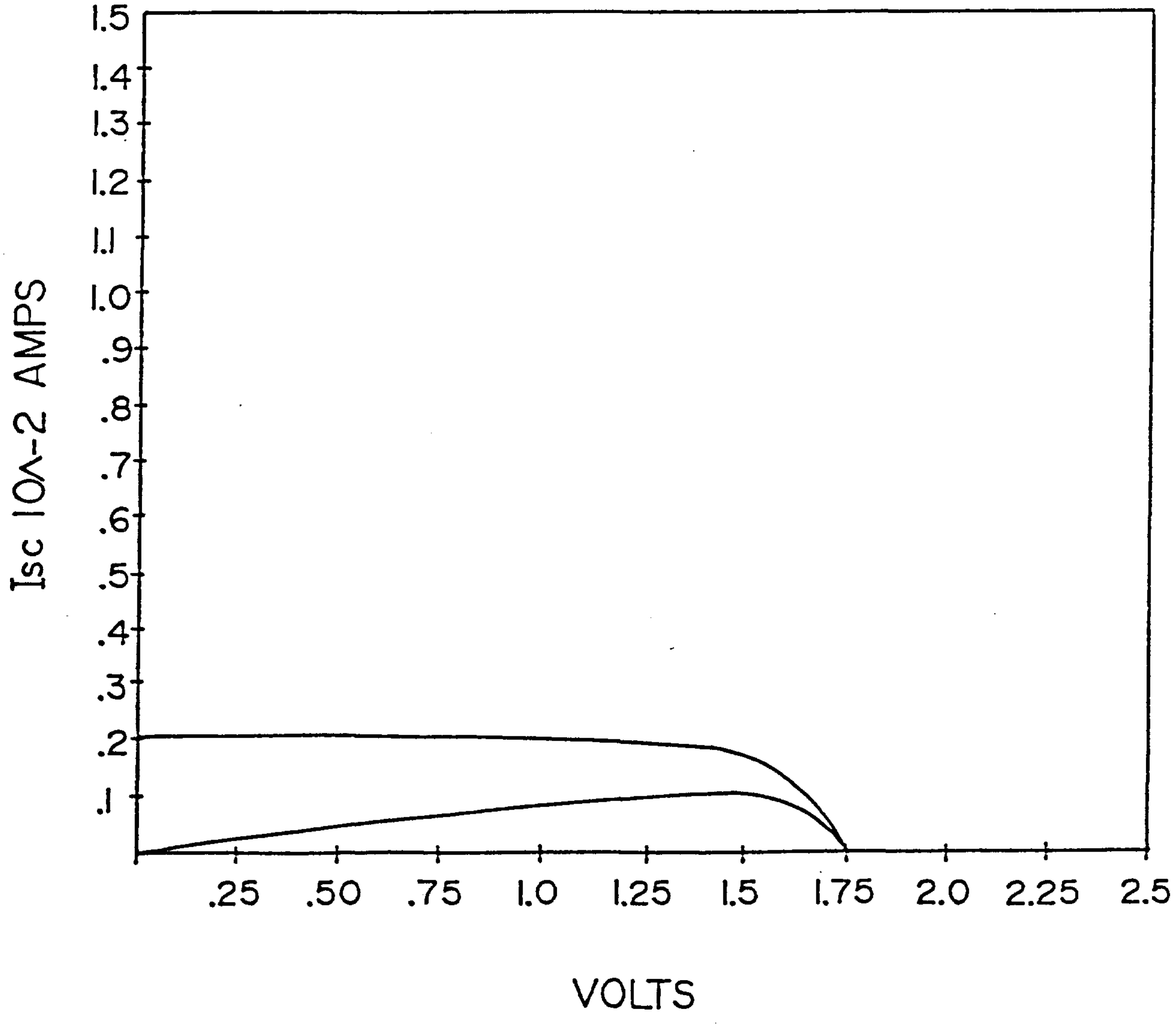

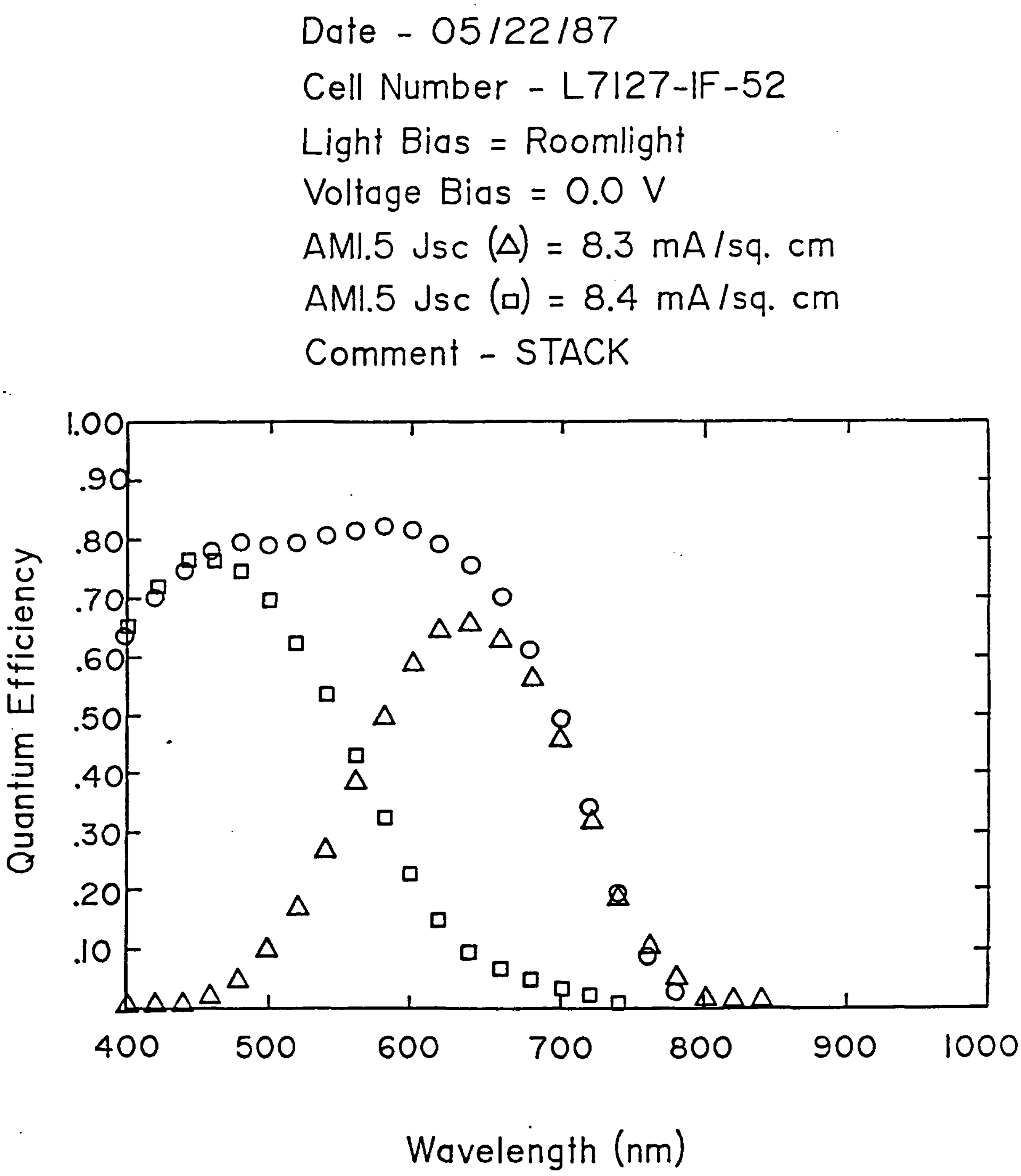

FIGURE 2.5.6-2. QUANTUM EFFICIENCY OF DEVICE IN FIGURE 2.5.6-1.

FIGURE 2.5.6-3. J-V CHARACTERISTICS OF a-Si/a-SiGe STACKED CELLS WITH A 10.5% CONVERSION EFFICIENCY.

Cell No. LL7217-3-3 TIAR
Date 870810
Voc = -1.722 Volts
Jsc = 9.11 mA/cm^2
F.F. = .670
Eff = 10.51%
Power = 10.51 mW/cm^2
Illum. = 101.01 mW/cm^2
V max = -1.354 Volts
J max = 7.76 mA/cm^2
Rs = 2.26E+01 ohm/cm^2
Rsh = 6.67E+03 ohm/cm^2
Temp = 24.1 deg. C
Cell Area = .755 cm^2

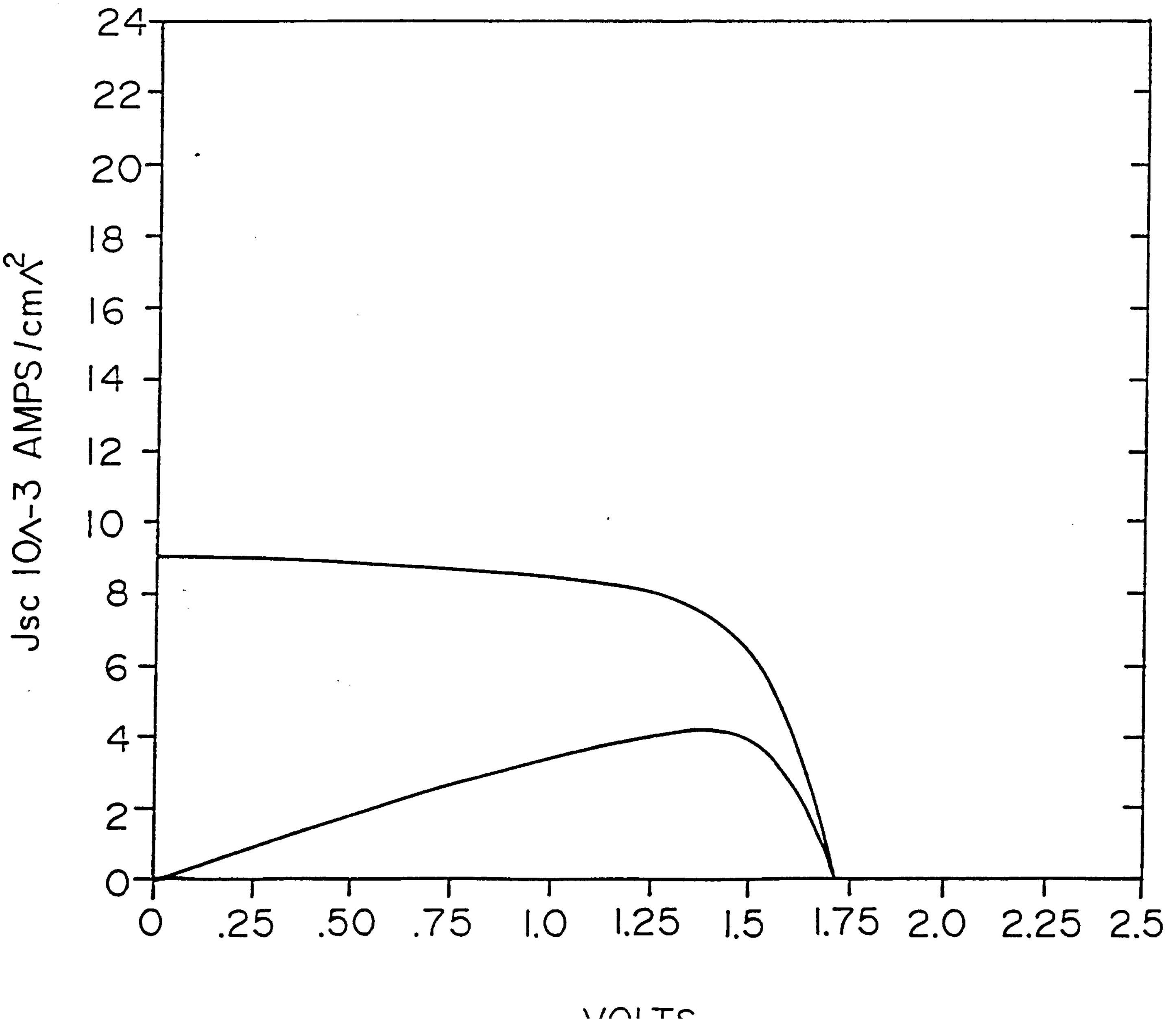

FIGURE 2.5.6-4. QUANTUM EFFICIENCY OF DEVICE FROM FIGURE 2.5.6-3.

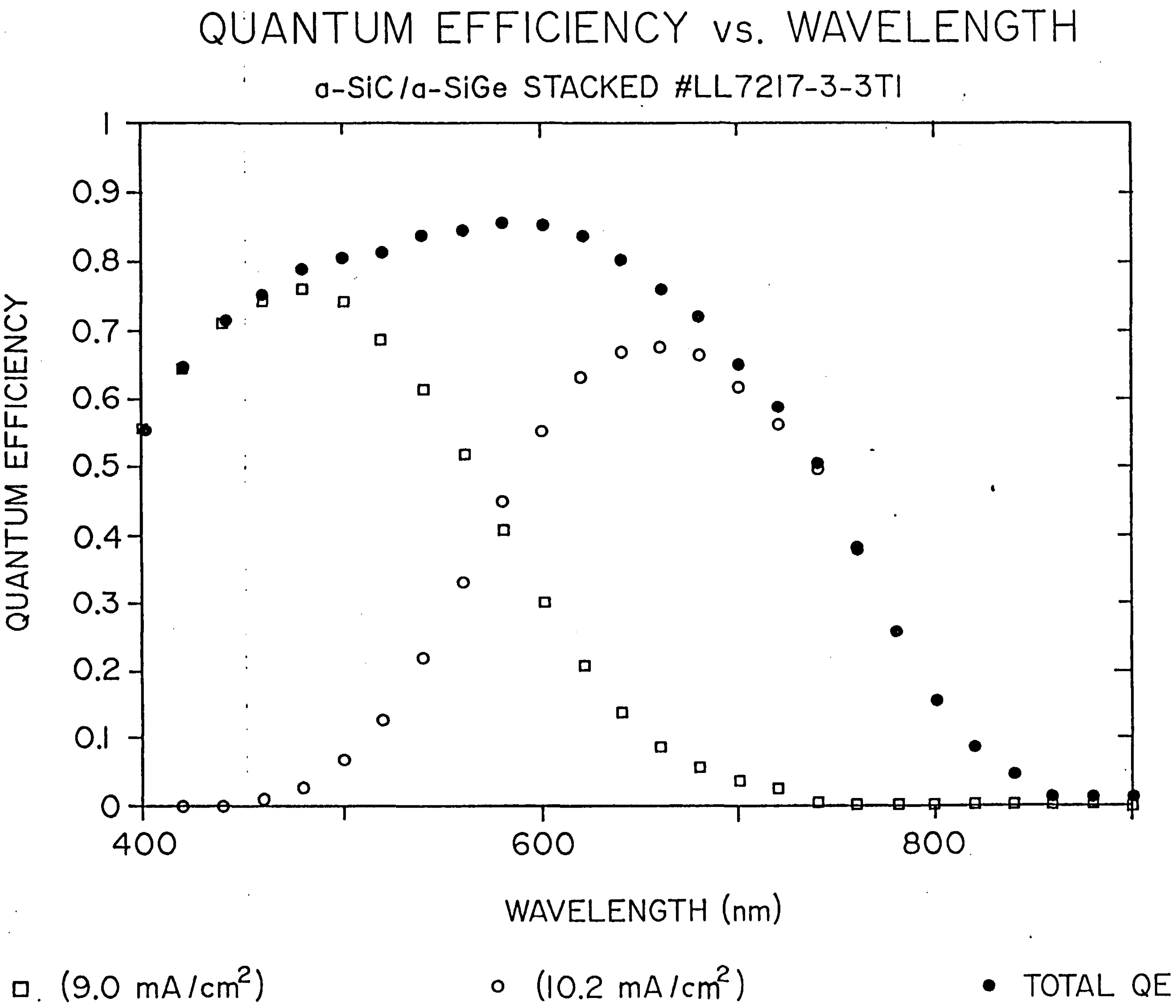

FIGURE 2.6-1-1. EFFICIENCY OF THIN Si/Si TANDEM CELLS AS A FUNCTION OF LIGHT-SOAKING TIME.

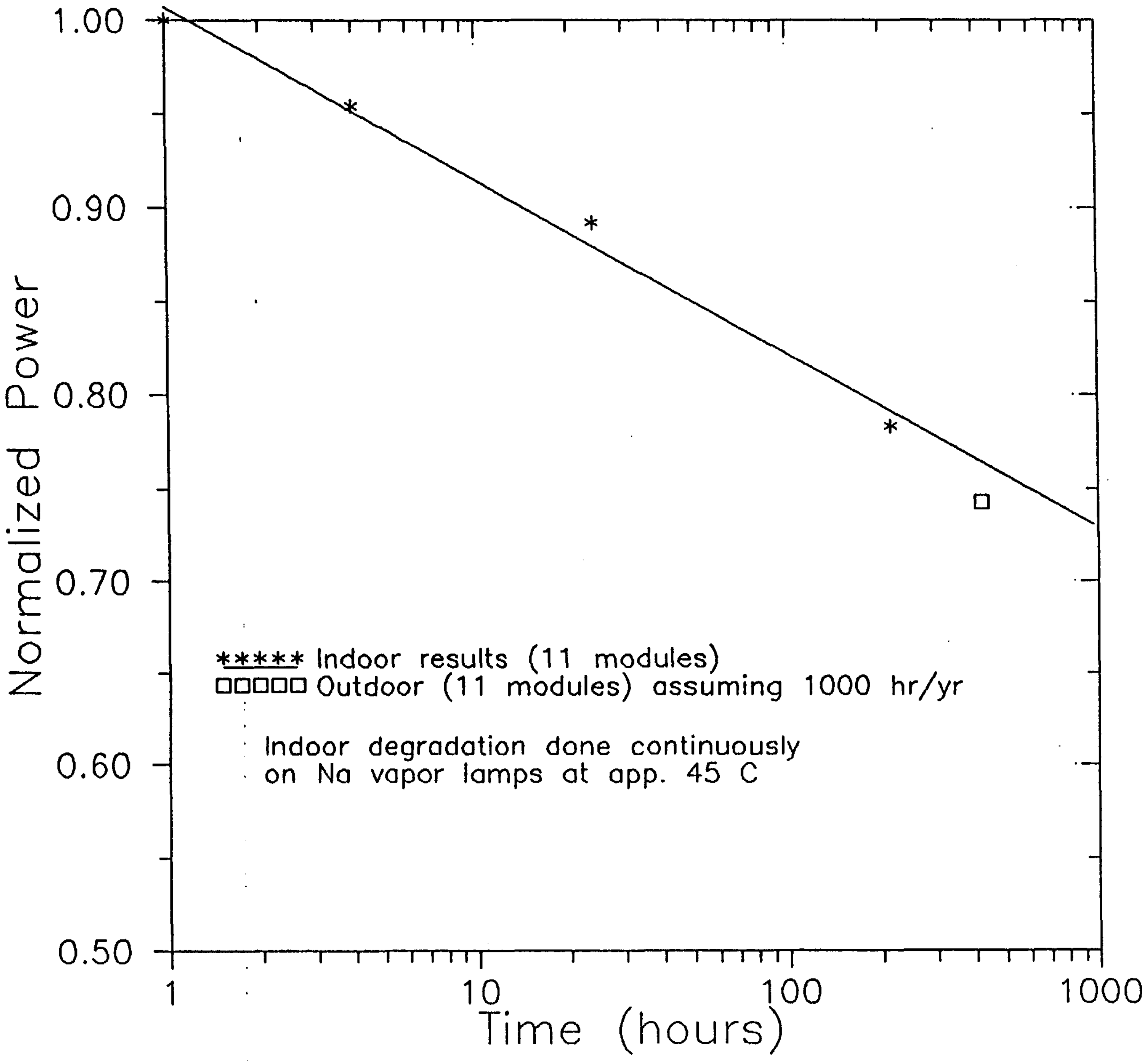

2.6.2 Stability of Stacked Junction Solar Cells

One of the attractions of multi-junction cells is that they may offer improved stability without sacrificing performance since multi-layer, thin junction cells may be stacked, thus preserving the stability inherent in that design. Such devices have been built and tested and results show the best long term stability and high initial performance to date. For example, a number of thin Si/Si tandem cells (600Å/2000Å) have been made with average initial efficiencies of 8.96%. After 1150 hours continuous light soaking at open circuit voltage on a Na vapor lamp ($100mW/cm^2$), the efficiency was 7.7% (Figure 2.6.2-1).

An attempt has been made to understand the kinetics of the photodegradation of stacked cells in terms of the kinetics of the degradation of the component junctions. It appears that the stacked cells do behave as would be expected if they were simply considered to be single junction cells connected in series. This somewhat simplifies the analysis since the kinetics of single junctions devices are well known.

To briefly summarize the results, the photodegradation of the multi-junction devices is composed of two components. There is a short period of stability, the length of which is related to the number of junctions and their thicknesses. This period results from the shading of the bottom junction(s) by the top junction(s). Following this, the efficiency falls linearly with the log of time. The slope of this part of the curve is found to be approximately the mean of the slopes which would have been obtained for the components of the stack if they had been degrades as single junctions.

The later stages of degradation have been simulated experimentally using single junction devices connected in series (wired) and suitably filtered to simulate the stacked device. Figure 2.6.2-2 shows the set-up schematically and Figure 2.6.2-3 shows the changes in efficiency for the single junction components individually, wired in series and filtered, and for the stacked junction. The stacked junction and wired components degrade at very similar rates and this rate is roughly midway between that of the components. We have also investigated this effect by generating the I-V characteristics of the components, then adding them together in the appropriate way to generate the current-voltage curve for the series connected pair Again the overall characteristic is between that of the components.

The delay in the onset of degradation is a consequence of degrading the rear cell at a lower light intensity. Figure 2.6.2-4 shows the effect of shading a single

FIGURE 2.6.2-1. EFFICIENCY VS. TIME OF 7.7% Si/Si STACKED CELL.

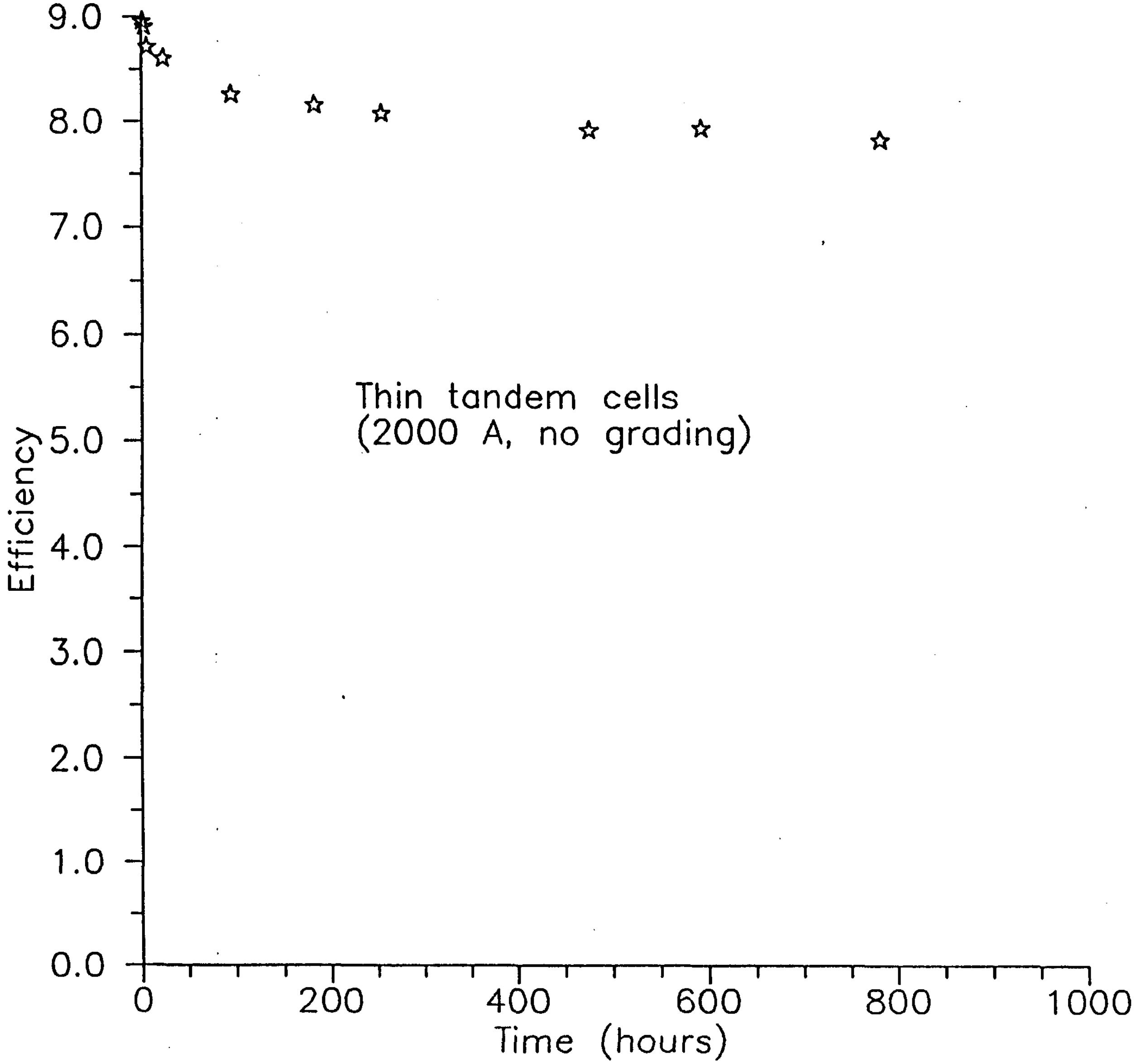

FIGURE 2.6.2-2. SCHEMATIC OF EXPERIMENT DESIGNED TO COMPARE DEGRADATION OF A TANDEM TO THAT OF ITS COMPONENT CELLS.

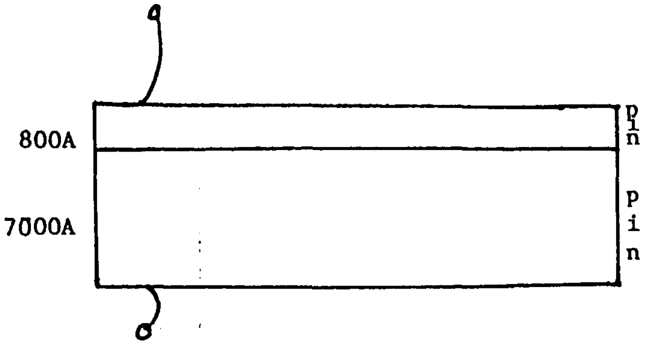

i) Monolithic Tandem Device

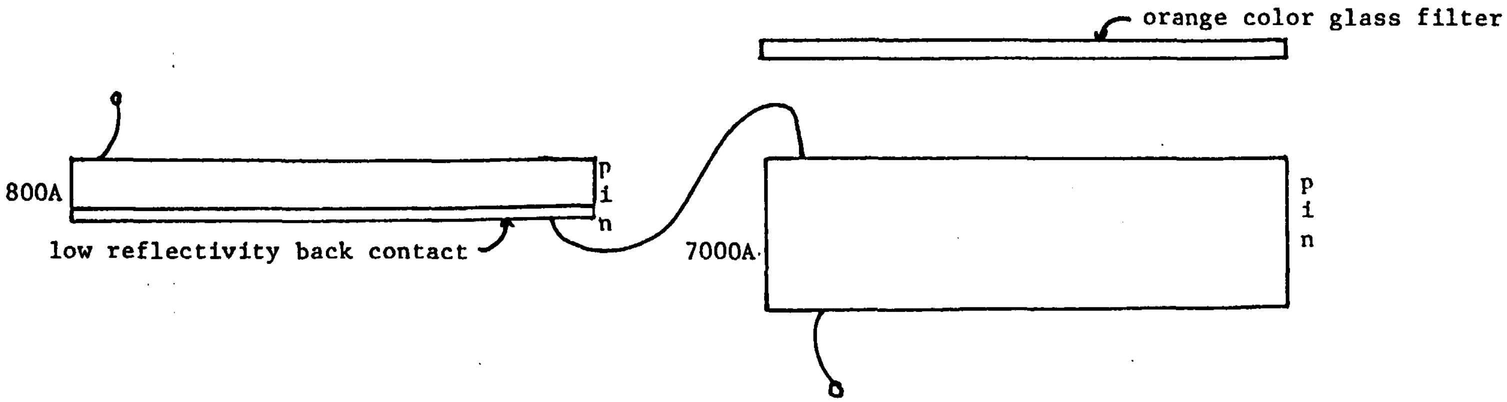

ii) Components of device i) suitably filtered and wired in series.

FIGURE 2.6.2-3. NORMALIZED EFFICIENCY VS. TIME OF A Si/Si TANDEM DEVICE, ITS SINGLE JUNCTION COMPONENTS, AND THE SINGLE JUNCTION COMPONENTS WIRED IN SERIES. THE SINGLE JUNCTION COMPONENTS ARE FILTERED TO PROVIDE THE SAME CURRENTS AND SPECTRAL RESPONSES AS THE COMPONENTS OF THE TANDEM.

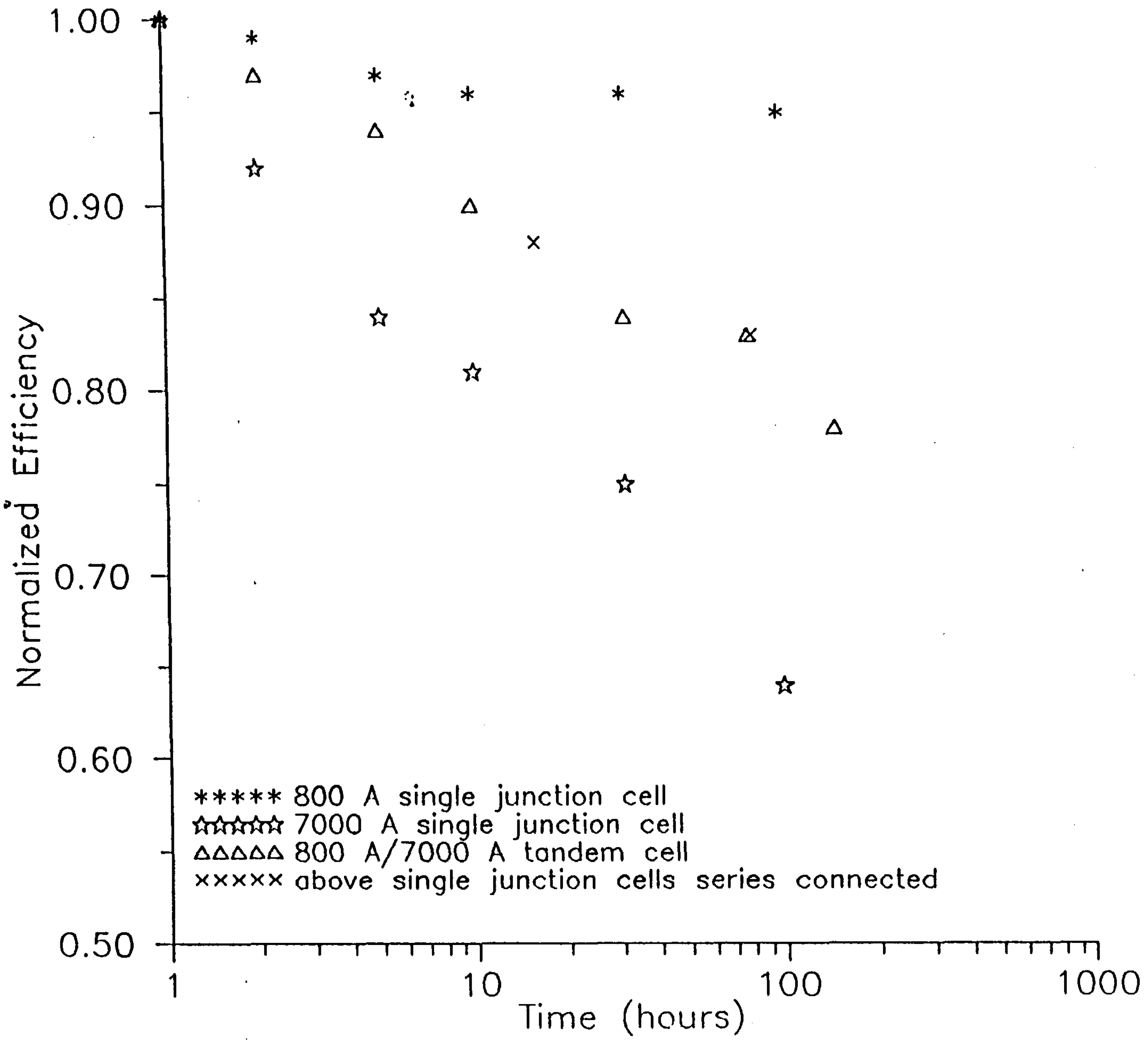

[redacted]

FIGURE 2.6.2-4. NORMALIZED EFFICIENCY VS. TIME FOR IDENTICAL CELLS LIGHT-SOAKED UNDER VARIOUS INTENSITIES.

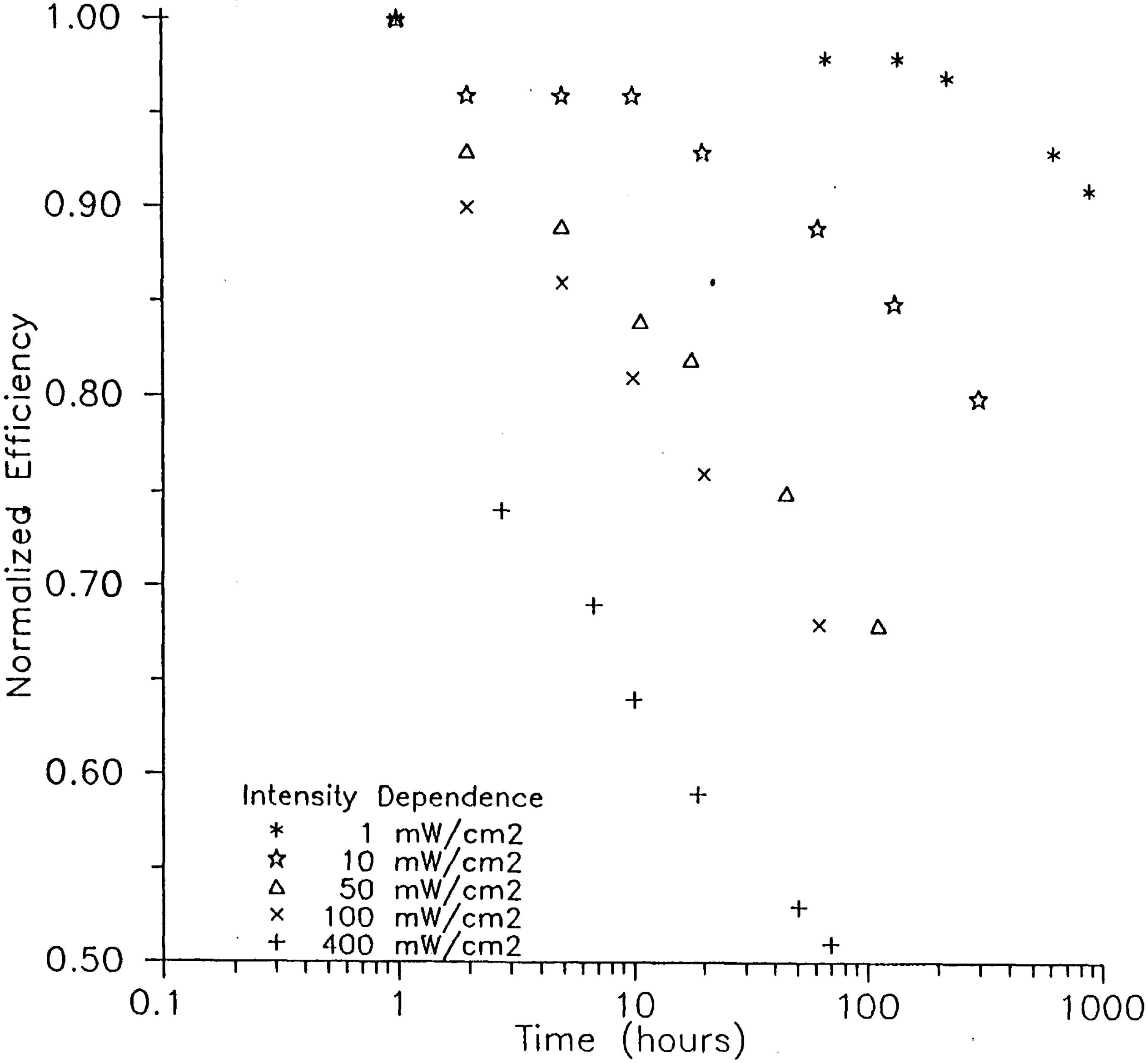

junction cell. There is a delay in the onset of degradation, however the sloe of the straight line obtained by plotting efficiency vs. log time is the same regardless of intensity. Therefore, reciprocity is not quite obtained; i.e., degradation proceeds somewhat slower than expected at lower intensity than expected on the basis of dose.

2.6.3 Quantum Efficiency Measurements of Stacked Cells

We have been investigating the problems associated with measurement of the spectral response of the components of stacked cells. We have again approached the problem by simulating the stacked cell by connecting single junction cells in series and suitably filtering the devices. We have been concerned only with the measurement of spectral response at 0V bias for each of the components of the device and have not addressed the considerably more difficult problem of measurement at arbitrary voltage biases. We have made the measurements under usual conditions, i.e., under blue light bias to measure the back cell and under red light bias to measure the front cell, in both cases holding the cell at 1/2 V_{OC}.

Two principle problems have been discovered. First, when biasing the cell to 1/2 V_{OC}, one must be sure to use the open circuit voltage which is obtained under the applied light bias conditions and not that measured under AM1.5. Under conditions of blue or red light bias the V_{OC} is somewhat lower than that obtained under AM1.5. Second, we found that our solar simulator performed poorly when measuring very thin cells such as are used for the top junction of a stack device. A more sophisticated approach, such as a multi-source simulator, is probably required.

2.6.4 Stability of a-Si:H

One of the major impediments to more stable and efficient amorphous silicon based solar cells is the problem of the light induced effects in these materials.

The fundamental physics of the Staebler-Wronski effect was investigated using current injection degradation of solar cells at temperatures great enough for complete saturation. The defect related to the Staebler-Wronski Effect appears to be governed by a simple equilibrium between charge carriers and defect centers when the high temperature saturation is considered. The estimated density of weak bonds (those susceptible to the creation of dangling bonds by light exposure) determined by these studies is $\sim 10^{19}\mathrm{cm}^{-3}$. This work is summarized in Appendix II.

3.0 NON-SEMICONDUCTOR MATERIALS RESEARCH

3.1 ABSORPTION ENHANCEMENT IN a-Si:H SOLAR CELLS

3.1.1 Introduction

Enhancement of absorption of long wavelength radiation (>600 nm) is of continued interest due to the large current gains which may be realized. To direct efforts to maximize absorption enhancement in a-Si:H solar cells, the light losses occurring in the structure are determined. The results of modeling the a-Si:H single junction solar cell structure are summarized below.

3.1.2 Optical Modeling

In the a-Si:H solar cells, the enhancement of absorption in the i layer is limited by absorption of radiation in the inactive layers of the structure. Deckman, et al. [1] considered the effect of these parasitic absorptions on the absorption occurring in the I layer, viz.,

$$(1-e^{-\alpha_I l_I}) + \frac{e^{-\alpha_I \ell_I}(1- e^{-2\alpha_I \ell_I})(1-n_r)[1+ e^{-2\alpha_I \ell_I}(1-n_f)(1-(1/n_I)^2]}{1-e^{-4\alpha_I \ell_I}(1-n_f)(1-n_r)(1-(1/n_I)^2}$$

where:

n_f = parasitic absorption of front contact

n_r = parastic absorption of the rear contact

n_I = index of refraction of I layer

α_I = absorption coefficient of I layer

ℓ_I = thickness of I layer

The above expression differs from that of Deckman, et al., in that, here, first pass absorption is treated separately from subsequent passes and the front and rear contact absorptions are treated individually. In developing this expression it was assumed that radiation reflected off the rear contact is scattered in Lambertian distribution.

If the fraction of the radiation incident upon the solar cell which enters the I layer and the parasitic absorptions are known, the above expression may be used to predict the I layer absorption. To obtain estimates of these quantities, a Lambertian angle averaged ray was followed through the various layers of the structure. The solar cell structure considered was: glass/textured tin oxide/a-Si:H p-i-n/rear contact. The rear contact was a metal or ITO (indium tin oxide)/metal. Figures 3.1.2-1 to 4 summarize the expected optical transmission or absorption for the various layers in the device structure. Figure 3.1.2-1 illustrates the transmission of light into the i-layer in the model presented above. Figure 3.1.2-2 plots the absorption loss expected for the p-layer. The parasitic absorption due to the rear contact is plotted in Figure 3.1.2-3 for molybdenum and aluminum contacts. Note that aluminum is far superior to molybdenum. Figures 3.1.2-4 and 5 illustrate the parasitic absorption for ITO/Mo and ITO/Ag rear contacts. Both the specular and trapped case are illustrated. Either metal contact in combination with ITO is far superior to the metal contact above, and as expected the ITO/Ag combination has extremely low absorption, which coupled with high reflectivity makes this contact an outstanding choice.

Figures 3.1.2-6 thru 9 illustrate the expected long wavelength QE, for Mo, Al, ITO/Mo and ITO/Ag. Good agreement with experiment is seen in all but the ITO/Ag contact. This discrepancy is likely due to the particular sample used in this experiment. Generally higher QE's at long wavelength are observed.

In summary, the long wavelength response of a-Si:H solar cells is limited by the parasitic absorptions which are present in the structure. The absorption in the rear contact is, in most cases, the major loss mechanism.

3.2 PROCESSES AND MATERIALS FOR SUBMODULE FINISHING

Investigation of materials and processing techniques for module finishing operations which are cost effective and adaptable to continuous in line manufacturing are ongoing. Process steps which are being examined include edge isolation, electrical connection and encapsulation for environmental protection. Simultaneous study of these factors has been undertaken because of their mutual interaction in manufacturing operations and in the capabilities of the finished product.

A high degree of electrical isolation is necessary for the safety and durability of high voltage array systems. Methods studied to achieve 1550 volts minimum wet isolation to the CTO coated edge include chemical etching, laser cutting and abrasive media blasting. Both laser cutting and abrasive media blasting in combination with a variety of coating materials including epoxy, urethane and asphaltic material

FIGURE 3.1.2-1. LIGHT TRANSMITTED INTO THE I-LAYER AS A FUNCTION OF WAVELENGTH FOR THE MODE DISCUSSED IN THE TEXT.

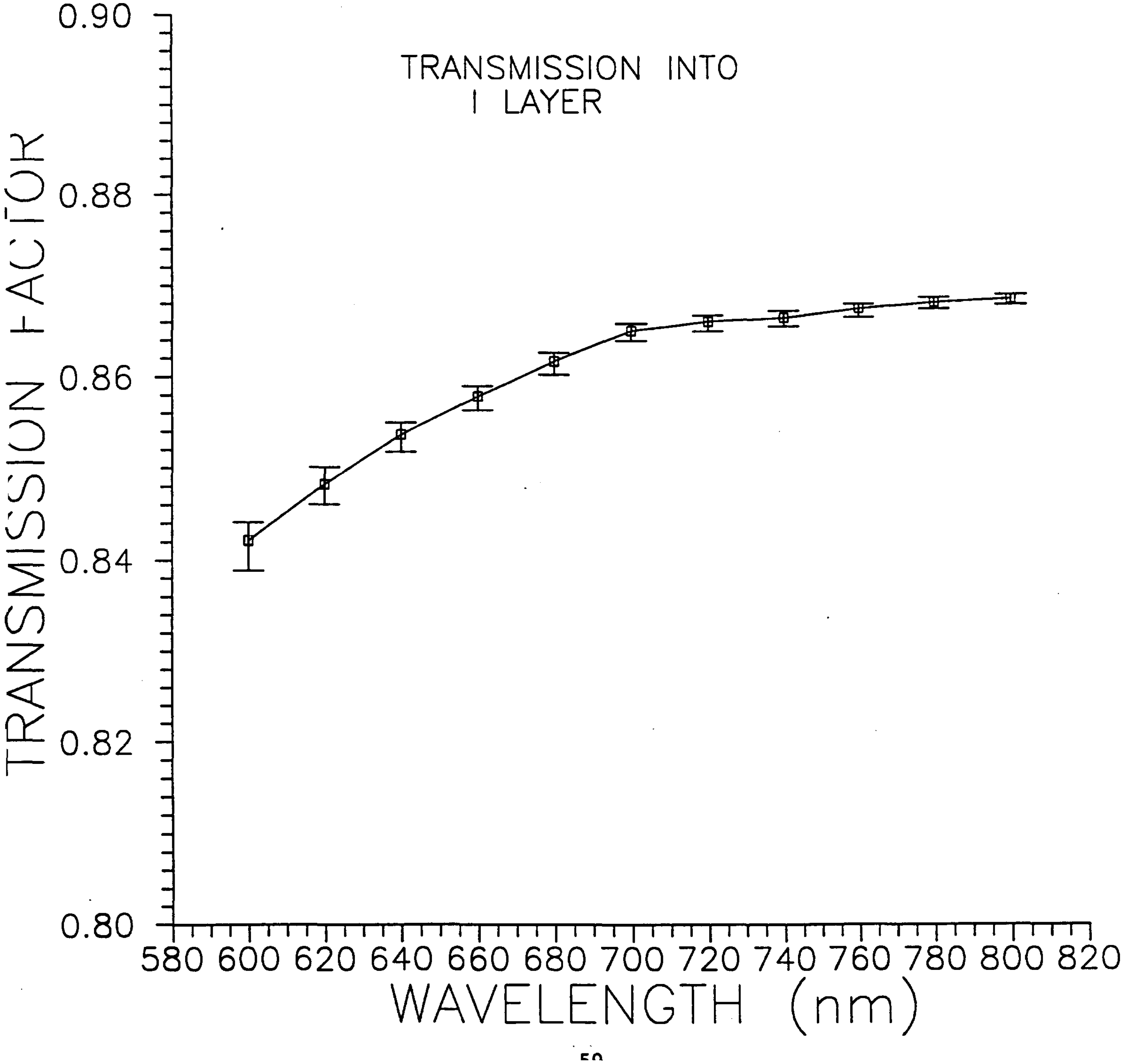

FIGURE 3.1.2-2. ABSORPTION LOSS EXPECTED FOR THE P-LAYER.

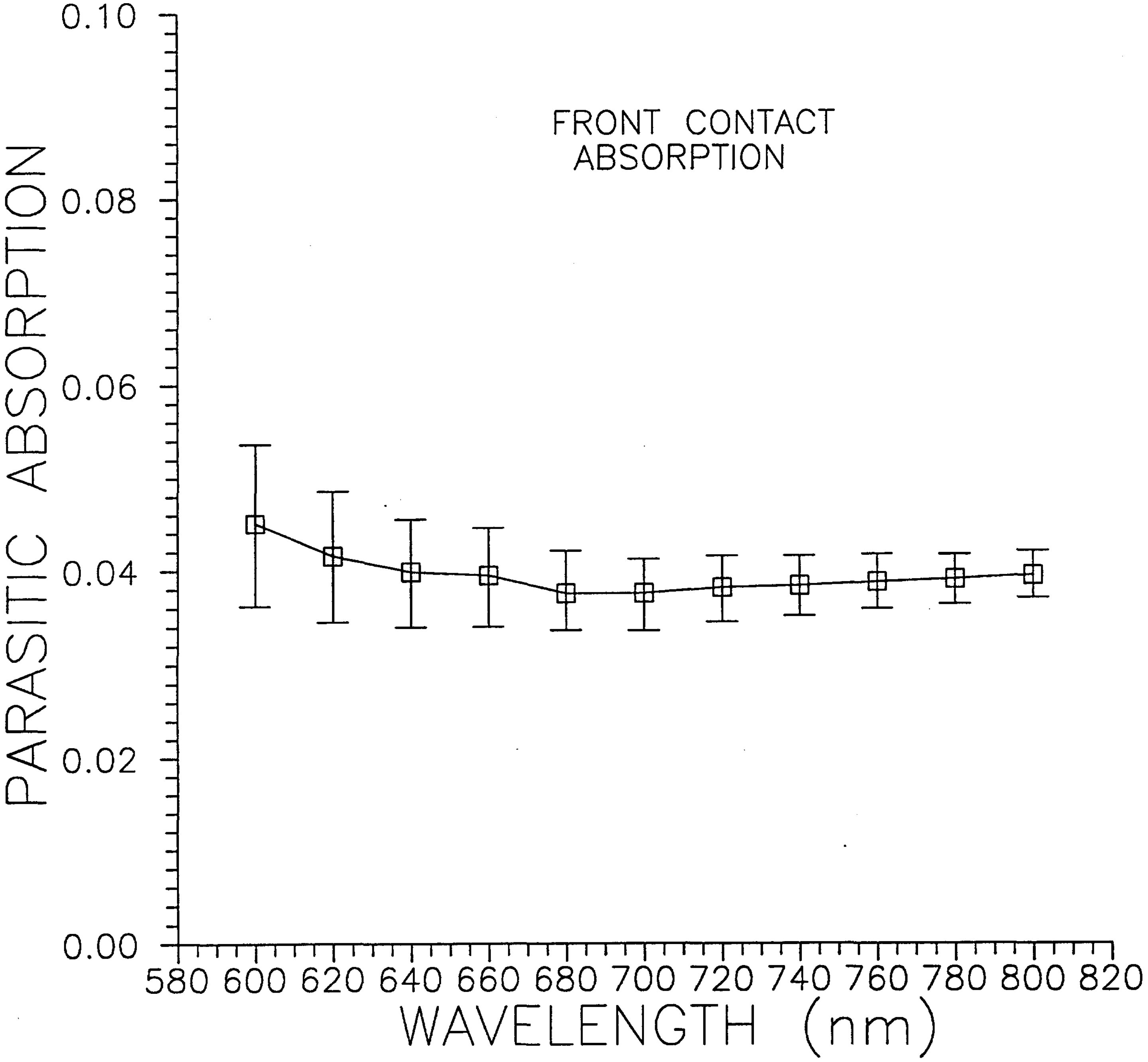

FIGURE 3.1.2-3. PARASITIC ABSORPTION DUE TO Al AND Mo REAR CONTACTS

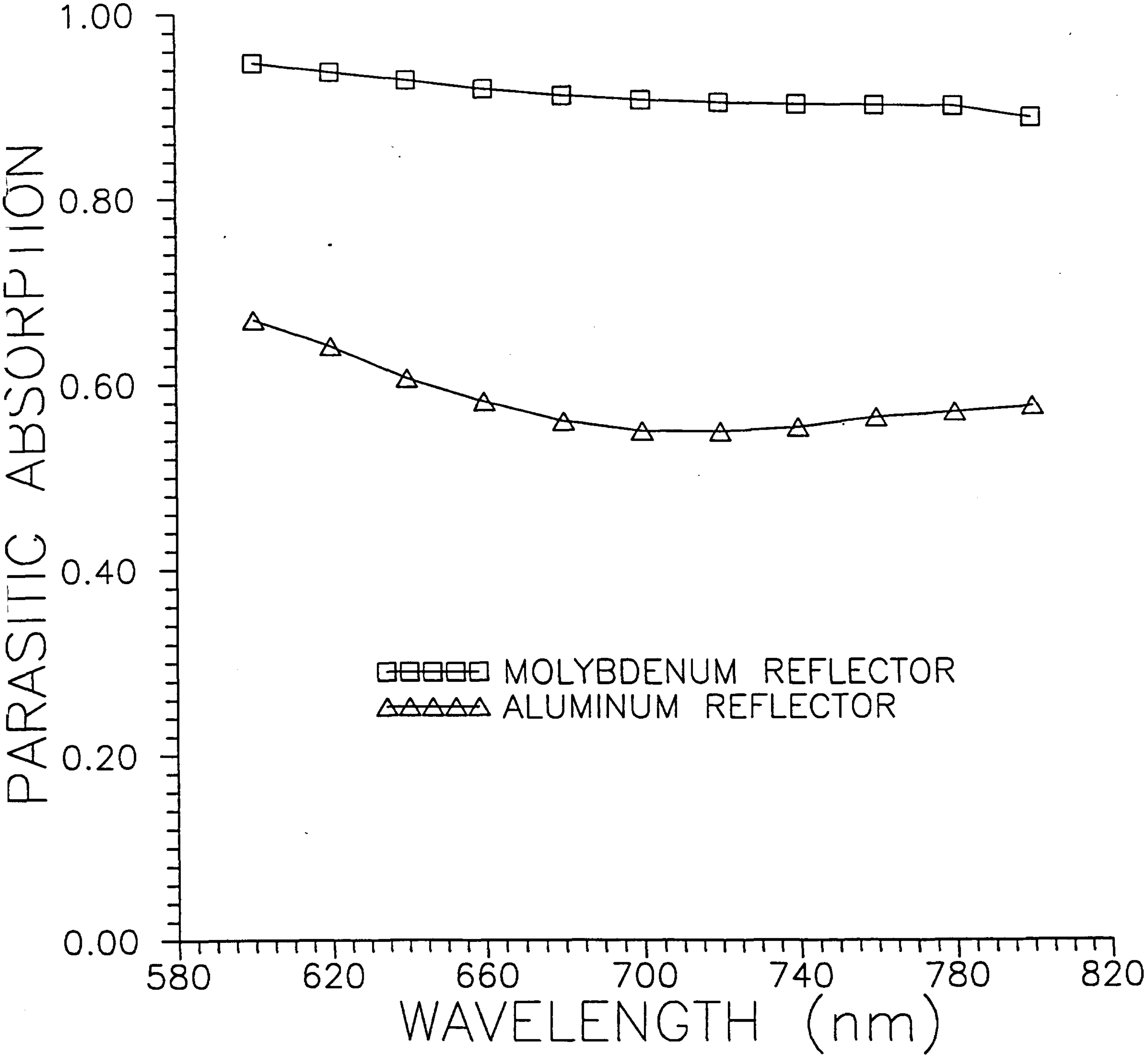

FIGURE 3.1.2-3. PARASITIC ABSORPTION FOR ITO/Mo REAR CONTACTS.

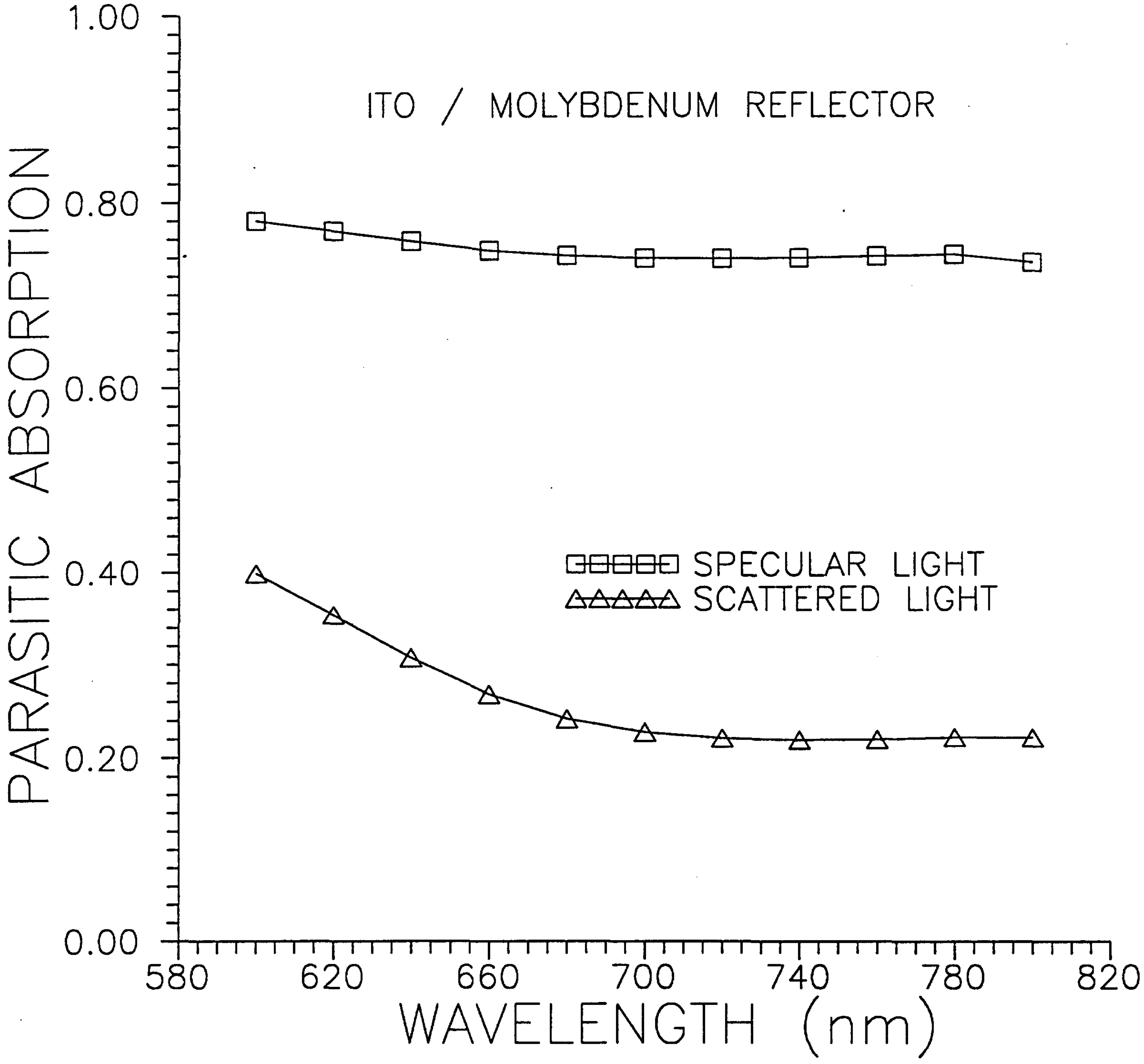

FIGURE 3.1.2-5. PARASITIC ABSORPTION FOR ITO/Ag REAR CONTACTS.

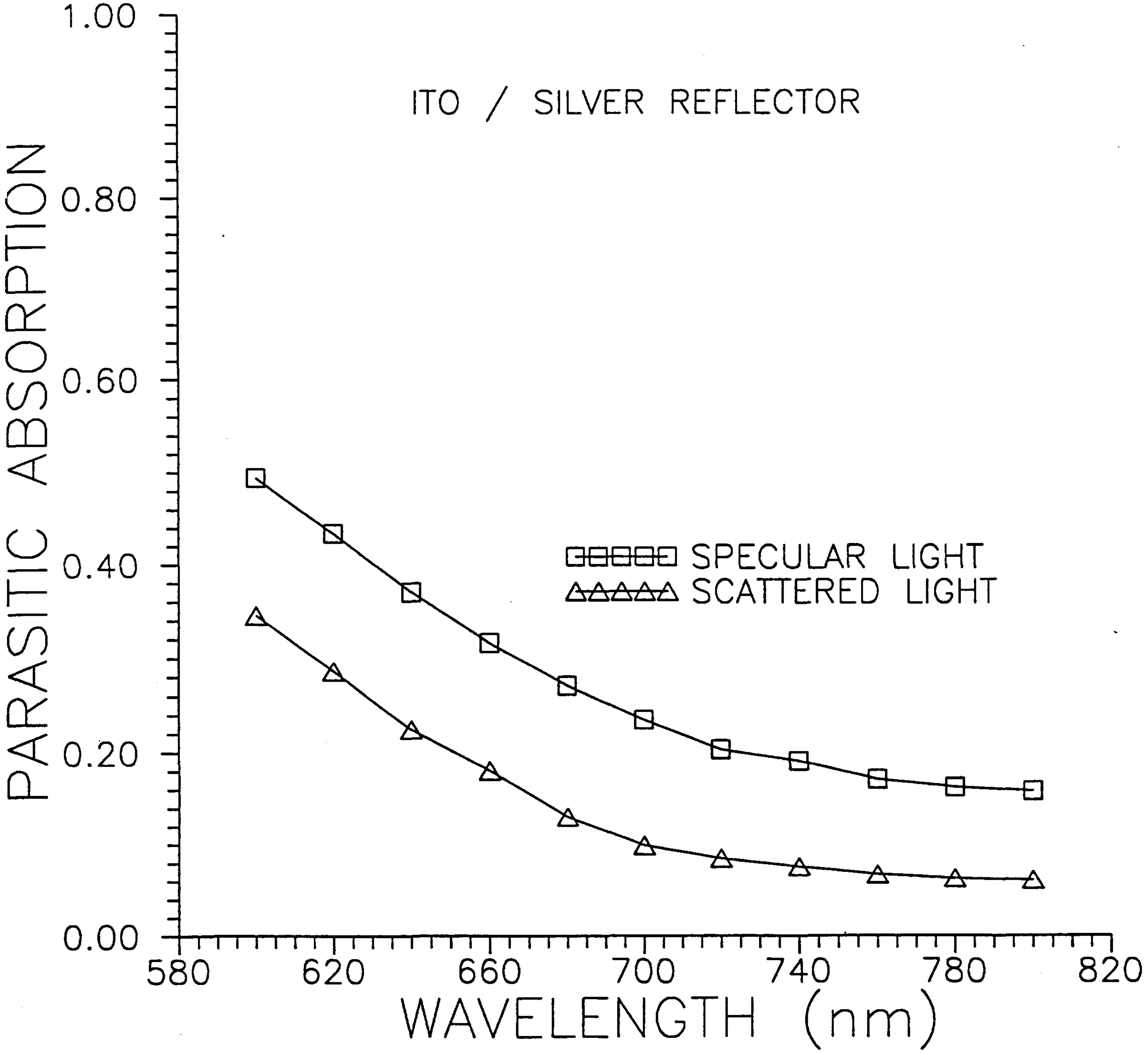

FIGURE 3.1.2-6. COMPARISON OF THE CALCULATED AND MEASURED LONG WAVELENGTH QE FOR Mo CONTACT.

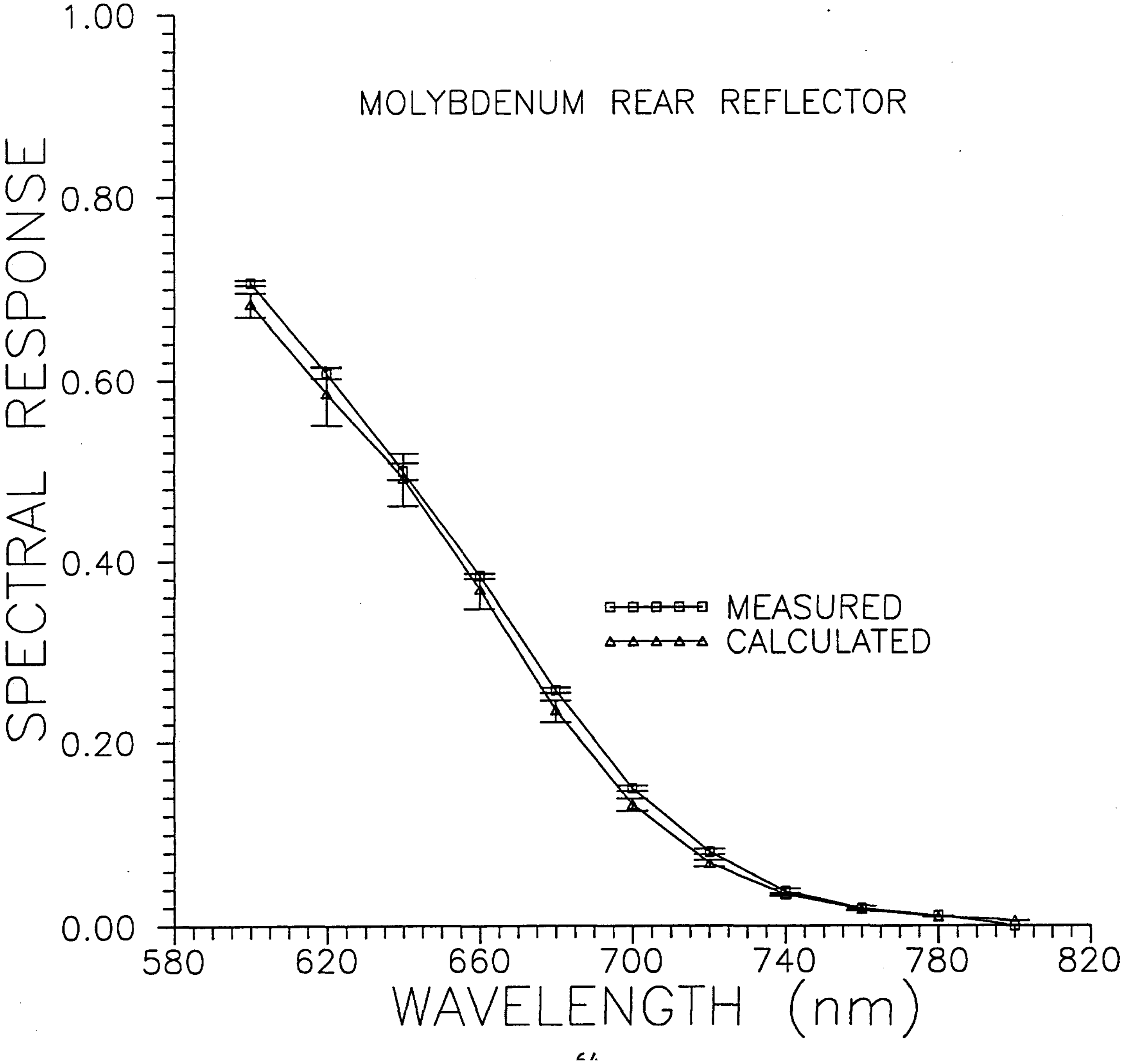

FIGURE 3.1.2-7. COMPARISON OF THE CALCULATED AND MEASURED LONG WAVELENGTH QE FOR Al CONTACT.

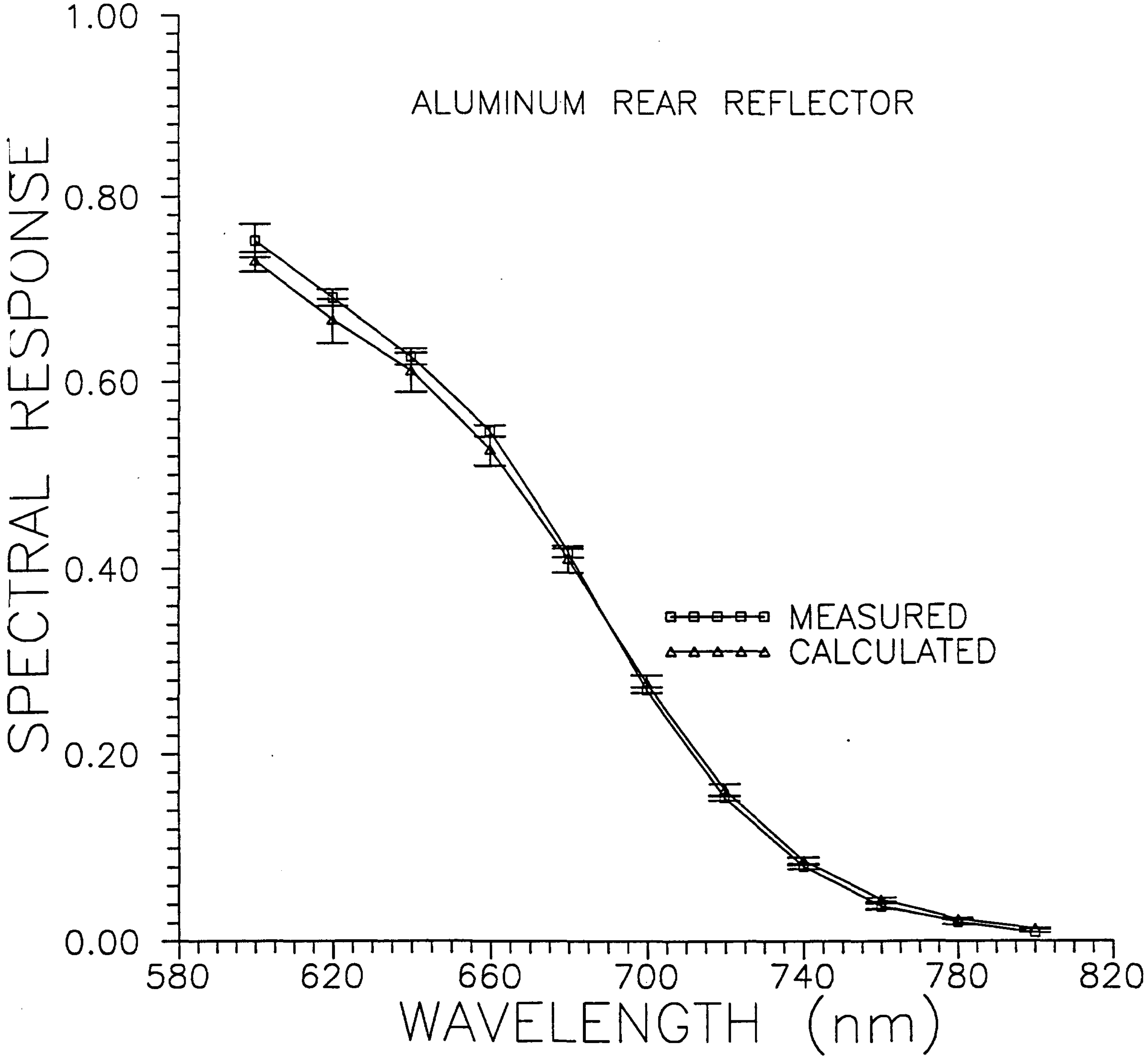

FIGURE 3.1.2-8. COMPARISON OF THE CALCULATED AND MEASURED LONG WAVELENGTH QE FOR ITO/Mo CONTACT.

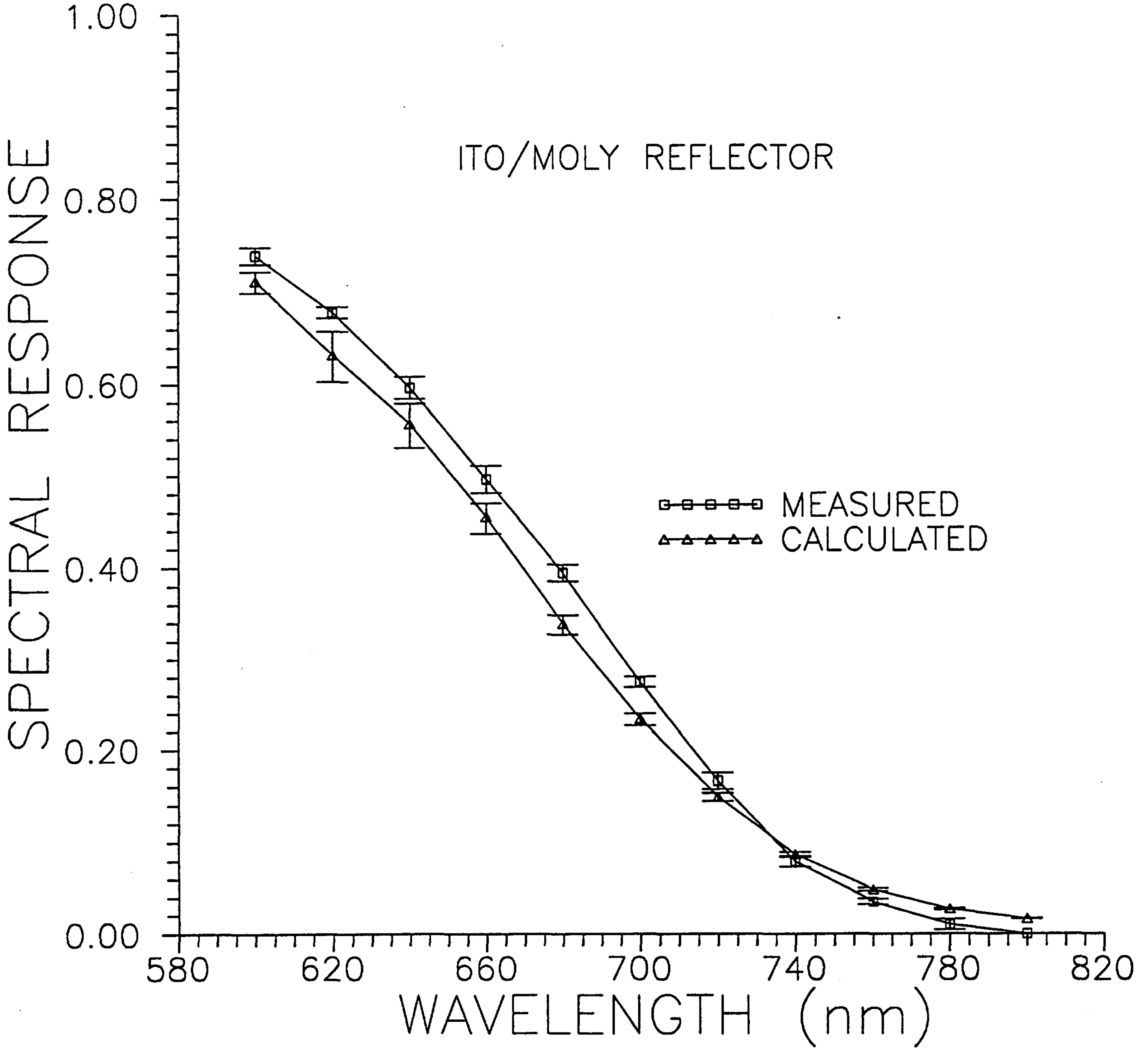

FIGURE 3.1.2-9. COMPARISON OF THE CALCULATED AND MEASURED LONG WAVELENGTH QE FOR ITO/Ag CONTACT.

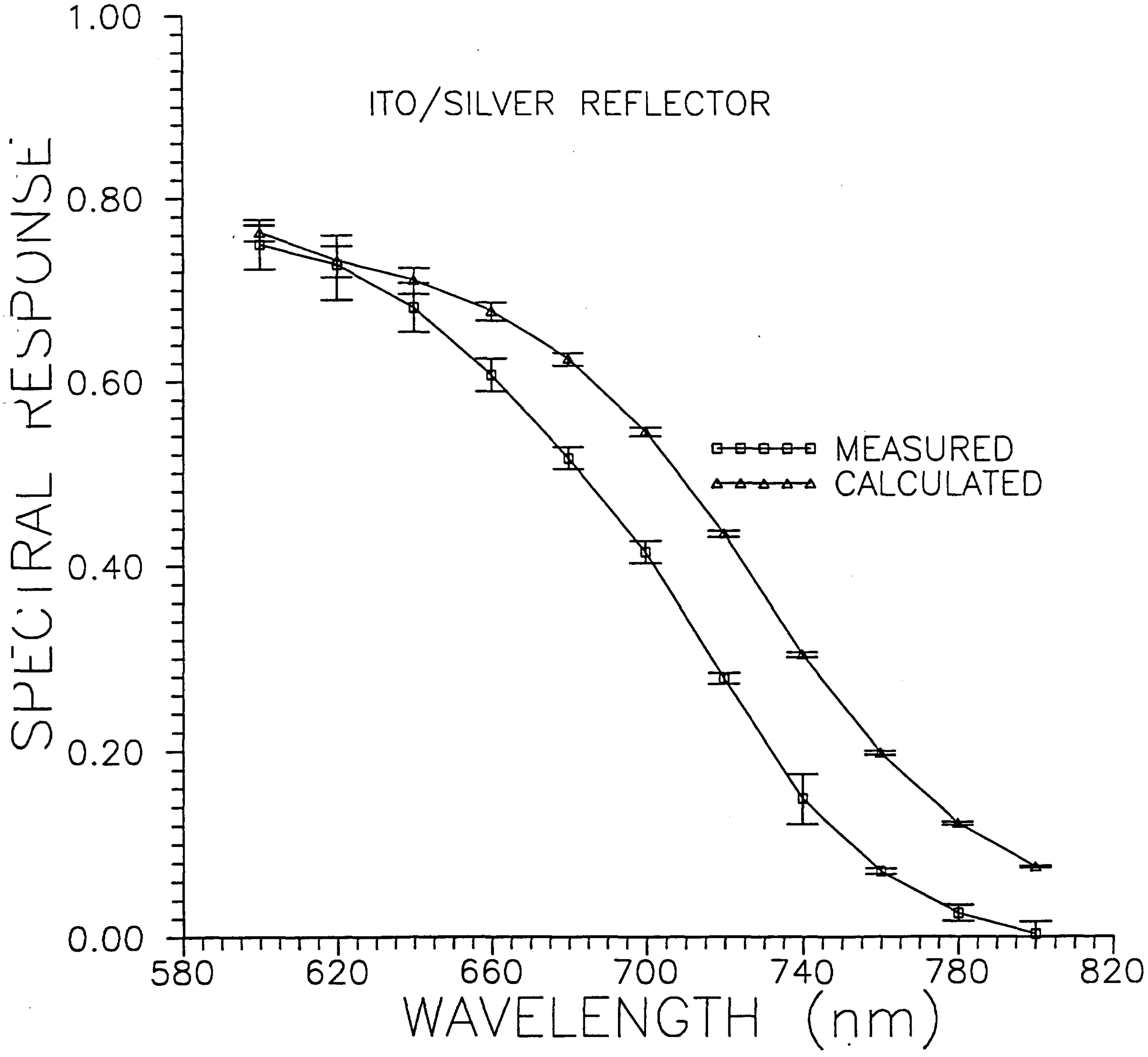

consistently achieved isolation breakdown voltage greater than 1550 volts dc. Optimization of the isolation methods and coatings are continuing.

Improvements are also being sought in the methods of electrical interface with basic PV module. Direct resistance welding to the aluminum backing metal, ultrasonic welding of nickel clad aluminum ribbon and printing of silver filled thick film and polymeric base conductors have been examined. Epoxy, polyester and polyimide base conductors have shown initial promise along with printed thick film silver. Each has survived 50 cycles of thermal cycle and 10 cycles of humidity freeze tests. More extensive environmental testing is in progress.

Resistance welds directly to the aluminum back metal have not been successful. The thin metal appears to prove insufficient thickness to survive this process. The feasibility of laser welding of aluminum metal to the back metal of the plate has been demonstrated. Apparently the control available in laser processing can overcome the difficulties of working with the thin backing metals. Ultrasonic welding of nickel clad aluminum ribbon to a previously welded aluminum ribbon was demonstrated. This provides means of replacing the large solder pad for wire connection with an equally solderable but more convenient wire connection point.

A variety of coating materials which can be applied to PV modules in a production oriented spray type process are being evaluated. Varnish, epoxy, urethane and their derivatives, epoxy urethane and acrylic urethane along with acrylic and asphaltic materials have been applied to modules. Epoxies and urethanes both appear promising as protective materials.

In addition these coatings have good dielectric properties and low moisture absorption which is essential to achieving electrical isolation to 1550 volts wet on both the edge and back of PV modules. Optimization of application techniques is required to achieve good adhesion, defect free and electrically insulating coatings in manufacturing operations.

4.0 SUBMODULE RESEARCH

4.1 HIGH EFFICIENCY MODULES WITH ITO/Ag/Al

The fabrication of high efficiency small area amorphous silicon solar cells often utilizes silver as a highly reflecting back metal contact. Other materials such as titanium, ITO, or ZnO often are deposited prior to silver. These materials serve as diffusion barriers to silver migration during heat treatments or they provide an enhanced red response in the quantum efficiency of the solar cells. Masks are used during the deposition of the back contact to the define the active area of the solar cells.

When silver or the combination of silver with other materials are used to fabricate large area modules special problems must be addressed. The primary problem is silver diffusion which electrically shorts the solar cell diodes when the metal is scribed with a laser or when the diodes are electrically cured. This problem is severe when Ti/Ag is used as a back metal contact. When ITO/Ag is used this difficulty is minimized. Unfortunately, the laser scribing of ITO/Ag films can result in silver peeling and subsequent poor performance of solar cell modules.

One approach to solving the above problems is to deposit ITO/Ag over most of the area of module diodes using a mask that covers the laser scribing interconnect portions of the solar cell module. This metallization is then followed by an aluminum deposition over the entire module after the mask is removed. The result is a module that has ITO/Ag covering most of the area of the module diodes but has aluminum in the region of the laser scribed interconnects. In this way, a module retains the well established metal scribing of aluminum but has an enhance red response (and corresponding J_{sc}) from ITO/Ag. A cross sectional view of a series connected module using ITO/Ag/Al is shown in Fig. 4.1-1.

The best high efficiency modules use 1000cm^2 quartz or pyrex substrates with approximately 5000Å textured CTO. Because of the relatively high cost of these substrates, development of the ITO/Ag/Al process is underway using small 3"x3" modules. Amorphous silicon depositions are made directly on 3"x3" substrates or on 12"x13" substrates which are subsequently cut into many 3"x3" substrates. Table 4.1-1 gives the best results for 3"x3" Al and ITO/Ag/Al modules.

Table 4.1-1 compares the results obtained on 3"x3" modules processed with ITO/Ag/Al metallization. The "best" V_{oc}, J_{sc}, FF, and η numbers are the highest observed for any module. However, no module is observed with all the best parameters in the same module. The typical parameters are more representative and often are observed together in one module. Table 4.1-2 gives the best results for a given module.

Generally, the ITO/Ag/Al metallization results in a J_{sc} that is ~0.6 to 0.9mA/cm^2 higher than that found in an identical module which uses Al. Most of this current increase is in the red response of the modules. Modules processed using ITO/Ag/Al generally have lower FF than those with Al back metal contacts. The FF for both Al and for ITO/Ag/Al modules can be improved by optimizing the segment width of the

FIGURE 4.1-1. CROSS SECTIONAL VIEW OF A SERIES CONNECTED SUBMODULE USING ITO/Ag/Al REAR CONTACT SCHEME.

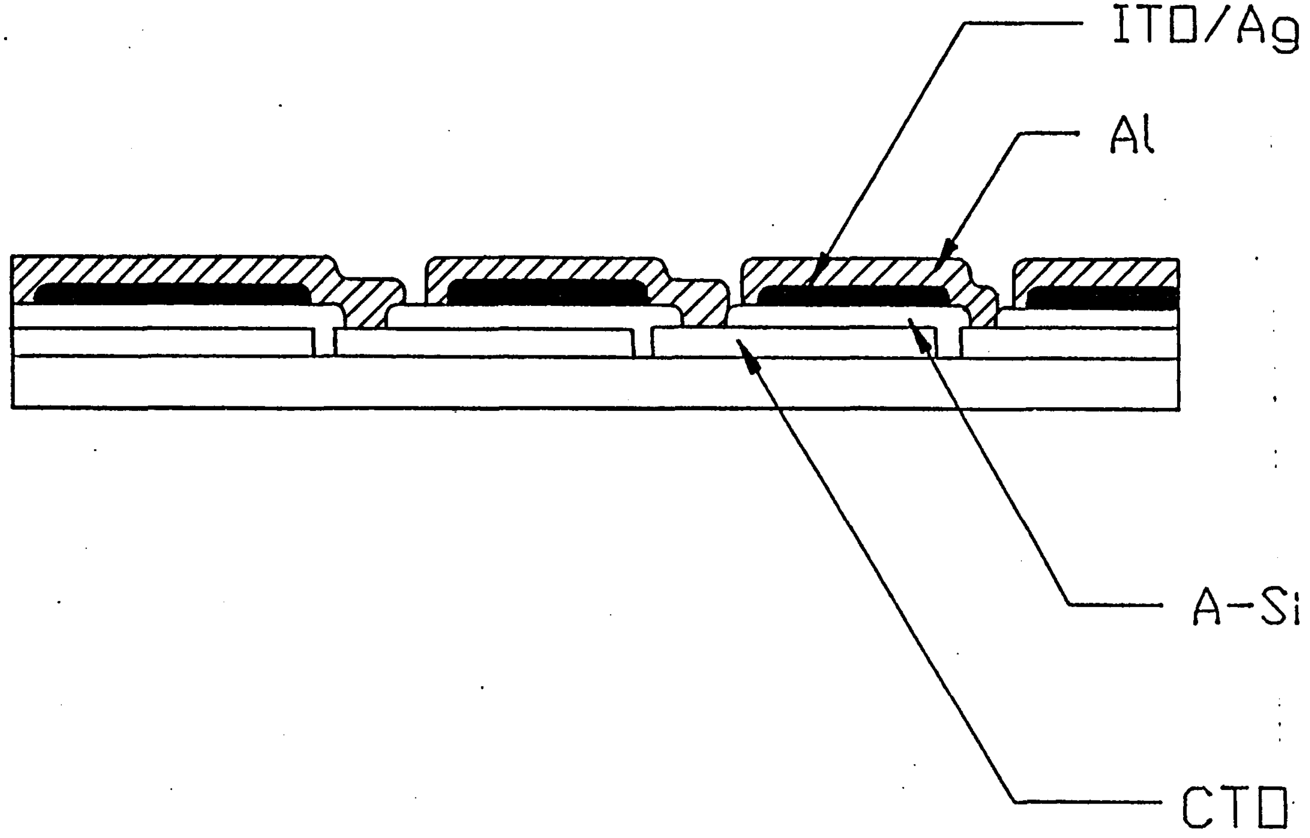

modules. Experiments are underway to optimize the segment width and compare theoretically predicted results to experimental results.

Assuming very modest parameters of V_{oc} = 880mV, J_{sc} = 16.5mA/cm^2, and FF = 0.7, a module efficiency over 10% can be obtained. It is believed that with optimization of the segment width all of these parameters will result in routine fabrication of high performance modules. Similarly this contacting method should yield very high (>13%) performance modules when coupled with the a-SiC/a-SiGe tandem devices.

4.2 STACKED JUNCTION MODULES

Over one hundred stacked junction modules have been made during the past six months, using an a-Si/a-Si stacked junction device structure (AM1.5, Xenon). The average active area efficiency of those devices was 6.07%. These devices incorporated a thin rear junction i-region. Degradation was accomplished by continuous exposure for 200 hours. Based on those tests we project a one year degradation of 14.8%. Little additional degradation occurs beyond this time. This is a major improvement over single junction devices.

4.3 ADVANCED SCRIBING PROCESSES

Solarex has recently developed advanced laser scribing processes that reduces the number of scribing stations from three to two. This two-step process has the advantage that modules proceed from amorphous silicon processing into metallization without breaking vacuum. The final interconnection and metal scribing is accomplished as a final process. Figure 4.3-1 illustrates the advantage of this process. The entire manufacturing line decreases in size which increases throughput and decreases capital equipment costs.

Standard SA-5 modules produced using the 2-step process have efficiencies equal to those processed in 3-steps (control). However, upon environmental testing (50 cycles of temp. (-40 to +90°C) and humidity), the 2-step modules fail, i.e., I_{ld} < 290mA. Initial results with an improved 2-step scribe show that upon sustained heat treatment at 150°C, 2-step modules perform as well as conventionally processed modules. This is shown in Fig. 4.3-2. However, these modules also failed environmental testing. Efficiencies dropped ~1% from initial test results. The efficiency loss is primarily observed in a drop in fill factor, with a slight increase in series resistance. Both V_{oc} and J_{sc} remain nearly unaffected.

FIGURE 4.3-1. COMPARISON OF THE PROCESS SEQUENCE FOR THREE STEP (ABOVE) AND TWO STEP (BOTTOM) LASER SCRIBING.

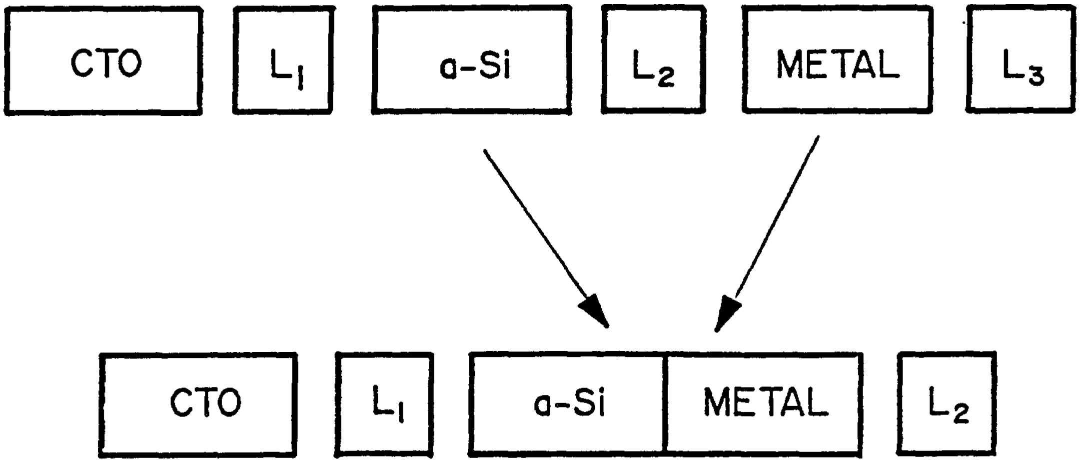

FIGURE 4.3-2. EFFECT OF SUSTAINED 150°C HEAT TREATMENT ON 3-STEP LASER SCRIBED CONTROL SUBMODULES AND 2-STEP SUBMODULES

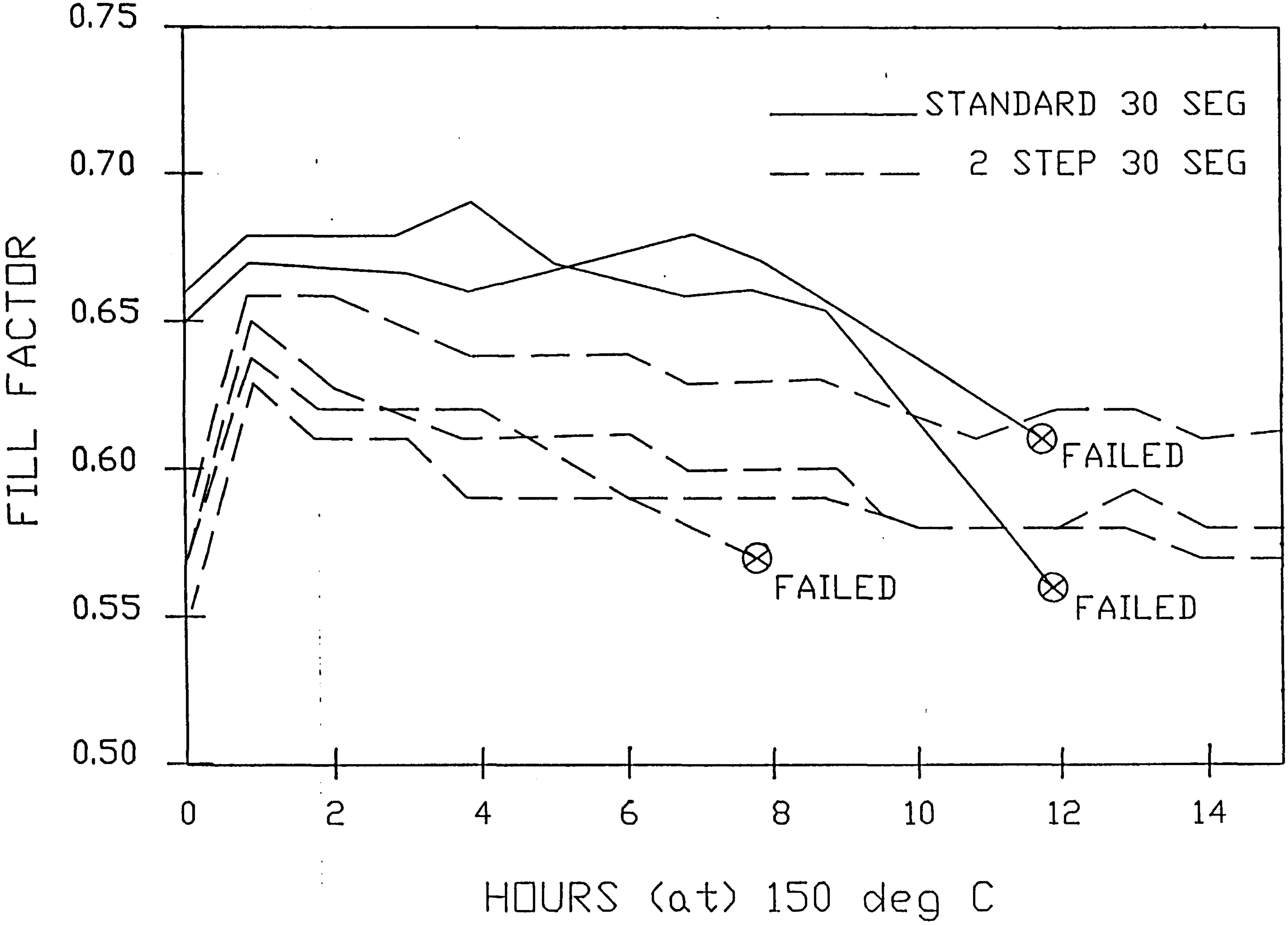

Table 4.1-1

Comparison of typical and best IV characteristics of 3"x3" modules

	Best	Typical
V_{oc}/segment	900mV	860-870mV
FF	0.67	0.64
J_{sc}	16.2mA/cm^2	15.8mA/cm^2
η_{act}	8.89%	8.6-8.8%

Table 4.1-2

Best IV parameters observed
together in 3"x3" modules

	Metal	#Seg	V_{oc}	FF	J_{sc}	η active
D2112	Al	5	4.492	.666	15.11	9.05
D2098	ITO/Ag/Al	5	4.352	.646	15.81	8.89

Outdoor testing of 2-step modules show that they continue to degrade slightly more than controls (see Fig. 4.3-3). However, these types of 2-step modules fail catastrophically when subjected to environmental testing. Modules with the improved 2-step scribe are currently under test by outdoor testing. It is encouraging that modules which fail catastrophically during environmental testing hold up fairly well in actual outdoor testing.

FIGURE 4.3-3. COMPARISON OF OUTDOOR TEST RESULTS OF 2 AND 3 STEP (CONTROL) LASER SCRIBED SUBMODULES.

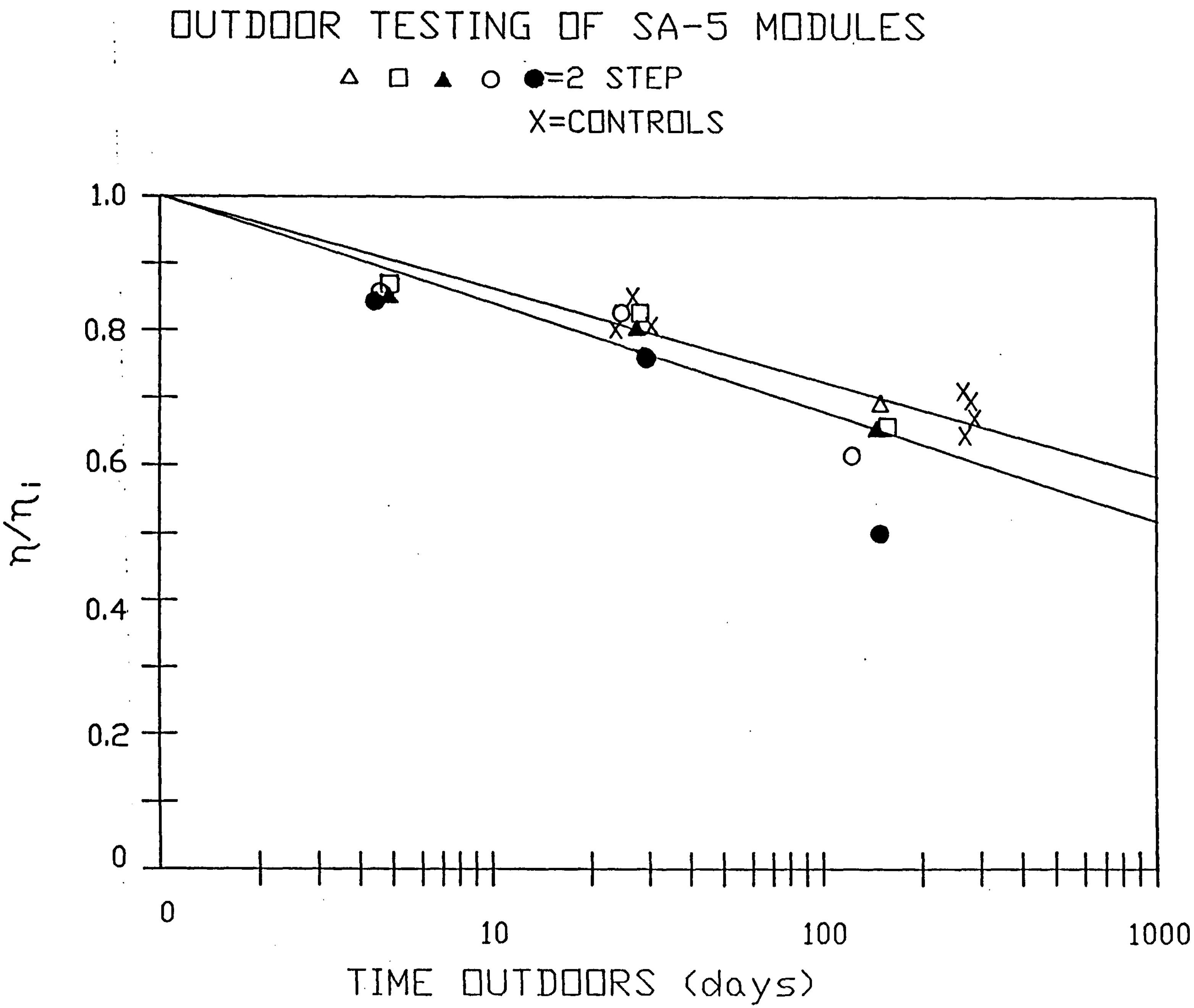

THE ROLE OF STRUCTURAL INHOMOGENEITIES ON THE TRANSPORT PROPERTIES OF a-SiGe:H

C.M. FORTMANN
Solarex Corporation, Thin Film Division, 826 Newtown-Yardley Road, Newtown, PA 18940

ABSTRACT

The defects that result from light soaking a-Si$_x$Ge$_{1-x}$:H are studied over the alloy range $0<X<0.4$. These defects act as recombination centers with a large hole capture cross section. The creation rate for light-induced defects is independent of the Ge content for compositions investigated ($x = 0$ to 0.4). The transport changes that result from Ge incorporation do not result in the creation of a larger density of these centers; however, the electronic transport properties decrease with increasing Ge content. The possibility that this decrease is due to germanium clusters is explored.

INTRODUCTION

The performance of a-SiGe:H alloys in solar cells has been disappointingly poor. The alloys have exhibited the unusual feature that the sub-bandgap absorption is not substantially higher than that of unalloyed amorphous silicon, while the electronic transport leads to relatively poor device performance [1]. There are three possible causes for the poor transport properties of annealed a-SiGe:H alloys. First the alloying of a-Si:H with Ge could lead to a higher density of the Si dangling bonds, the same defect that results from light soaking a-Si:H materials. Second, defects could result from the clustering of Ge atoms in the a-SiGe:H matrix. Finally, defects related to Ge content but not Ge clusters, perhaps Ge dangling bonds, could be responsible for the observed poor device performance.

To determine whether the Si dangling bond is responsible for the poor device performance, an investigation of light-induced changes in solar cells was conducted. The analysis of the SWQE (short wavelength quantum efficiency) [2] was used to characterize the light-induced recombination center. This technique takes advantage of the unique impact that the light-induced center has on the bias-light and voltage dependence of the SWQE in solar cells.

Light soaking an a-Si:H solar cell results in a loss in the SWQE (short wavelength quantum efficiency) which is shown by both our analysis of the SWQE and by numerical modelling [3] of device characteristics to be due to a reduction in hole lifetime. The reduction in SWQE (without light bias) is given by:

$$\Delta SWQE = qp_o(D-W_p-W_n)(\sigma_r \Delta N_r V_{th})/J_F \tag{1}$$

Where q is the electronic charge, p_o is the dark equilibrium hole concentration in the low field region of the i-layer, D is the i-layer thickness, σ_r is the capture cross section for holes when the center is occupied by an electron, N_r is the density of the recombination centers, and W_p and W_n are the depletion region widths at the p-i and n-i interface respectively. The last term ($\sigma_r N_r V_{th}$) characterizes the recombination center. The light soaking of a series of cells with differing i-layer thickness determines N_r as it is the only parameter that is a strong function of light soaking time, while D is the only device dependent parameter.

The reduction in transport properties that accompanies Ge content has also been explored. The decrease in electron mobility that accompanies Ge incorporation has been studied on both films [4] and devices [5] (thin film transistors). The assumption that the light-induced defects and those created as a result of Ge incorporation are both due to dangling bonds has

Mat. Res. Soc. Symp. Proc. Vol. 118. ©1988 Materials Research Society

been considered in the literature [6]. The possibility that the defects related to Ge are due to Germanium clusters has been explored. High density regions larger than 40Å have been observed by TEM in RF grown materials [4]. It is assumed that clusters of this size would result in bond relaxation to that of Ge within crystalline Ge resulting in the bond and anti-bond levels being within the bandgap of thea-SiGe:H matrix. Clusters of smaller size (4 to 7 atoms) would result either through the preferred bonding of Ge atoms with other Ge atoms or would arise naturally in high concentration (>20% Ge) alloys if atoms of Ge and Si mixed randomly (EXAFS studies suggest random mixing [7]).

The effect of a germanium atom cluster can be inferred from recent a-Si:H/a-Ge:H superlattice investigations. A cluster of Ge atoms could reduce the electron transport due to either charge trapping (Wronski [8] reports band discontinuities of 0.55eV at the conduction band and 0.15eV at the valence band) or enhanced recombination resulting from the higher carrier concentrations in the potential wells formed by the cluster. It is less likely that the decrease of transport is due to interface states at the boundary between the cluster and the surrounding matrix because Wronski [9] also reports that the density of interface states in a-Si:H/a-Ge:H superlattices is no larger than the density of states in a-Ge:H ($\sim 10^{17}\,cm^{-3}$). EXAFS studies of a-Si:H/a-Ge:H multi-layers [10] demonstrated that the Ge atoms in multi-layer structures were bonded equally to other Ge atoms and Si atoms for Ge layers one monolayer in thickness, indicating that the fabrication of multi-layered structures does not necessarily result in an increase in dangling bonds or other deleterious structure. Further general descriptions of the optical, electrical and mechanical properites of a-Si:H/a-Ge:H superlattices can be found in the literature [11-13].

In this work the multi-layers of a-Si:H/a-Ge:H are used to specifically study the impact of reduced electron mobility on the film characteristics and the device performance. Also the analogy between clusters and Ge layers can be carried further, through the use of repeat spacings that are appropriately chosen. The repeat spacing of the a-Si:H/a-Ge:H multi-layers studied here was chosen such that the number of atoms in the Ge layers would bracket that expected from 5 to 7 atom spherical clusters in the a-$Si_{0.8}Ge_{0.2}$:H (assuming random mixing with no energy differential between Si-Si, Ge-Si and Ge-Ge bonds). The thickness of the Ge layers studied were approximately one to two monolayers thick with repeat spacing ranging from ∼700 to 1200Å.

EXPERIMENTAL

p-i-n solar cells were used to characterize the electronic transport properties of a-Si_xGe_{1-x}:H and a-Si:H/a-Ge:H multi-layers. To aid in the diagnostics of the light degradation of a-SiGe:H, solar cells were prepared with different i-layer thickness (X∼0.2) and Ge content (X=∼0 to 0.4). The deposition conditions used for the a-SiGe:H layers and devices as well as the conditions used for the light soaking of the solar cells has been described previously [14]. Two series of multi-layers (films and devices) were prepared by the deposition of a-Ge:H layers at a rate of <2Å/sec for 3 and 5 seconds, while a-Si:H layers were deposited at the rate of ∼4Å/sec. Films were deposited onto quartz substrates with metal patterns for conductivity measurements and SIMS characterization.

DISCUSSION

Figure 1 shows the quantum efficiency of an a-$Si_{0.8}Ge_{0.2}$:H solar cell as a function of wavelength, bias light, bias voltage and light soaking time. The annealed a-$Si_{0.7}Ge_{0.2}$:H and a-Si:H solar cells have similar SWQE. The a-SiGe:H solar cells have a characteristic voltage dependency of the LWQE (long wavelength quantum efficiency) which results in a lower fill factor than a-Si:H cells of comparable i-layer thickness. The voltage dependence

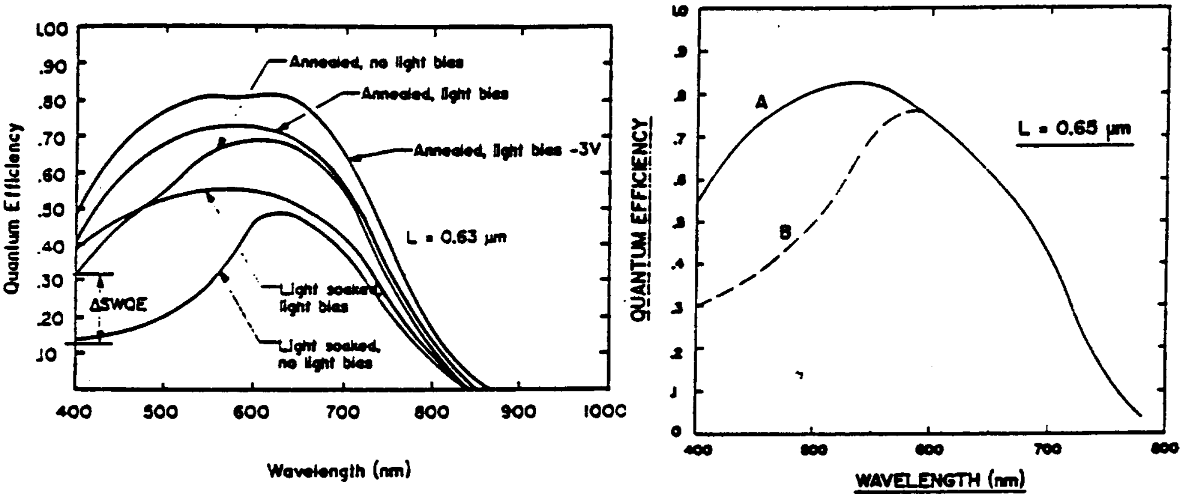

Figure 1. The QE of an a-$Si_{0.8}Ge_{0.2}$:H solar cell (left) and the QE of an annealed (A) and light soaked (B) a-Si:H solar cell (right).

of the LWQE increases with increasing Ge content. The a-SiGe:H solar cells show a similar decrease in SWQE at a wavelength of 400nm (Δn_{400}) due to light exposure as that of the a-Si:H cells of similar thickness as seen in Figure 2. The fill factor for solar cells as a function of Ge content and light soaking time is also shown in Figure 2. These results indicate that the defect related to Ge content is not a-Si dangling bond. Further it shows that the rate of dangling bond formation is not dependent on the Ge content or bandgap dependent, since the ΔSWQE is proportional to the dangling bond density.

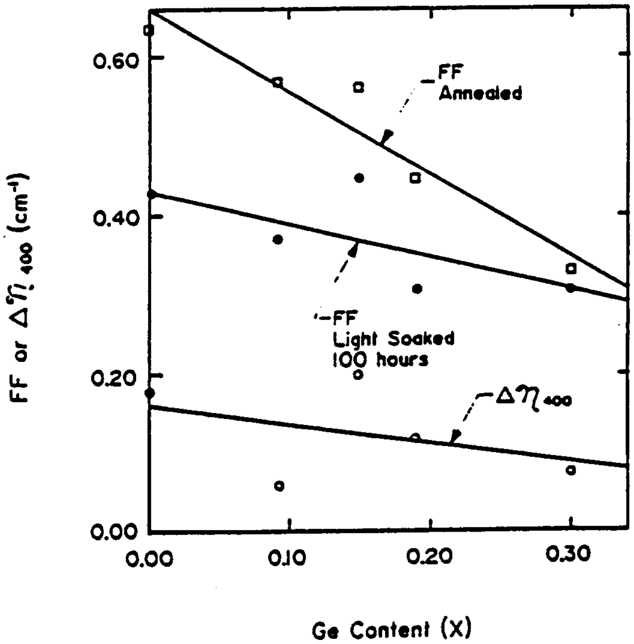

Figure 2. The effect of light soaking on p-i(a-Si_xGe_{1-x}:H)-n solar cells with 'x' ranging from 0 to 0.3.

Light soaking decreases amorphous solar cell performance. The effect is characterized by a reduction in fill factor and the resulting loss in solar conversion efficiency. The degradation of the SWQE is modeled with equation (1) as an increase in the hole capture cross section due to an increase in the density of recombination centers. Unlike the changes that result from light soaking, the transport properties of a-SiGe:H alloys cannot be uniquely determined through either a solar cell or film measurement as reduction in either or both carrier mobilities [15] will cause a fill factor loss that is not related to the dangling bond with it's characteristic SWQE loss. Therefore, it is necessary to rely on both film measurement as well as device characterization in order to study the Ge related defects.

The electron mobility in annealed a-Si$_x$Ge$_{1-x}$:H decreases with increasing Ge content to a large degree independently of the preparation method [16]. The decrease in photoconductivity due to Ge incorporation is much greater than the decrease in the photoconductivity associated with light soaking in a-Si:H [17]. The suppression of photoconductivity by Ge incorporation can be simulated through the incorporation of Ge monolayers in an a-Si:H film or solar cell i-layers. The performance of devices and the film characteristics of multi-layers is shown in Figure 3. The long wavelength absorption (leV) of the multi-layers studied here is no larger than that high quality a-Si:H (Figure 4).

The parameters of a-Si:H, a-Si:H/a-Ge:H and a-Si$_{0.8}$Ge$_{0.2}$:H solar cells are compared in Table 1. The SWQE of cells with a multi-layer i-layer is no smaller than that of an a-Si:H cell of similar thickness, indicating that the density of Si-dangling bonds is no higher than that in a-Si:H. These multi-layer films and solar cells provide a system with relatively poor transport which does not have a large density of dangling bonds. The alloy and the mulit-layer cells have a similar reduction in fill factor and LWQE.

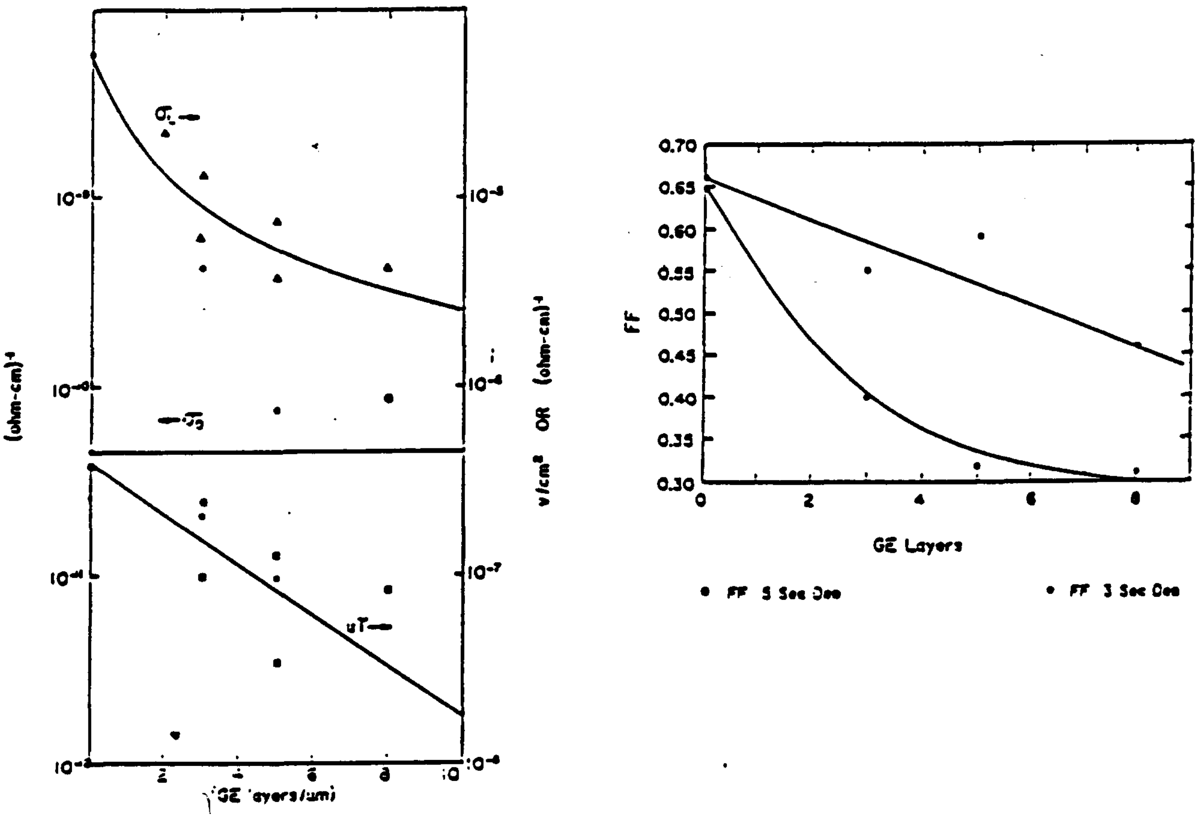

Figure 3. The photoconductivity, dark conductivity, μτ product (left) and solar cell parameters (right) as a function of the number of Ge layers in a film ~0.8μm thick.

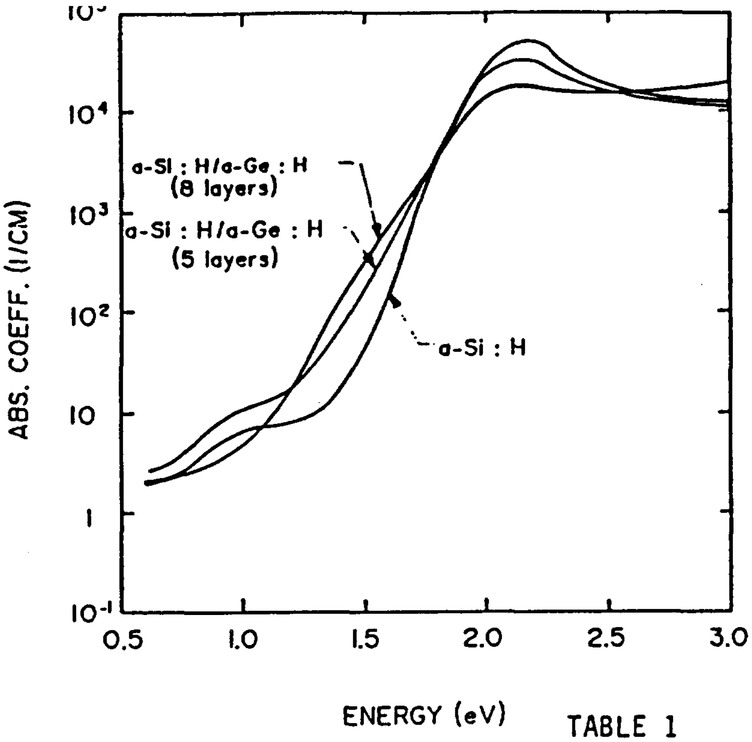

Figure 4. A PDS scan of a-Si:H, and of a-Si:H/a-Ge:H multi-layers 5 Ge layers and 8 Ge layers.

TABLE 1

COMPARISON OF a-Si:H, a-SiGe:H, and a-Si:H/a-Ge:H CELL DATA

Property	Std. Cell	a-SiGe:H	a-Si:H/a-Ge:H
Cell #		781	776
V_{oc}	0.83	0.758	0.793
FF	0.62	0.49	0.355
J_{sc}	16.0	17.4	15.9
SWQE Ratio	0.93	0.87	0.92
LWQE (0/-3V) (AM1 bias illumination)	0.92	0.76	0.80

CONCLUSIONS

The performance differences between a-Si:H and a-SiGe:H devices can be accounted for by a lower electron mobility of these materials. The reduction in hole mobility and the resulting poor device performance is not due to an increase in Si dangling bonds. The rate of increase in Si-dangling bonds due to light exposure is independent of Ge content over the composition range studied.

The defects that result from Ge incorporation are examined by a-Si:H/a-Ge:H multi-layers. The transport properties and device performance of a-SiGe:H and the multi-layer structure are similar. These similarities include the voltage dependency of the LWQE solar cells, the poor conductivity of films on insulating substrates, and the low long wavelength absorption measured by PDS. The similarity of a-SiGe:H and a-Si:H/a-Ge:H film and device properties support the hypothesis that Ge clusters are responsible for the reduction in transport properties of the alloy; however direct evidence is lacking. We are currently exploring the possibility of clustering with Raman scattering; however, this is a formidable task due to the small number of atoms expected to be in the clusters.

This work has been partially supported by SERI under Contract No. ZB-3-03056.

REFERENCES

1. J.L. Newton, G. Wood and A. Catalano, Proc. 19th IEEE PVSC, p. 862-866 New Orleans, LA (1987).
2. C.M. Fortmann, S. Lange, M. Hicks and C.R. Wronski, to be published.
3. M. Hack and M. Shur, J. Appl. Phys. 58 (4), (1985).
4. K.D. Mackenzie, J.R. Eggert, D.J. Leopold, Y.M. Li and W. Paul, Phys. Rev. B Vol. 31, No. 4 (1985).
5. P. Yan, N. Lichtin and D. Morel, Appl. Phys. Lett. 50 (19) (1987).
6. Z E. Smith, S. Aljishi, V. Chu, J. Condo and S. Wagner, Tech. Dig. Int'l. PVSEC-3, Tokyo, Japan (1987).
7. A. Filippone, P. Fiorini, F. Evangelisti, A. Balerna and S. Mobilio, Proc. 7th EC PVSEC, p. 1202-1204, Seville, Spain (1986).
8. C.R. Wronski, P.D. Persans and B. Abeles, Appl. Phys. Lett. 49, 569 (1986).
9. C.R. Wronski and M. Hicks, Jap. Journ. Appl. Phys., Vol. 26 no. 2, (1987) p. L105-L107.
10. F. Sette, B. Abeles, L. Yang, A. McDowell, D. Norman, C.H. Richardson, J. Non-Cryst. Solids 97&98 (1987) p. 895-898, North-Holland, Amsterdam.
11. B. Abeles and T. Tiedje, Phys. Rev. Lett. 51 (1983) 2003.
12. P. Persans, B. Abeles, J. Scanlon and H. Stasiewski, Proc. 17th Int'l. Conf. Phys. of Semiconductors eds. J.D. Chadi and W.A. Harrison (Springer-Verlag, NY, 1985) 499.
13. B. Abeles, T. Tiedje, K.S. Liang, H.E. Stasiewski, J.C. Scanlon and P.M. Eisenberger, J. Non-Cryst. Solids 66, 35 (1984).
14. C.M. Fortmann, J. O'Dowd, J. Newton and J. Fischer, "Stability of a-Si Alloy Materials & Devices", B.L. Stafford and E. Sabisky Eds., AIP Conf. Proc. 157, AIP, NY (1987).
15. M. Hack and M. Shur, Vol. J. Appl. Phys. 58 (2) (1985).
16. K.D. Mackenzie, J.H. Burnett, J.R. Eggert, Y.M. Li, and W. Paul to be published.
17. C.R. Wronski "Semiconductors and Semimetals Volume 21, part C", J.I. Pankove Ed., p. 351 Academic Press, NY (1984).

APPENDIX I

SEMIANNUAL REPORT # 2 FROM THE UNIVERSITY OF FLORIDA

By

K. Misiakos and F.A. Lindholm (Principal Investigator)

To: Murray Bennett, SOLAREX

From: F.A.Lindholm and K.Misiakos, University of Florida

Subject: Semiannual Report # 2

Period: January - June 1988

SERI Subcontract K #RB-6-06003

I. INTRODUCTION

In this report we present numerical results on the various kinetic models proposed in the literature to explain the degradation of amorphous silicon thin films. So far there are only two complete kinetic rate moles published, one by Stutzmann [1] and recently another by Redfield [2]. Numerical results suggest that neither model can explain the experimentally observed degradation as a function of device thickness and bias. To overcame this problem we propose a modified version of Redfield model that is successful in reproducing experimental results.

There are two sectionsin this report. The first contains the details and the numerical results of the models discussed above. The second is on the influence of the interface traps at the a-Si$_{1-x}$C$_x$:H/a-S$_i$:H heterojunction on the stability and the performance of the cells. The basic device structure is shown in Fig. 1. The incident light is the SERI tabulated AM1.5 spectrum. To model the light trapping process we followed the model by Schade and Smith [3]. Glass and transparent layer reflection and absorption coefficients were provided by SOLAREX.

Before presenting the modeling parameters, we have to point out that we included the recombination from tail states to dangling bonds in addition to the recombination from free carriers to dangling bonds. Provided that there are more hole tail states than electron tail states, the incorporation of the tail state to dangling bond recombination results in an effective hole capture cross section well above the effective electron capture cross section. A large hole capture cross section is essential in the numerical simulation of experimental efficiencies and open circuit voltages .

Below is a list of the parameters used in the modeling.

Table 1.

Band gap of P layer (eV)	2.1
Electron affinity of P layer (eV)	3.53
Band gap of I and N layers (eV)	1.67
Band gap of the 100Å transition layer (eV)	1.8-1.67
Electron affinity of I and N layers (eV)	3.96
Electron affinity of the transition layer (eV)	3.83-3.96
Conduction band tail states	
$G_A(E) = G_A \exp((E-E_c)/E_A)$	
G_A $(cm^{-3}\ eV^{-1})$	10^{20}
E_A (eV)	0.03
Valence band tail states	
$G_D(E) = G_D \exp((E_v-E)/E_D)$	
G_D $(cm^{-3}\ eV^{-1})$	10^{20}
E_D (eV)	0.045
Initial dangling bond density	
in the P layer (cm^{-3})	$8x10^{16}$
in the I layer (cm^{-3})	$2x10^{15}$
in the N layer (cm^{-3})	$2x10^{17}$
Density of gap states in the I layer	
Density of states N_c=N_v (cm^{-3})	2×10^{19}
Doping Density	
N_A (cm^{-3}) in the P layer	$2x10^{18}$
N_D (cm^{-3}) in the N layer	$5x10^{18}$
N_A and N_D (cm^{-3}) in the I layer	10^{15}
Activation energy for acceptor dopants (eV)	0.4
Activation energy for donor dopants (eV)	0.2
Thickness of P and N layers .	100Å
Electron mobility in the heavily doped layers $(cm^2s^{-1}v^{-1})$	10
Hole mobility in the heavily doped layers $(cm^2s^{-1}v^{-1})$	1
Electron mobility in the I layer $(cm^2s^{-1}v^{-1})$	15

Hole mobility in the I layer $(cm^2 s^{-1} v^{-1})$	2
Dielectric constant in all three layers	11.7
Transition rates $(cm^3 s^{-1})$	
$e \rightarrow D^+$	10^{-8}
$e \rightarrow D^0$	2×10^{-9}
$h \rightarrow D^-$	7×10^{-10}
$h \rightarrow D^0$	2×10^{-9}
Optical Tauc parameters	
P layer	
E_g (eV)	2.1
C $(eVcm)^{-1/2}$	550
I and N layer	
E_g (eV)	1.7
C $(eVcm)^{-1/2}$	700
Reflection coefficient of the back contact	0.9

The Urbach energies were determined by smoothly joining the Tauc and Urbach relations at $\alpha = 10^4$ cm^{-1}. The heterojunction was modeled by assuming an energy uniform distribution of donor and acceptor states having a surface density of 10^{12} cm^{-2} and a dangling bond surface density of 10^{11} cm^{-2}.

II. DEGRADATION MODELS

A. Stutzmann model

According to this model the generation rate of new dangling bonds, G_{DB}, is proportional to the tail to tail recombination which, in turn, is proportional to the pn product: G_{DB}=Cpn, where C is a constant. This model was combined with numerical programs that solve the carrier transport equations in the cell to simulate the degradation as a function of the cell thickness. Experimentally it has been found that plotting the degradation vs time in a semilogarithmic scale results in a straight line having a slope that is an increasing function of the cell thickness, as shown in Fig. 2.

It turned out that Stutzmann model can not account for these qualitative features of the experimental results. Figures 3, 4, 5, 6 summarize the results on Stutzmann model. These plots show the degradation of a thin, 0.2 μm, and a thick, 0.62 μm, cell as a function of time under open circuit conditions. The trap capture cross sections and carrier mobilities are changed in a way so that the efficiency and the open circuit voltage have realistic values. These performance variables are given at the end of this section The general conclusion from these plots is that using Stutzmann model we can not realistically simulate the experimental degradation data. In Figure 3 the slope does substantially change with thickness but the delay for the thick sell is unrealistic. In Figure 4 (A1) the slopes of the two plots are not much different and the less degradation of the thin cell is mainly due to a higher delay. The same is true for Figures 5 (A2) and 6 (A3).

Here I list the modeling and performance variables for the cells of the figures. In all plots, except Fig. 6 , the electron and hole mobilities were 15 and 2 for the heavily doped regions and 30 and 5 cm^2/Vs for the intrinsic layer, respectively. In Fig. 6(A3) the same mobilities were 10 and 1 for the heavily doped and 15 and 2 cm^2/Vs for the intrinsic layer. In all the figures, with the exception of Fig. 3, the recombination transition probabilities are the same as the ones measured by Street: Hole to neutral trap: 7E-10, hole to negatively charged trap: 2E-9, electron to neutral trap: 2E-9, electron to positively charged trap: 1E-8 cm^3/s. In Fig. 3 the transition probability to neutral traps was 2.8E-9 while the same probability to charged traps was 2.8E-8 cm^3/s. The tail states participate in the recombination up to a depth of 0.3 eV below the conduction band and above the valence band. In Fig.5(A2) this depth is 0.4 eV for holes. The transition probabilities of the free carriers to the tail states are a hundred times less than the ones to the traps. The density of dangling bonds at the P-Buffer layer heterojunction is 1.E11 /cm^2. The initial performance parameters under AM1.5 conditions are as follows.

Figure	3		4(A1)		5(A2)		6(A3)	
Thickness	.2	.62	.2	.62	.2	.62	.2	.62
I_{sc}(mA)	13.8	15.7	14	16.3	13.9	16.1	13.9	16.1
Voc(mV)	841	839	884	885	855	850	887	880
Eff(%)	9.2	9.1	10.4	11.4	10	9.8	10.2	10.3

B. Redfield Model

According to Redfield the rate equation for the density of metastable defects is

$$dN_M/dt = C_1N_LR-v_2N_M-C_2N_MR+v_1N_L \qquad (1)$$

where R is the recombination rate, v_1 and v_2 the thermal transition coefficients and C_1 and C_2 are recombination inducing rate coefficients, $v_1=v_{10}\exp(-E_1/kT)$ and $v_2=v_{20}\exp(-E_2/kT)$ where E_1 is the energy required to generate a metastable defect while E_2 is the annealing energy. N_M is the metastable defect density and N_L the latent defect center density: $N_T = N_L + N_M$, where N_T is the density of total potential defect sites. C^1 and C_2 are about equal to the unit cell volume (10^{-22} cm^3).

This original model had to be modified because it predicted an unusually fast degradation at the beginning and a virtual saturation after few hours. The first change to be made was that generation of new defects, as well as the annealing of old defects, occurs through tail to tail recombination instead of recombination through defects. Under this assumption the initial degradation rate was more realistic. Problems, however, persisted because of early saturation and considerable delays. This is shown in Figure 7 where the degradation at open circuit of a thin cell is shown. Plots A, B, C, D, E correspond to different values of the activation energies and rate coefficients. The objective was to reduce delay and obtain a realistic scope. As Fig. 7 shows, this turn out to be impossible. In addition, all plots tend to saturate, something that can be predicted by equation (1).

To overcome this problem two different defect types were introduced with different kinetic rate coefficients. The two parameters of the two different types are shown below.

Table 2.

	TYPE 1	TYPE 2
C_1 (cm^3)	0.2C1	0.06C1
C_2 (cm^3)	0.4C2	0.1C2
v_{10} (s^{-1})	10^{10}	10^{10}
v_{20} (s^{-1})	10^{10}	10^{10}
E_1 (eV)	1.06	1.12
E_2 (eV)	0.96	1.02
N_T (cm^{-3})	0.5NT	.8*NT

where $C1-210^{-22}$, $C2-10^{-22}$ cm^3 and $NT-310^{17}$ cm^{-3} are the values provided by Redfield. The activation energies and rate coefficient were chosen so that when the first defect type saturates the second turns on, so that the degradation is a logarithmic function of time. The very first part of the degradation is dominated by defect type 1 while type 2 dominates for very long times. Degradation results are shown in Fig 8. The two curves show the degradation of a thin (0.2 μm) and a thick (0.62 μm) cell at open circuit. For times greater than an hour the degradation rate on a logarithmic scale becomes straight line with a slope of 10% per decade for the thin cell and 15% per decade for the thick cell. Considering the experimental results, these plots seem to be realistic. Figure 9 shows the degradation of the open-circuit voltage and short circuit current for the same cells. The open circuit voltage degradation is minor, 35 and 25 mv drop after 600 hours for the thick cell and the thin cell, respectively. The same is true for the short circuit current of the thin cell, a 3% loss after 600 hours. The thick cell I_{sc} initially degrades slowly, though faster than the thin cell I_{sc}. However, after 20 h of stressing its degradation increases substantially. For long times the efficiency loss for the thick cell is evenly divided between the short circuit current loss and the fill factor loss.

Figure 10 shows the degradation at short-circuit condition. These plots have the same slope as under open circuit conditions but, at the same time, they are shifted to the right introducing a delay, in accordance with experimental observations (Fig. 2).

III. INFLUENCE OF INTERFACE TRAPS ON PERFORMANCE AND STABILITY

Figure 11 shows the influence of the interface trap density on the cell performance. For an interface trap density in the middle 10^{11} cm^{-2} the open circuit voltage depends on the interface recombination and is almost independent from the thickness. As the interface trap density gets smaller the bulk recombination becomes more important and the thinner cell has higher open circuit voltage. Eventually, for a very low interface density the open circuit voltage saturates to a bulk limited value, 960 mV and 980 mV for the thick and the thick cell, respectively.

The efficiency is also sensitive to the interface trap density. For low trap densities the efficiency of the thin cell exceeds the efficiency of the thick cell because of higher open circuit voltage and fill factor. When the interface trap density decreases the short circuit currents stay virtually the same, the fill factor of the thin cell remains almost constant while the fill factor of the thick cell slightly decreases.

Figure 12 shows the influence on the stability of two different interface trap densities. The cells with the higher interface trap density degrade less, and although they start at a lower initial efficiency they end up being more efficient after several tens of hours of open circuit stressing. Figure 13 explains this behavior. For higher interface trap density the pn product, the driving force of dangling bond generation in the bulk of the cell, is lower throughout the cell resulting in enhanced stability.

Finally, Figure 14 shows how the pn product changes with stress and terminal bias. For prolonged stressing the pn product drops considerably making the degradation rate a decreasing function of time. Atshort circuit conditions, the pn product in most of the cell is orders of magnitude less than it is at open circuit conditions. This explains why the degradation drops when the terminal bias increases. Figure 14 also suggests that at short circuit conditions most of the dangling bonds are generated near the N^+ layer.

REFERENCES

[1] M. Stutzmann, W. Jackson and V. Tsai, Phys. Rev. B 32, 23 (1985)

[2] D. Redfield, Appl. Phys., Lett., 52, 292 (1988)

[3] H. Schade and Z.E. Smith, J. Appl. Phys. 57, 568 (1985)

FIGURE CAPTIONS

Figure 1. Band diagram of the cell under consideration.

Figure 2. SOLAREX experimental results on the cell degradation.

Figure 3, 4, 5, 6 Numerical results on the degradation using Stutzmann model

Figure 7. Numerical results on the Redfield model with only one defect type

Figure 8. Numerical results on the open circuit degradation with two defect types. Degradation parameters are shown in table 2.

Figure 9. Open circuit and short circuit current degradation at open circuit. Degradation parameters are shown in table 2.

Figure 10. Degradation under open circuit and short circuit conditions.

Figure 11. Open circuit voltage and efficiency as a function of the interface trap density.

Figure 12. Efficiency degradation as a function of the interface trap density.

Figure 13. pn product as a function of the interface trap density for a 0.62 μm cell (13a) and a 0.2 μm (13b) cell.

Figure 14. pn product as a function of the accumulated stress hours at open circuit and at short circuit conditions.

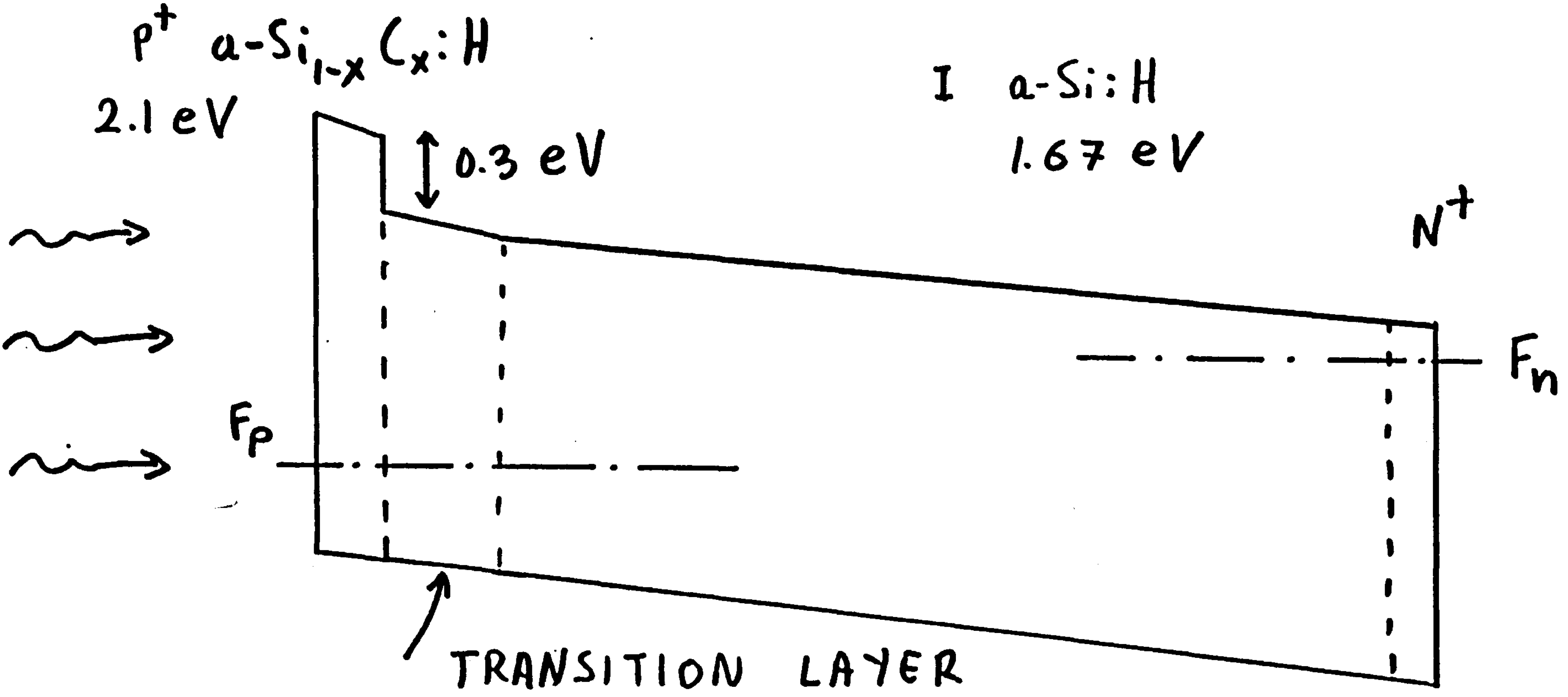
p^+ $a\text{-}Si_{1-x}C_x:H$
2.1 eV
0.3 eV
I a-Si:H
1.67 eV
N^+
F_n
F_p
TRANSITION LAYER

Fig. 1

11. M. Bennett, J.L. Newton, R.R. Arya and K. Rajan; 18th IEEE Conf. Procedings (Las Vegas, 1986) p. 1569.

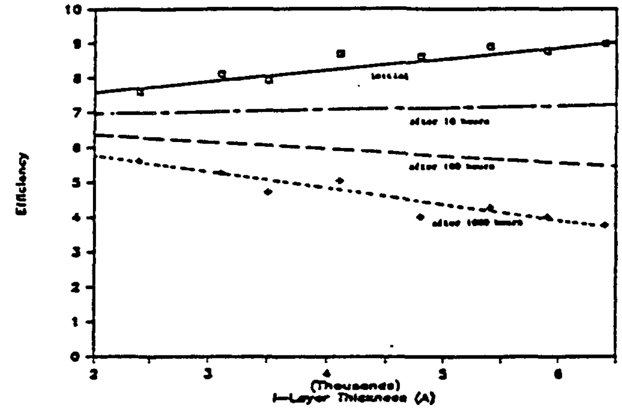

FIGURE 1
Efficiency as a function of i-layer thickness initially (——), and after 10 hrs (— —), 100 hrs (—.— —), and 1000 hrs (——).

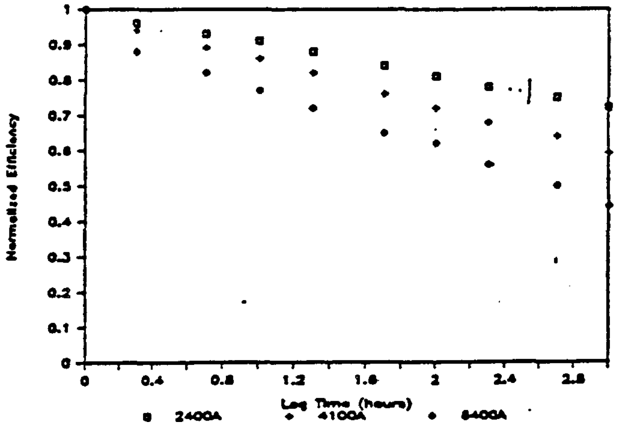

FIGURE 2
Relative degradation rate of cells with different i-layer thicknesses.

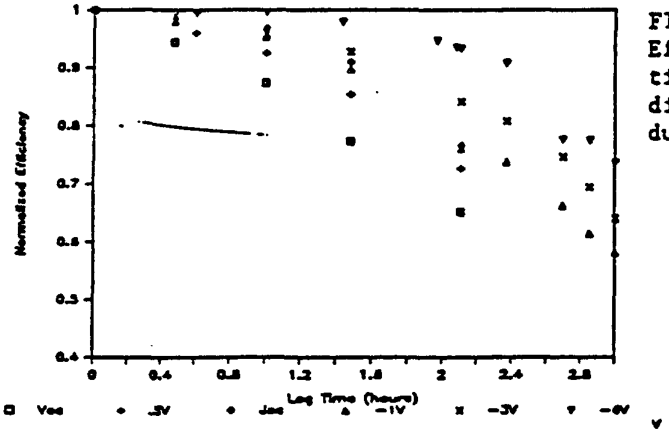

FIGURE 3
Efficiency as a function of time for cells held at different bias levels during degradation.

Fig.2.

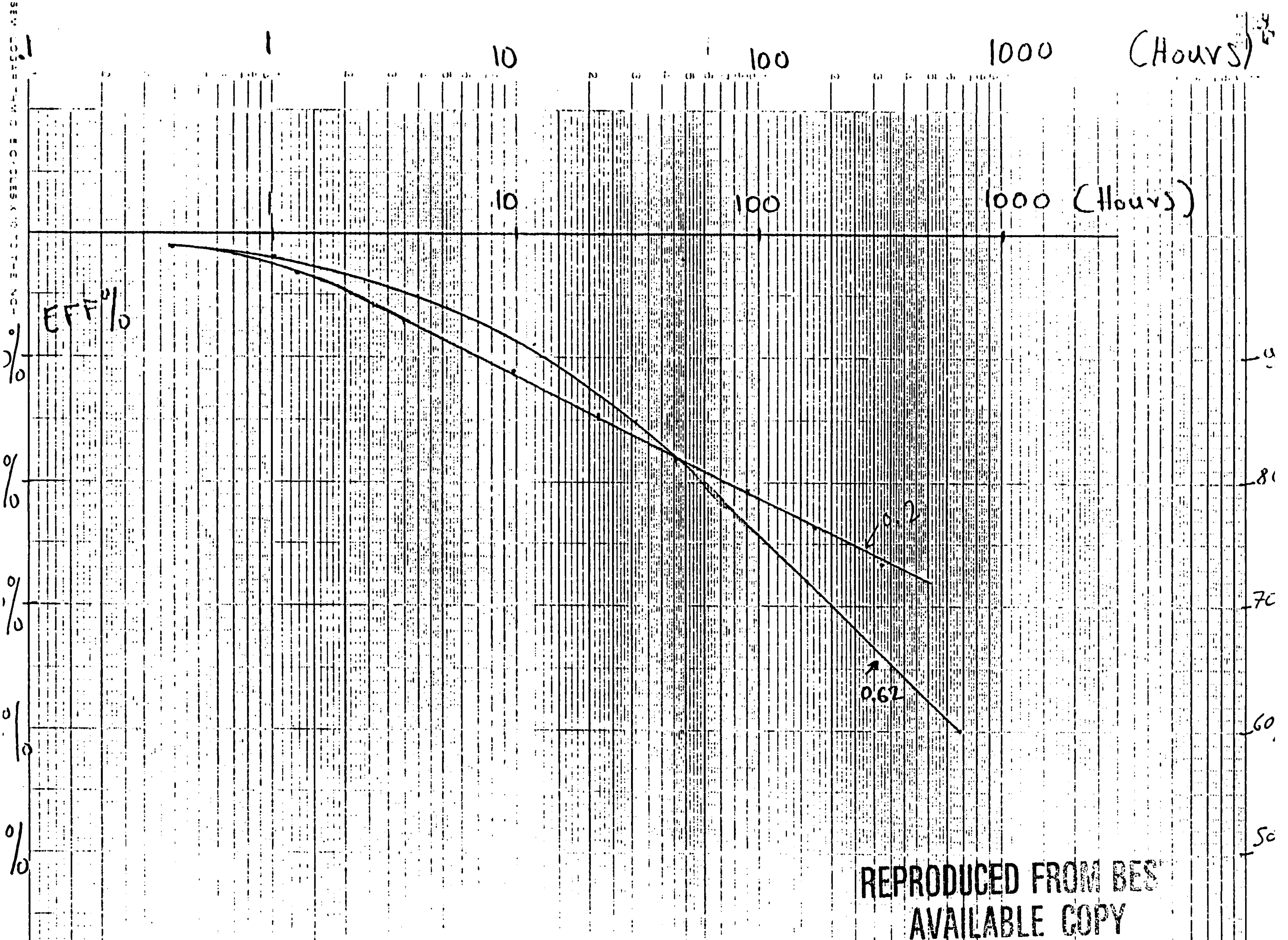

REPRODUCED FROM BEST
AVAILABLE COPY

Fig. 3

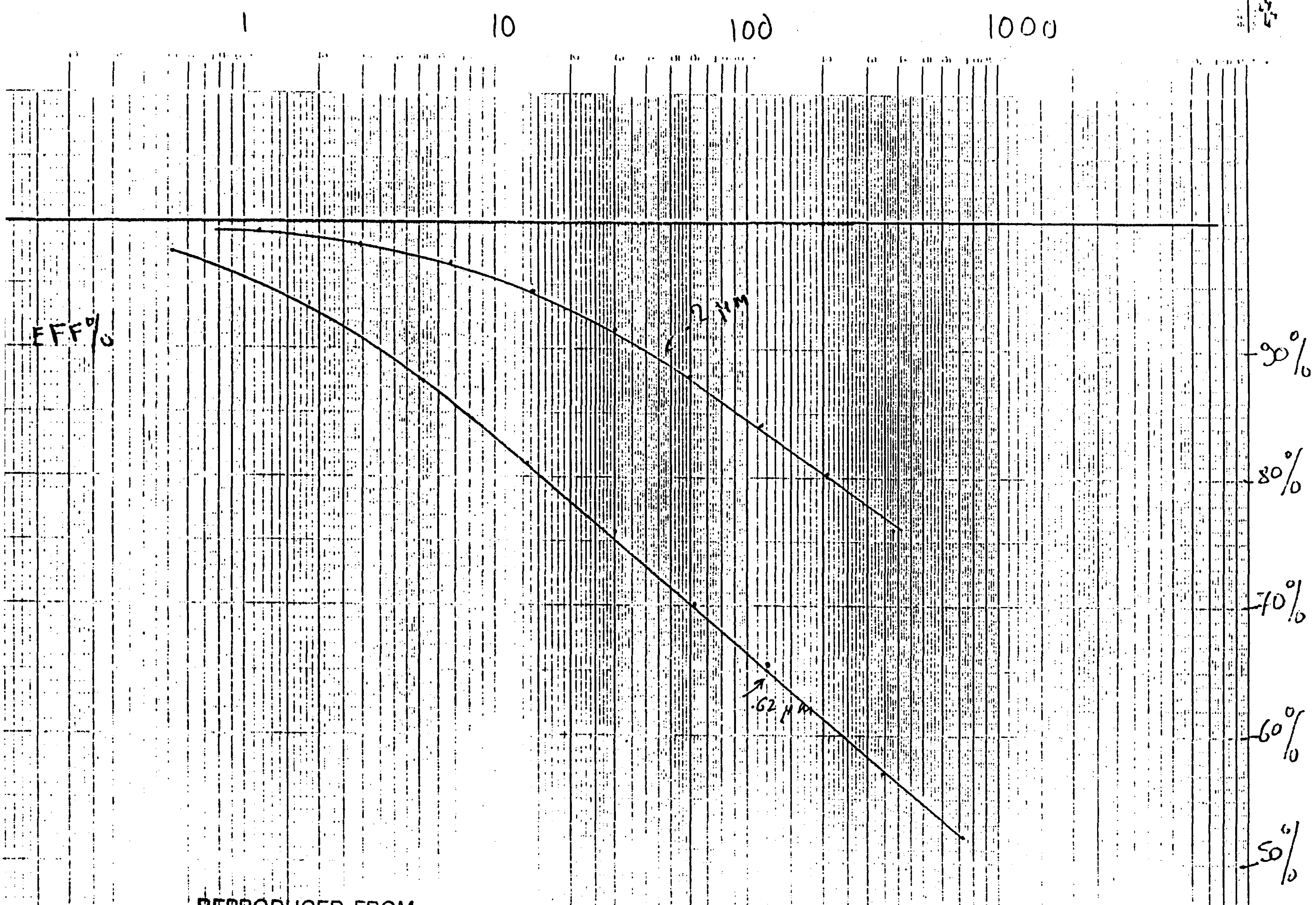

REPRODUCED FROM
BEST AVAILABLE COPY

Fig. 4

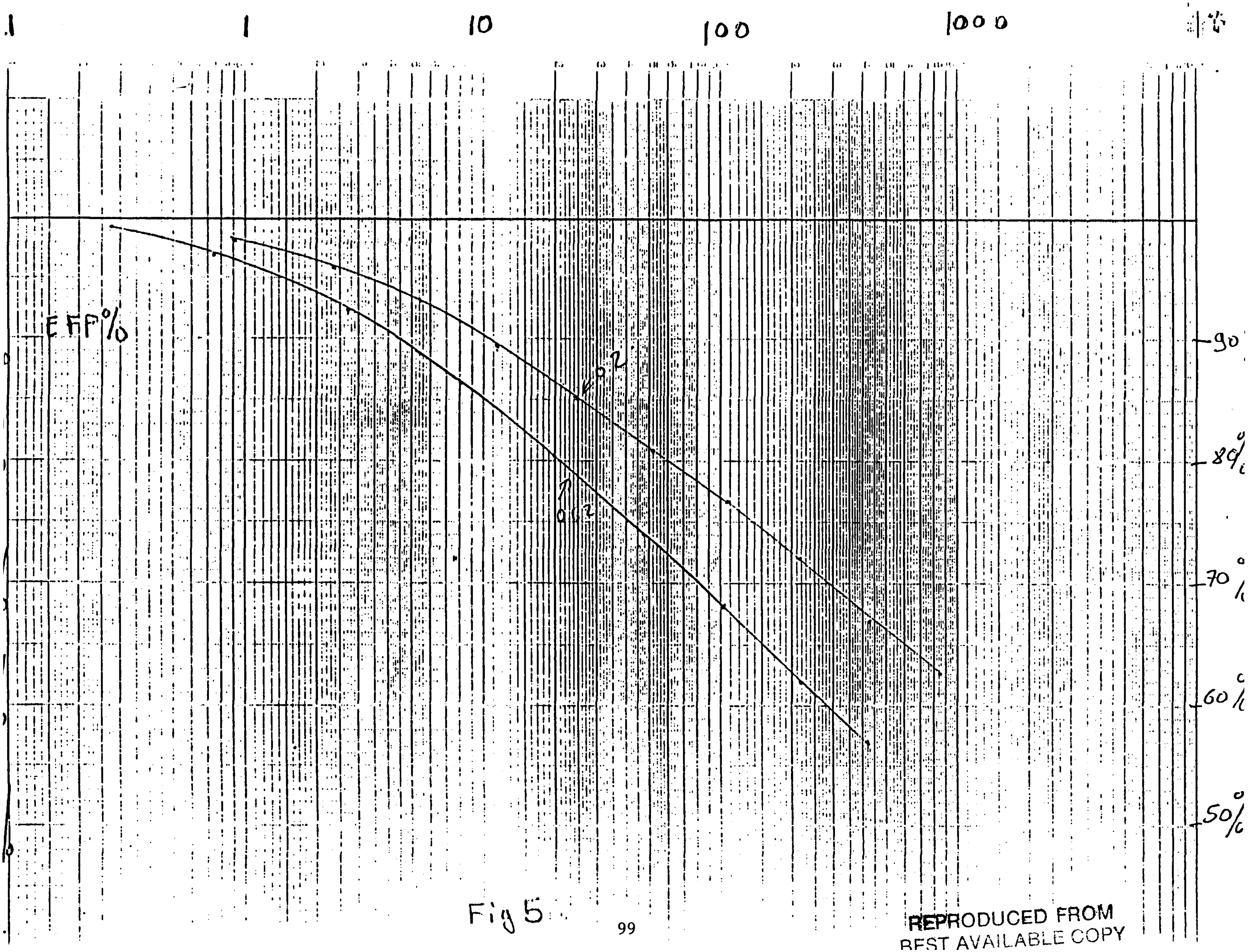

Fig 5

REPRODUCED FROM
BEST AVAILABLE COPY

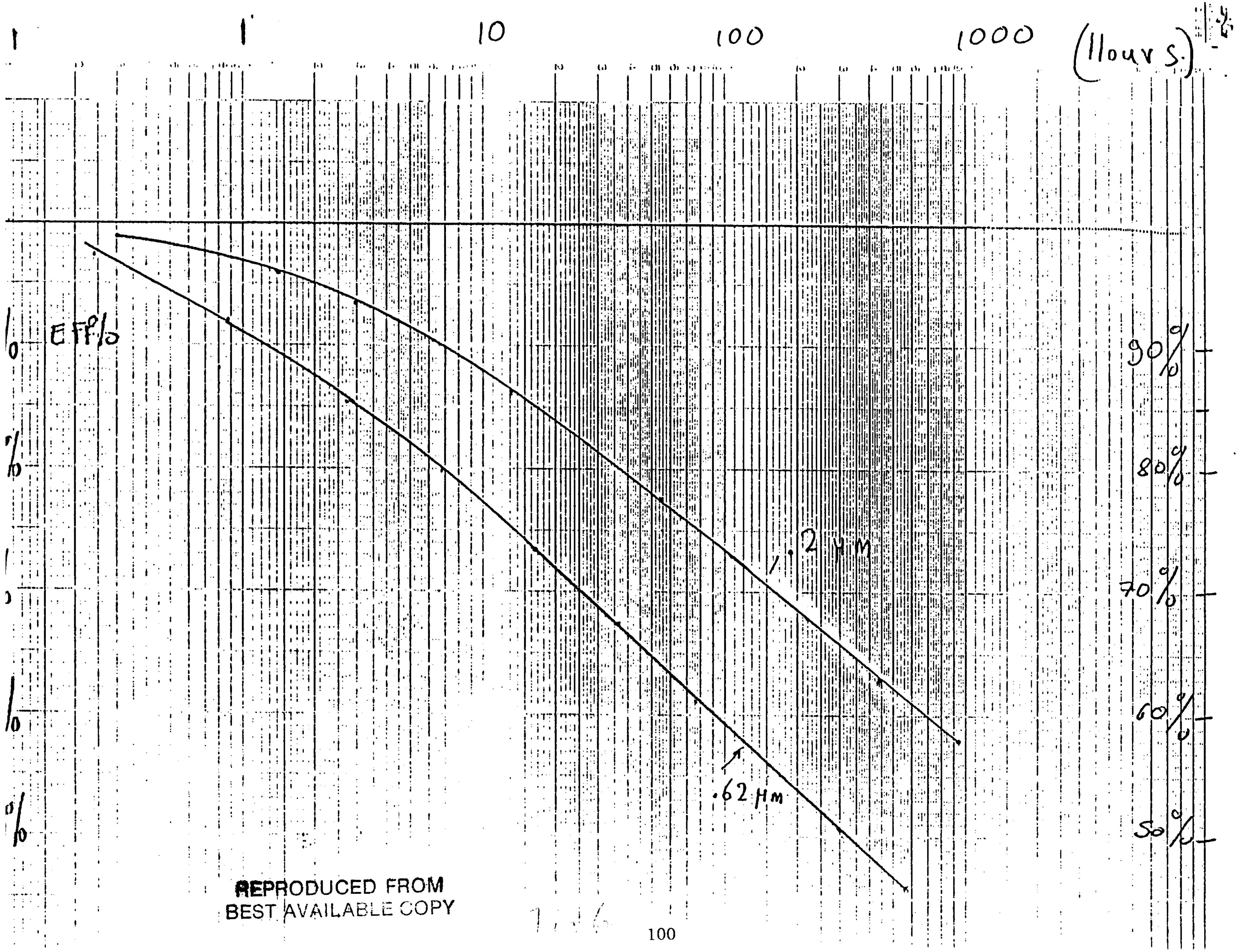

REPRODUCED FROM
BEST AVAILABLE COPY

model

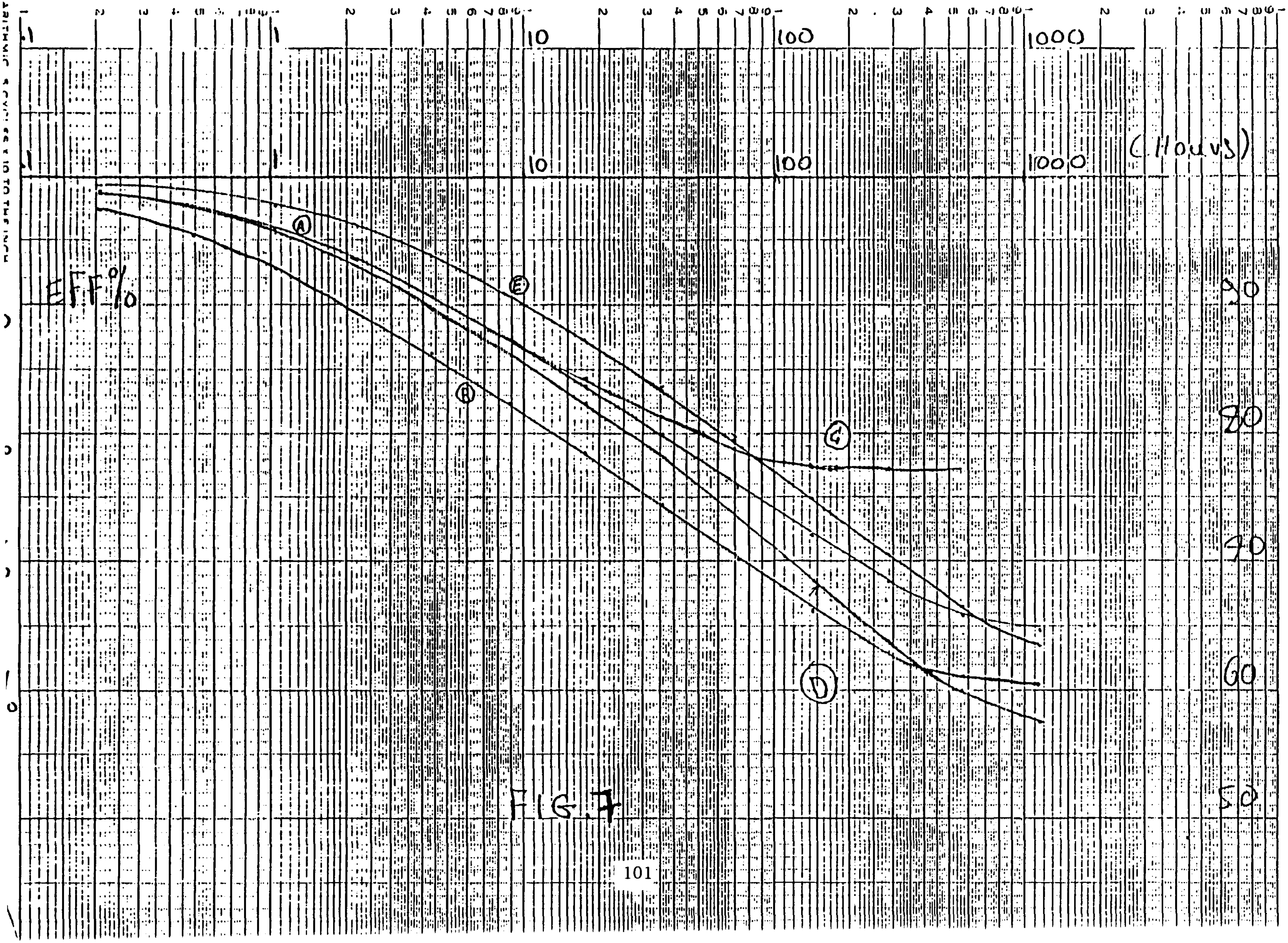

FIG. 7

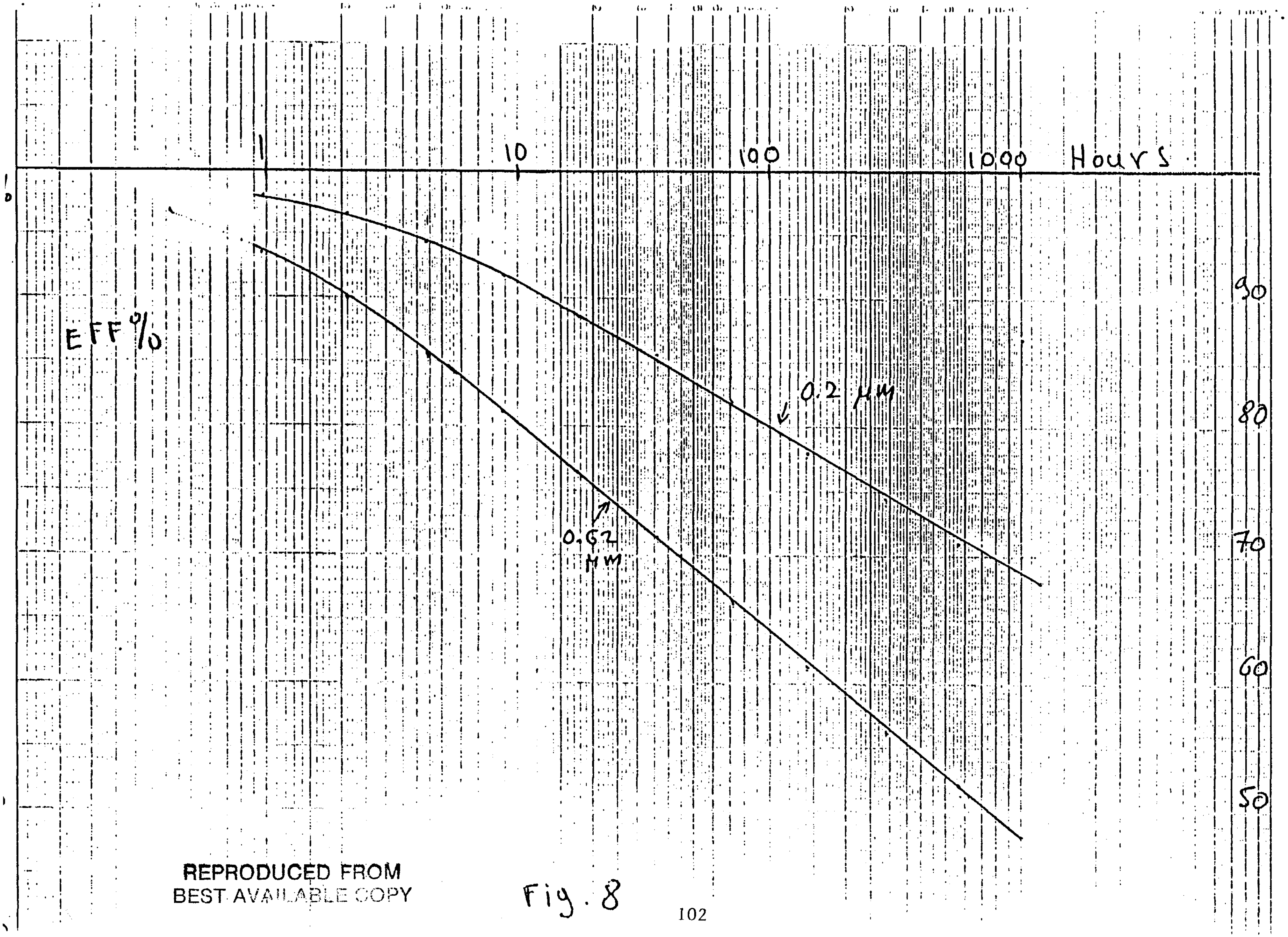

REPRODUCED FROM BEST AVAILABLE COPY

Fig. 8

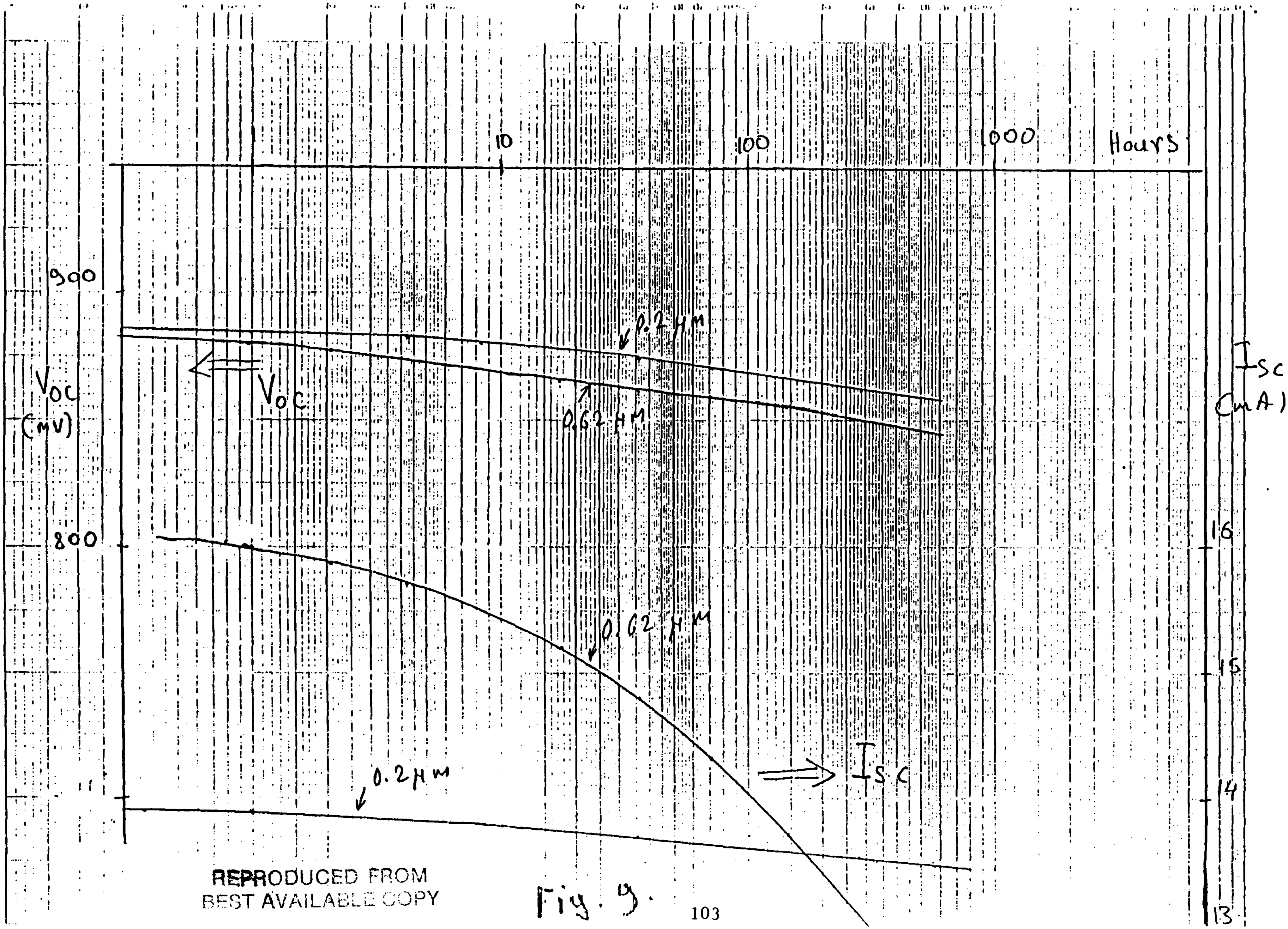

REPRODUCED FROM
BEST AVAILABLE COPY

Fig. 9.

REPRODUCED FROM
BEST AVAILABLE COPY

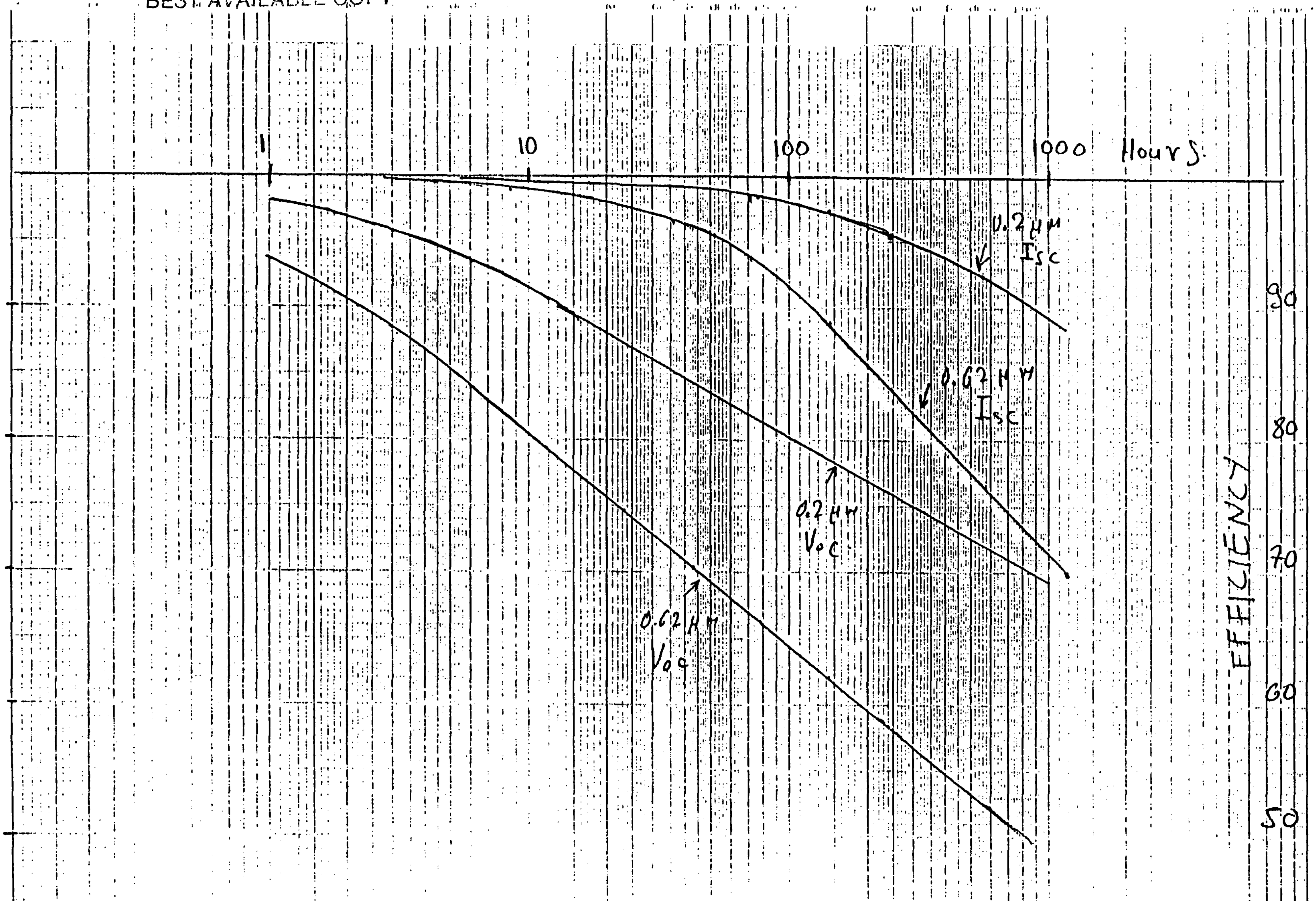

Fig. 10

Isc ≈ Constant 0.62 → 16 mA 0.2 → 13.8

FF : 0.62 0.69 – 0.66 0.2 : 0.78 – 0.77

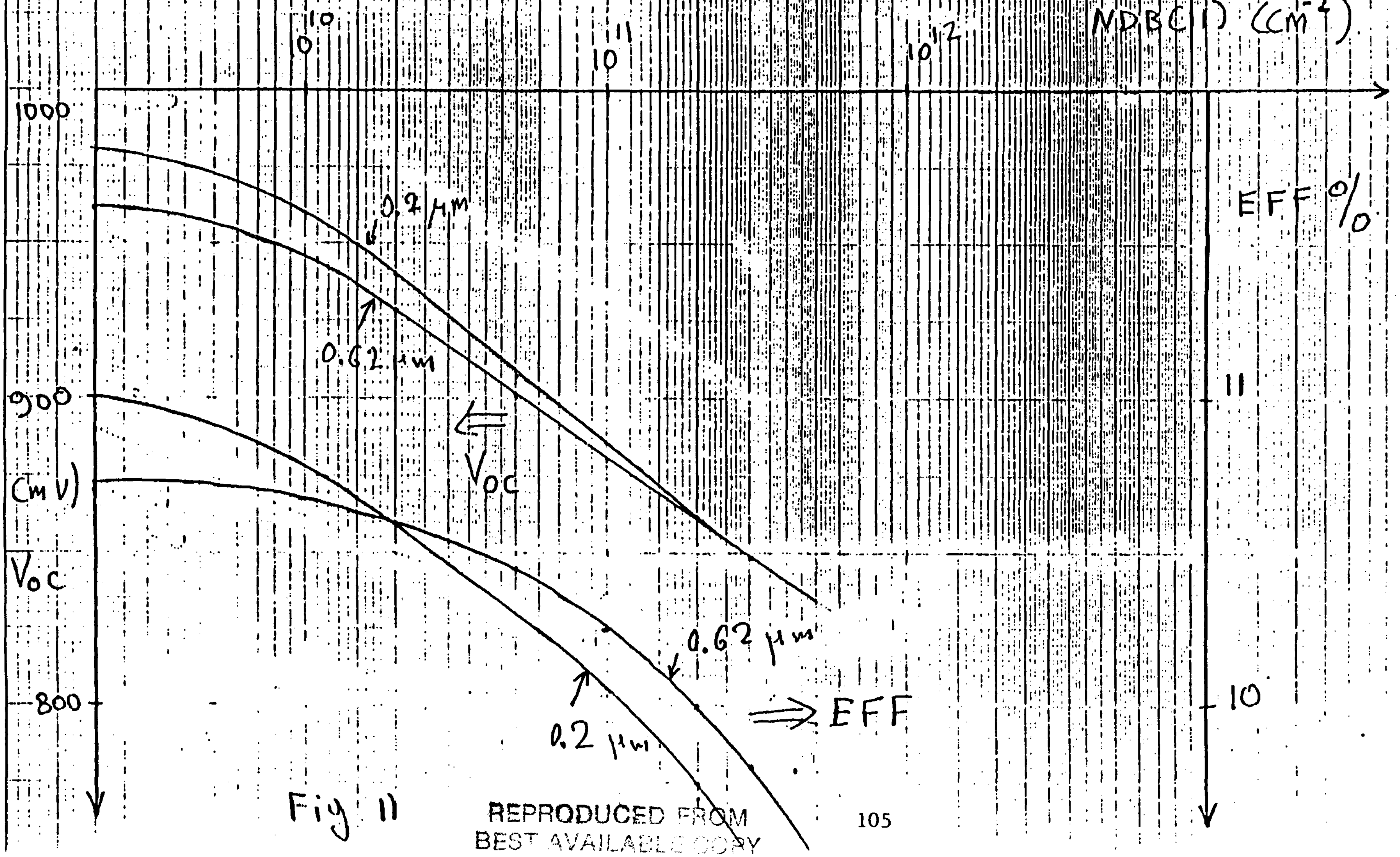

Fig 11

REPRODUCED FROM
BEST AVAILABLE COPY

REPRODUCED FROM
BEST AVAILABLE COPY

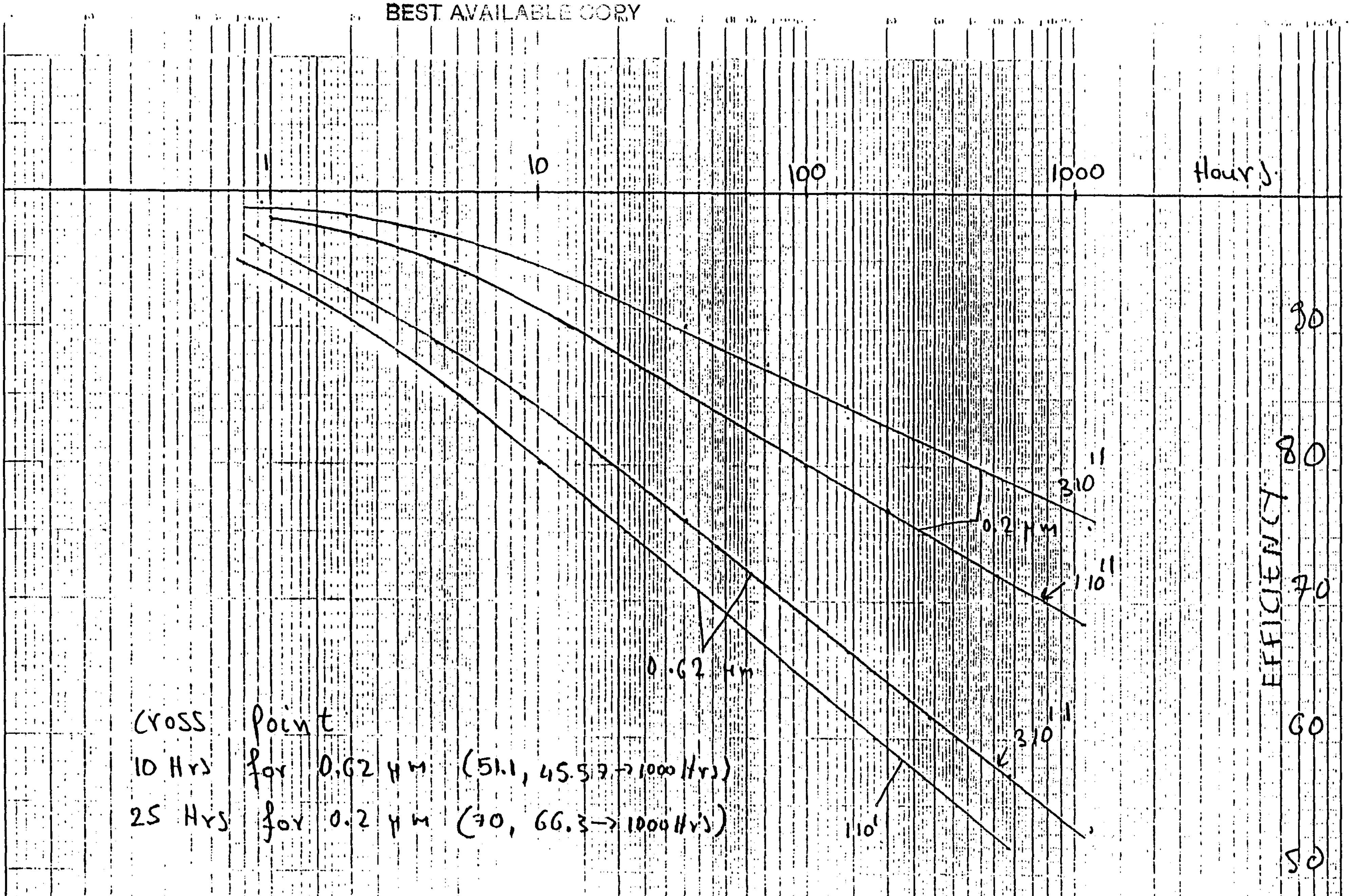

Cross point
10 Hrs for 0.62 μm (51.1, 45.57 → 1000 Hrs)
25 Hrs for 0.2 μm (70, 66.3 → 1000 Hrs)

Fig. 12.

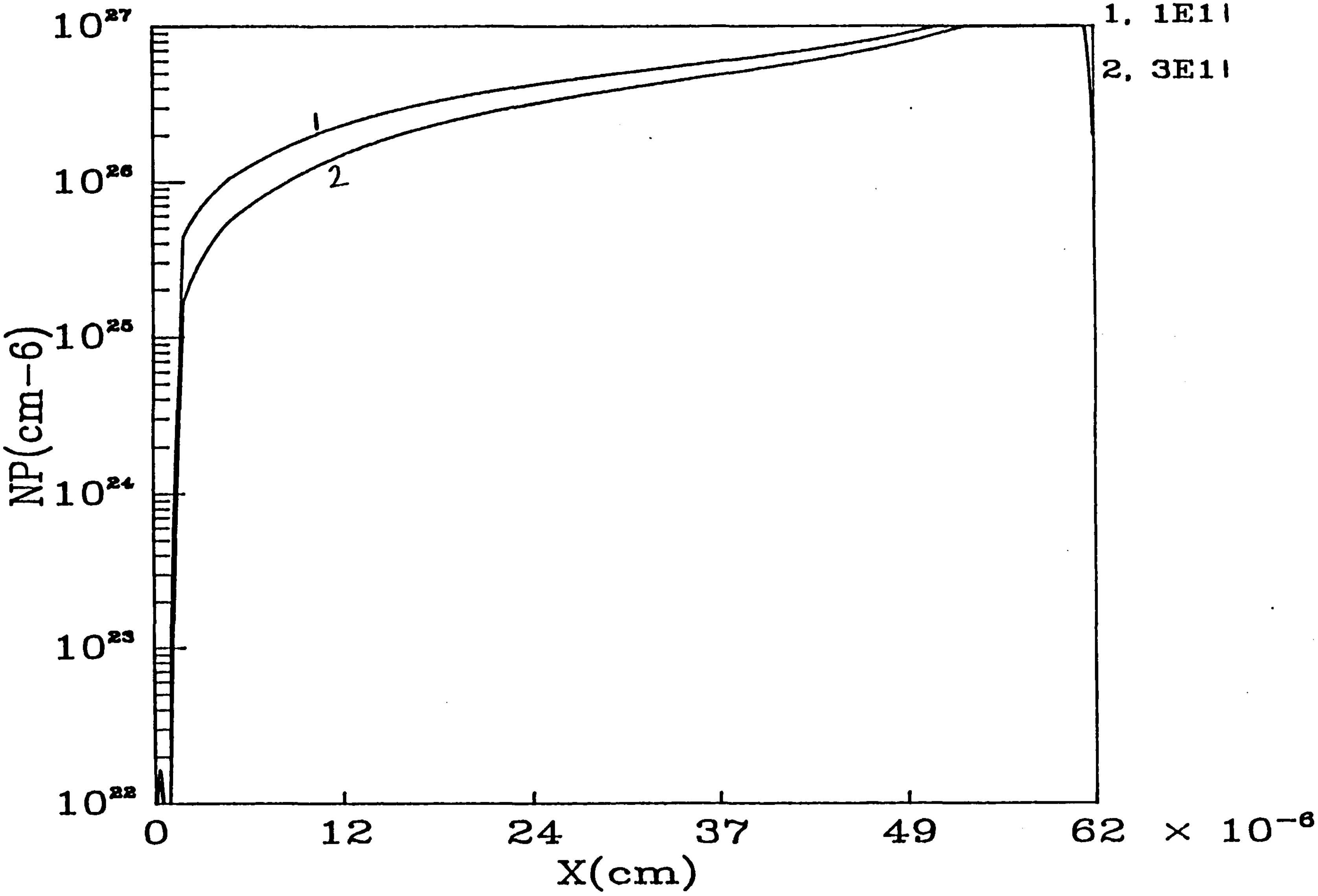

PN PRODUCT

Fig. 13 a

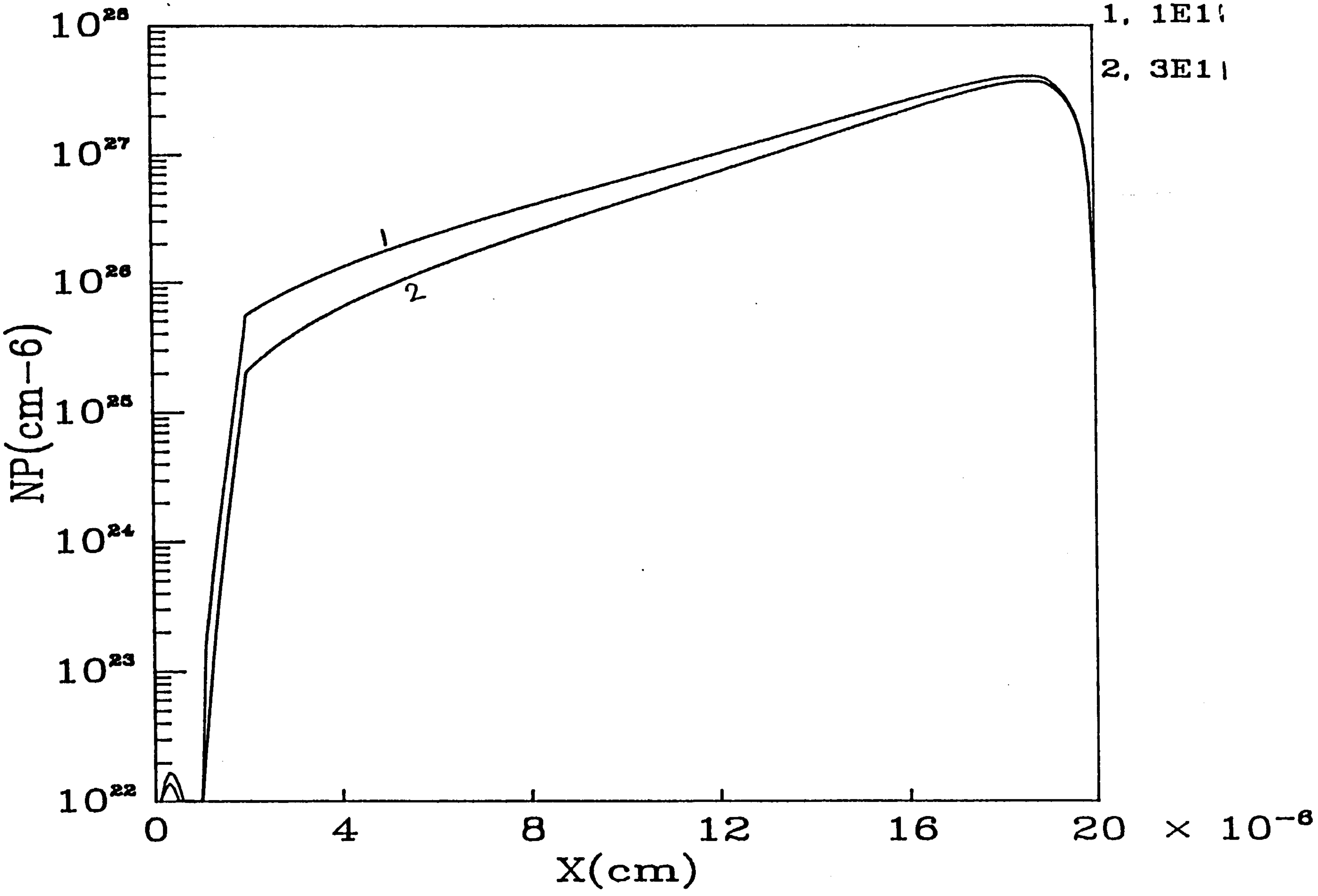

PN PRODUCT

Fig. 13b

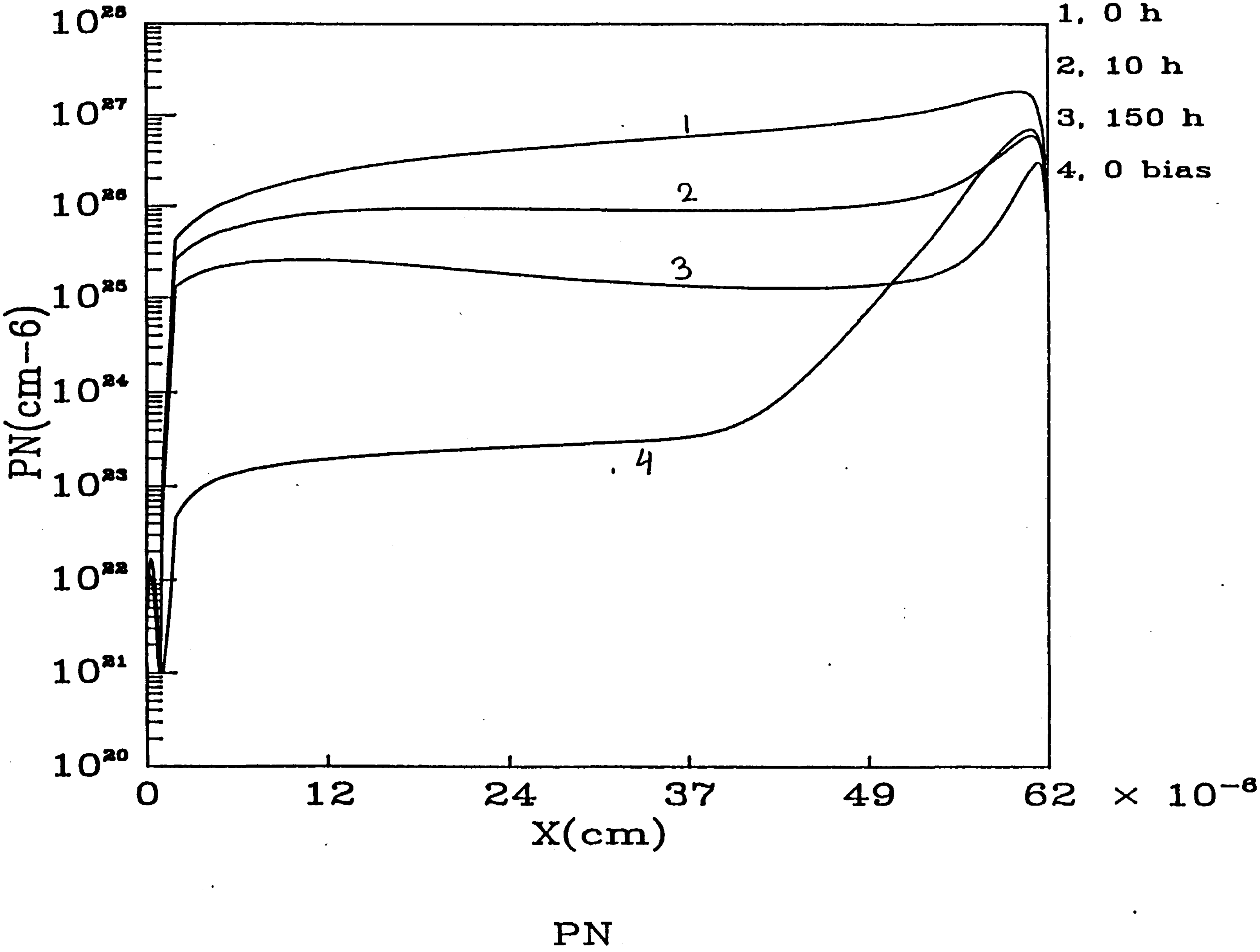

PN(cm-6)
10^{28}
10^{27}
10^{26}
10^{25}
10^{24}
10^{23}
10^{22}
10^{21}
10^{20}
0
12
24
37
49
62
$\times 10^{-6}$
X(cm)
1, 0 h
2, 10 h
3, 150 h
4, 0 bias
1
2
3
4
PN

Fig. 14

Document Control Page	1. SERI Report No. SERI/STR-211-3583	2. NTIS Accession No. DE89009496	3. Recipient's Accession No.

4. Title and Subtitle

Research on High-Efficiency, Single-Junction, Monolithic, Thin-Film Amorphous Silicon Solar Cells, Phase II Semiannual Report, 1 Feb 1988 - 31 July 1988

5. Publication Date
October 1989

6.

7. Author(s)
R.R. Ayra et al

8. Performing Organization Rept. No.

9. Performing Organization Name and Address

Solarex Thin Film Division
826 Newtown-Yardley Road
Newtown, Pennsylvania 18940

10. Project/Task/Work Unit No.

11. Contract (C) or Grant (G) No.
(C) ZB-7-06003-2
(G)

12. Sponsoring Organization Name and Address

Solar Energy Research Institute
1617 Cole Boulevard
Golden, Colorado 80401-3303

13. Type of Report & Period Covered
Technical Report

14.

15. Supplementary Notes
SERI Technical Monitor: Byron Stafford, (303) 231-7126

16. Abstract (Limit: 200 words)

This document describes efforts to improve the quality of candidate photovoltaic materials used in amorphous wide- and narrow-band-gap materials, namely, a-$Si_{1-x}C_x$ and a-$Si_{1-x}Ge_x$. Although these alloys show a decrease in mobility-lifetime product as the fraction of silicon decreases, their optical properties show marked differences. Microcrystalline p-layer films containing carbon were prepared to evaluate their importance for achieving high open-circuit voltages. Silicon-germanium cells were studied to optimize their performance in multijunction, stacked cell structures. The best cells fabricated from the silicon-germanium alloys yielded a conversion efficiency of 10.1% with a band gap of 1.55 eV. Several alloy-based stacked cells had conversion efficiencies of more than 10%: an a-SiC/a-SiGe cell yielded 10.5% and an a-SiC:H/a-Si:H structure yielded 10.2%. Stacked-junction cells showed far less susceptibility to light-induced degradation.

17. Document Analysis

a. Descriptors Photovoltaic cells ; amorphous state : silicon solar cells ; efficiency

b. Identifiers/Open-Ended Terms

c. UC Categories 271

18. Availability Statement

National Technical Information Service
U.S. Department of Commerce
5285 Port Royal Road
Springfield, Virginia 22161

19. No. of Pages
121

20. Price
A06

Form No. 0069 (3-25-82)